MECHANISM OF TIP VORTEX CAVITATION SUPPRESSION

BY POLYMER AND WATER INJECTION

by

Ryo Yakushiji

A dissertation submitted in partial fulfillment
of the requirements for the degree of
Doctor of Philosophy
(Naval Architecture and Marine Engineering)
in The University of Michigan
2009

Doctoral Committee:

Professor Steven L. Ceccio, Chair
Professor David R. Dowling
Professor Marc Perlin
Professor Armin W. Troesch

DEDICATION

To everybody whom I met in the United States

ACKNOWLEDGEMENTS

I would like to acknowledge that this research is supported by the Office of Naval Research and program manager Dr. Ki-Han Kim. In addition to that, my 3-year study in the University of Michigan was supported by Technical Research and Development Institute, Ministry of Defense, Japan.

CONTENTS

LIST OF FIGURES

LIST OF TABLES

ABSTRACT

Tip vortex cavitation (TVC) is the form of cavitation inception occurs when a bubble is trapped in to the low-pressure region located in the center of the vortex from the tip of a hydrofoil. TVC can be observed in marine propellers and, in the most cases, starts to appear at lower ship speed than other forms of cavitation. Since TVC suppression would reduce the acoustic noise emission from ship propellers, researchers have endeavored to suppress TVC through both passive and active means. Researchers have shown that TVC can be suppressed by polymer or water injection. However, the physics of this suppression is not understood, and this lack of knowledge makes it difficult to apply the active controlling technology for ship scale propellers. This work aims to reveal the flow phenomena that lead to tip vortex cavitation (TVC) suppression by polymer and water injection.

At the beginning of this study, the TVC suppression effect was surveyed experimentally using a wide range of injection flow rates and polymer concentrations as mass was injected into the tip region of an elliptic hydrofoil. Aqueous polymer solutions were injected, and TVC desinence was measured using a laser-scattering bubble detector. The series of TVC desinence tests revealed that TVC desinence was delayed with increasing injectant flow rate and polymer concentration, and that the suppression effect became saturated beyond a maximal flow rate and a polymer concentration. At the maximum extent of suppression, the cavitation inception number was reduced to σ=1.8, compared to a value of σ=3.5 for the non-injection case.

The freestream bubble nuclei dependence was also surveyed by coupling observations of TVC with measurements from a cavitation susceptibility meter. The TVC desinence was governed by nuclei density in the water tunnel, but the degree of cavitation suppression by polymer injection was found to be independent from background nuclei density. This observation suggests that mass injection leads to modification of the flow field near the tip region of the hydrofoil, and this modification is responsible for TVC suppression.

In the next step, the flow field near a hydrofoil tip was investigated using Stereo Particle Image Velocimetry (SPIV). From the averaged flow filed, a static pressure at the vortex core was estimated by integrating Euler's equation. The estimated average static pressure for non-injection condition and mass injection conditions did not reveal significant difference. Hence, changes in the average flow field did not account for TVC suppression. Furthermore, the estimated average static pressure derived from the SPIV measurements for the baseline (non-injection) flow (Cp=-2.3) was not low enough to cause a cavitation at the observed inception pressure (σ=3.5). An extensive literature review on the past studies of similar flows also found similar inconsistency between the estimated average static pressure in the vortex core and observed cavitation inception numbers.

In the end of the study, close observations using high-speed video imaging and flow visualization with fluorescence dye were carried out. The high-speed video images taken for the baseline (non-injection) cases suggested the existence of unsteady flow structures near the hydrofoil tip, which can lead local reduction in static pressure and accompanying TVC inception. Fluorescence dye visualization showed filamentation of the injected polymer near the tip region, and this suggests that a viscoelastic interaction between the polymer and the tip flow.

Flow unsteadiness in the tip region can be introduced by several possible mechanisms (e.g. vortex-vortex interaction or the entrainment of turbulent shear flow around a vortex core), and vortex fragmentation and merger can increase the likelihood of pressure fluctuations in the tip region. The addition of mass appears to disrupt these processes, which is enhanced by the presence of the polymer. Further study is needed to reveal precisely how the mass injection reduces unsteadiness in the tip region. Moreover, we still need to obtain the knowledge to scale up the suppression effect for the ship scale propellers. The present study recommends the experimental approach on a large-scale hydrofoil, since the flow unsteadiness can be strongly dependent on Reynolds number scaling.

Chapter One

Motivation of this research

1.1 Tip vortex cavitation

The tip vortex cavitation (TVC) is the form of cavitation and TVC inception occurs when a bubble is trapped in to the low-pressure region located in the center of the vortex from a hydrofoil tip (see Figure 1-1 & Figure 1-2). TVC can be observed in marine propellers (see Figure 1-3) (Kinnas 1998) and, in the most cases, starts to appear at lower ship speed than other cavitation. To improve ship's acoustic stealth, the physics of TVC has been studied with extensive efforts.

1.2 Mechanism of TVC

From a tip of a three-dimensional hydrofoil, a circulation is shed downstream. In the classical wing theory, a non-uniform circulation distribution along span-wise direction also makes vorticity shedding from the trailing edge. This span-wise vorticity sheet (=vortex lattice) is rolled-up around the primarily vortex from the tip at downstream.

TVC can take place, if a nucleus is trapped into the viscous core and experiences a pressure low enough to be activated.

1.3 Control of Tip Vortex Cavitation

There exist several countermeasures to control TVC on marine propellers.

The most practical way is to control a span-wise circulation distribution. A common way is decreasing the circulation at a tip region, which leads the lower circulation of TVC at fully rolled-up condition resulting in a higher static pressure at tip vortex from a blade (Carlton 1994). Although this design approach offsets the blade geometry from the optimized design for maximum efficiency, it is generally referred to as "tip un-loaded propeller" and is the most common way to suppress TVC.

The second idea is by putting obstacles at foil tip. As explained in a later part, a vortex core size governs the minimum static pressure in a vortex core. The additional obstacle is expected to increase the vortex core size and makes the vortex core pressure high. Another approach is to add extra roughness at a blade tip, which increases the boundary layer thickness on a blade. The vortex core size is related to the boundary layer thickness on a blade, so this approach also increases vortex core size.

The before mentioned methods are forms of passive control of TVC, and they are summarized by Platzer & Souders (1979), which carried out a thorough literature survey (see Figure 1-4 for a summary). Following that, the same research group, Souders & Platzer (1981), conducted intensive experiment works and showed that some of those ideas are effective for TVC suppression. But each method definitely introduces a larger drag for propeller rotation and that will reduce the overall efficiency of the propulsion system. Moreover, an additional obstacle at blade tip can trigger other structural or cavitation problems. Therefore these ideas for passive control TVC are rarely applied in actual marine propellers.

Disadvantages of above mentioned passive control methods are they result in lower efficiency during whole operation environments. If TVC is problematic only at a high ship speed range or only in limited conditions (e.g. during maneuver or acceleration), a transient active control on TVC will be beneficial. A form of active control of TVC is to implement a transient countermeasure by injecting polymer or water from propeller blade only when needed. Several experimental works were done on scale models and each result shows some extent of TVC suppression effect (Souder & Platzer (1981), Fruman et al. (1995), Chahine (1993)).

Those past works will be reviewed intensively in Chapter Two, however it should be noted that the physics on TVC suppression due to polymer injection has not yet

revealed. Then the absence of the definite explanation on TVC suppression mechanism makes it difficult to apply this active control method in actual ship scale propellers.

1.4 Motivation and strategy of this study

Therefore, this study aims to reveal the mechanism on TVC suppression due to polymer injection. The knowledge on the physics of this active TVC control will help to give a guidance to design an injection system and will assess the expected suppression effect in a ship scale propeller. Since the flow structure is dependent on the scale and since this type of technology is, in the most of cases, developed by model tests in water tunnels, the suppression effect in a ship scale test should be extrapolated from a model test, based on knowledge on suppression mechanism.

The environment around this work is preferable, because there are some up-to-date measurement technologies (e.g. stereo particle image velocimetry, high speed video camera), which was not available in 1980's (the most of experimental works on this topic were carried out in 70'-80's). Using those technologies will provide a larger amount of database in wide range of test cases and detailed observations on the phenomena.

The recent works on TVC inception mechanism itself have revealed the physics of TVC, which is more complex than the classical theory. Therefore, a research study on TVC control has to be done with reliable and repeatable measurements, in order to approach the detail of phenomena. This study established a definite definition of TVC inception/desinence and intends to evaluate a degree of suppression quantitatively and sensitivity on polymer concentration or other parameters. This strategy also requires a well-controlled environment, especially in terms of a bubble nuclei distribution in the water tunnel.

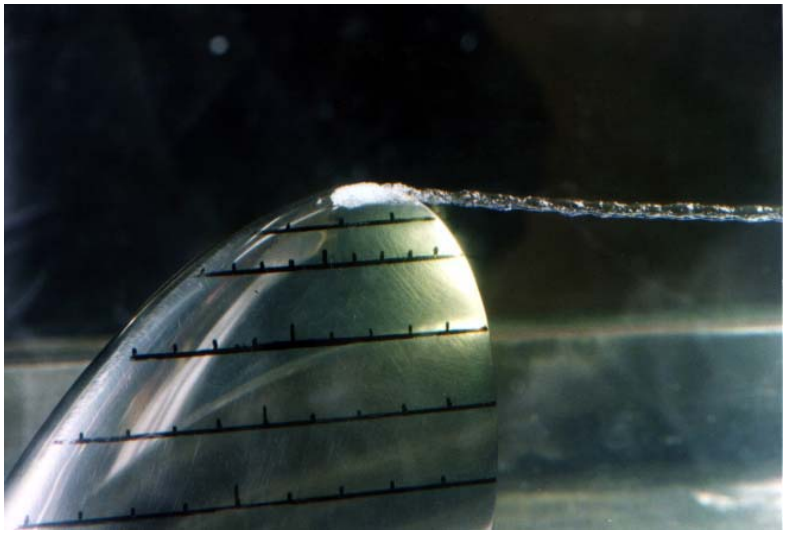

Figure 1-1: Typical tip vortex cavitation on a back skewed elliptic foil
(from http://www.fluidlab.naoe.t.u-tokyo.ac.jp/Research/CavPictures/large/Tip.sb.jpg)

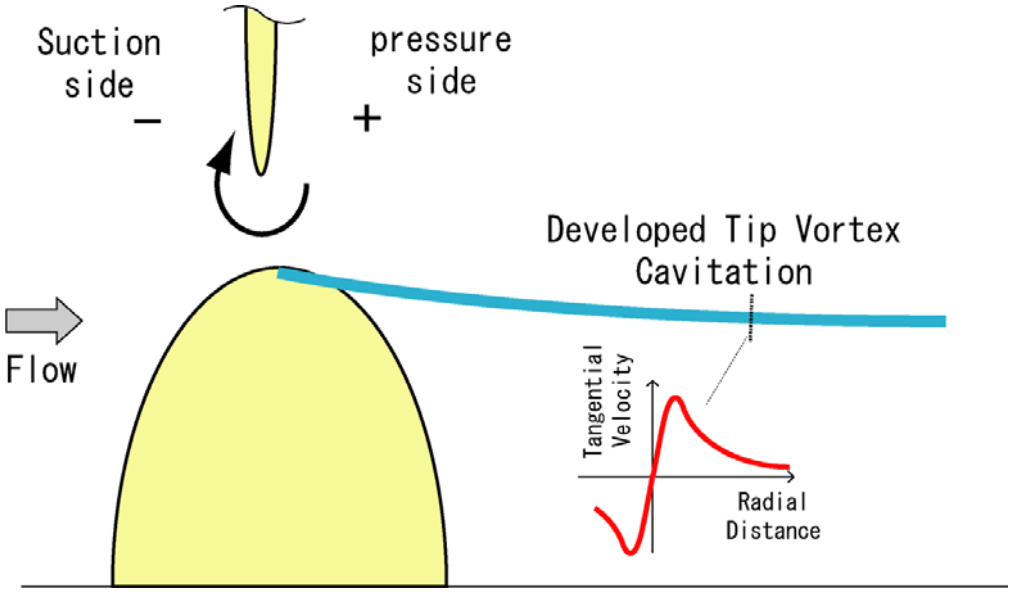

Figure 1-2: General description on flow structure around TVC

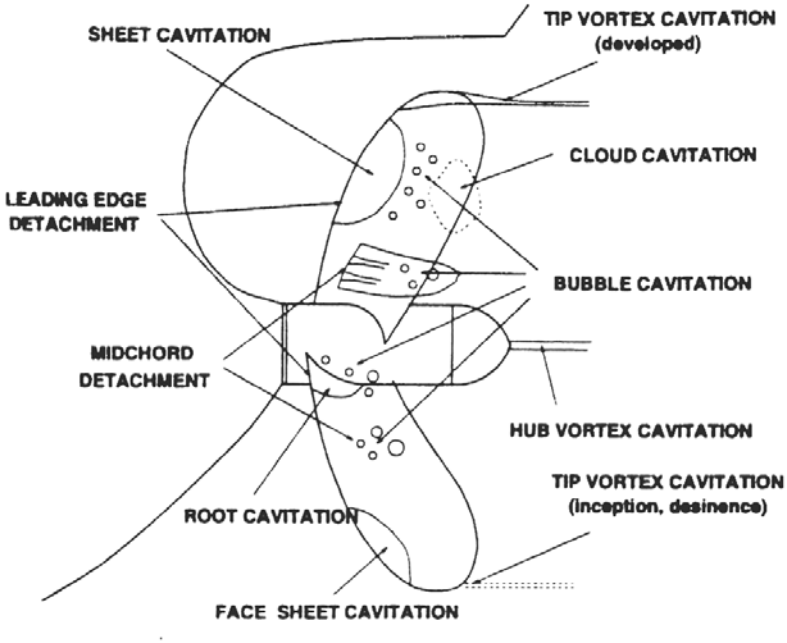

Figure 1-3: Cavitation categories on marine propeller (Kinnas 1994)

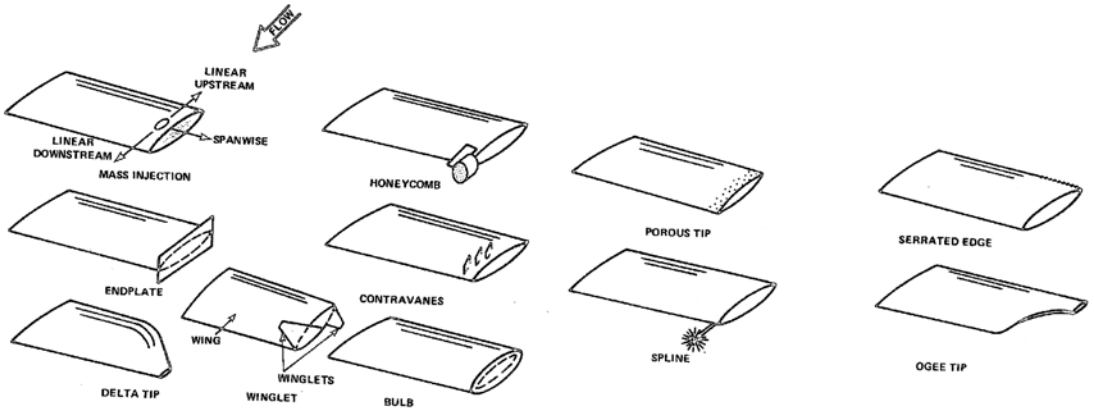

Figure 1-4: Passive TVC suppression ideas (Platzer & Souders 1979)

References

Carlton, J.S., 1994, *"Marine Propellers and Propulsion"*, Butterworth Heinemann, 1994, pp438-pp439

Chahine G. L., Frederick, G. F., Bateman, R. D., 1993, *"Propeller tip vortex cavitation suppression using selective polymer injection"*, Journal of fluids engineering, Vol. 115, pp497-503

Fruman, D.H., Pichon, T., T., Cerrutti, P., 1995, *"Effect of drag reducing polymer solution ejection on tip vortex cavitation"*, Journal of marine science and technology, Vol. 1, pp13-23

Kinnas, S. P., 1998, *"The prediction of unsteady sheet cavitation"*, 3rd international symposium on cavitation, Grenoble, France

Platzer, G. P., Souders, W. G., 1979, *"Tip vortex cavitation delay with application to marine lifting surfaces"*, DTNSRDC Technical report 79/051

Souder W.G., Platzer G. P., 1981, *"Tip vortex cavitation characteristics and delay of inception on a three-dimensional hydrofoil"*, DTNSRDC Technical Report 81/007

Chapter Two

Literature Review

2.1 Mechanism of Tip Vortex Cavitation (TVC)

The physics on TVC has been worked with intensive efforts, since controlling this type of cavitation is important for silent ship designs. Franc and Michel (2004) describes the mechanism of TVC inception in their textbook. As shown in a classical wing theory, the circulation distribution along spanwise direction makes a vorticity sheet form a hydrofoil trailing edge. This vorticity is eventually rolled –up around a primary tip vortex from a hydrofoil tip. In other words, the circulation around a primary tip vortex increases gradually in downstream.

Moreover, the line vortex from a hydrofoil has a viscous core at its center. Fundamentally, the thickness of this viscous core is governed by a boundary layer thickness on a foil tip.

Those two parameters, a circulation strength and a viscous core size, governs a minimum static pressure in a vortex core and a velocity measurement around TVC showed that the minimum pressure point along a flow direction is located at ~10% chord length down stream from a tip.

Besides the basic physics on TVC, a lot of efforts have been made on “nuclei effect” and “scale effect”, which is strongly controls TVC inception. Since the TVC inception point is estimated from a model test, the intensive efforts are made on how to

scale up the model scale result to the actual ship scale performance, especially in terms of Reynolds number scaling. In addition to that, small bubble nucleus in the water is known to affect TVC inception and the distribution of the nuclei in model test facility is different from the distribution in the sea. Therefore, this nuclei dependence has been also a big issue on TVC study. In the next part, some past works on scale effect and nuclei effect will be reviewed.

2.2 Reynolds number scaling

The most classical and practical knowledge on the scale effect of TVC inception was given by McCormick (1962). He derived a power law for the TVC inception point relating to the Reynolds number based on a foil chord length, since the viscous core size is related to the boundary layer size on the foil and the strength of the circulation around a vortex, which can be simply scaled by an attack angle. By combining the experimental data, McCormick derived the following regression equation.

$$\sigma_i = c\alpha^{1.4}\,\mathrm{Re}^{0.4} \qquad \text{(eq. 2-1)}$$

σ_i : *Incipient Cavitation Number*
C : *Empirical Coefficient*
α : *Attack Angle*
Re : *Reynolds Number based on root chord length*

This equation is still used in the actual propeller design and no practical estimation method has been established beyond this point.

Fruman et al. (1992) conducted a series of TVC inception test for different scale elliptic foils. Three different scale water tunnels are used and intensive flow field measurements by LDV revealed that not only a viscous core size but also an axial velocity in the core was changed among the different scale. This implies that the actual physics on TVC inception is more complicated than McCormick's scaling.

2.3 Nuclei Effect

Cavitation phenomenon is known to be strongly dependent on the density of small bubbles flowing in the water. The first work on this issue was done by testing an

axisymmetric body in different tunnel facilities (Lindgren and Johnsson (1964)). The bubble cavitation inception points on a tested body among different facilities are inconsistent and it is inferred that the difference of bubble nuclei in water tunnels was behind this inconsistency.

After several elementary works, ITTC (International Towing Tank Conference) carried out a project to approach nuclei dependence at a French large water tunnel GTH, in which nuclei distributions could be controlled at three different levels (Gindroz & Billet (1993)). In the program, three propeller models were manufactured, on which three different types of cavitation (i.e. sheet, bubble, and tip-vortex cavitation) appears. Then bubble cavitation and TVC shows a strong dependence on the water quality, meanwhile sheet cavitation is insensitive.

Based on this observation, Gindroz & Billet (1993) established a way to correlate nuclei effect combined with a nuclei measurement method, "Event Rate Analysis". They introduced a clear definition of cavitation inception point. (That is to say, one bubble is activated for one second.) Then the inception cavitation number is correlated to the inception point in "zero-tension water", based on the nuclei measurement result and the probability of bubble capture in a vortex core. Gindroz et al. (1997) applied this method to the cavitation inception test of a destroyer's propeller and they reported that it matches well with the two different nuclei distributions.

To approach cavitation inception problem, it is strongly required to carry out a bubble nuclei measurement and take account of its effect. In this study, nuclei density in a test facility was measured and the effect of both a background nuclei distribution and nuclei content in injection fluid will be evaluated.

There are a lot of methods to measure nuclei distributions and those technologies will be reviewed at the beginning of Chapter Three.

2.4 Active Control on TVC

As briefly introduced in Chapter One, an active control on TVC by injecting polymer solution or water has been worked on by several researchers.

Souder and Platzer (1981) injected water into the core of the vortex, which is shed form an elliptic foil. In their experiment, water was injected from the hole that was drilled

through a foil from the root on the tip (injection outlet) at several volumetric flow rates. It was found that water injection delays TVC inception (see Figure 2-1). The active injection was tested coupled with surface roughness and gave the maximum reduction effect. It should be noted that the suppression effect seems to be saturated beyond a certain flow rate.

Fruman et al. (1995) tested polymer injection on a similar elliptic hydrofoil. The aqueous solution of Polyox WSR301, which is typically used for a skin frictional drag reduction, was injected from a hole on an elliptic foil. They reported that TVC inception point was delayed by polymer injection, but water injection did not show TVC suppression effect.

They also conducted velocity measurements around a vortex core region and reported that the vortex core size was increased, when there was polymer injection. The observed change in vortex core size was sufficient to account for the corresponding static pressure difference between with/ without injection case required to suppress cavitation (see Figure 2-2).

Chahine et al. (1993) tested a model propeller with polymer injection. Intensive observations were done to find the most effective location for polymer injection hole. A wide range of polymer concentrations and wide range of injection rates were examined too. In addition to an aqueous polymer solution, glycerin and water injection were tested but did not show a significant effect on TVC suppression (see Figure 2-3). Chahine's work progresses to infer a TVC suppression mechanism by polymer injection. In their explanation, the injected polymer jet swells just after the injection hole (generally known as "dye swell", and caused by the polymer's elasticity), and this lead to a radial velocity. The material strain caused by this radial velocity introduces additional stress and static pressure increment.

In summary, based on past works, we can point out the present situation of TVC active control technologies.

- To some extent, TVC is suppressed by polymer injection
- No quantitative scaling on polymer injection effect has been established
- There is a disagreement on the effect of water injection.

- The underlying physical mechanism of TVC suppression by water/polymer injection and its scalability is still unknown.

Before implementing TVC suppression by polymer injection in actual application, it is necessary to understand the physics behind this phenomenon. Even though there is experimental data on model propeller (i.e. Chahine's result), it is not sufficient to properly scale up the effect for a ship size propeller.

2.5 Active control on other kind of cavitation than TVC by polymer injection

There were few past works on jet cavitation suppression by adding a polymer. Hoyt (1973) surveyed how polymer solution can suppress the cavitation, which forms in the jet from a nozzle. The study obtained the relationship between the cavitation inception point and polymer concentration. In the end of the study, the following two possible mechanisms were pointed out; 1) some chemical reaction removes bubble cavitation nuclei in the jet, 2) polymer reduced a intensity of the turbulent in a shear flow around a jet.

For sheet cavitation, Ellis et al. (1970) carried out an experimental study on a sheet cavitation on a hemispherical body. Fundamentally, sheet cavitation is formed from a separation bubble. Therefore, it would be natural that non-Newtonian fluid changes the behavior of separation bubble.

2.6 Recent works on TVC

The previously mentioned works assumed the classical model in which, one bubble nucleus is trapped into a single line vortex core from a foil tip and generate one acoustic pulse signal. However, recent works revealed more complicated physics on TVC inception mechanism.

2.6.1 TVC scaling

Choi (2006) revealed that a single bubble can generate multiple acoustic pulses during its inception, growth and collapse, from a close observation on a single line vortex

cavitation. This new knowledge shows that the assumption used in the "event rate analysis" is not necessarily precise for TVC scaling.

From the viscous scale effect viewpoint, Shen et al. (2001) 's numerical work shows that the slip velocity of different size nuclei causes the bias of bubble nuclei entrapment. Therefore using a single sectional area for "event rate analysis" is not appropriate and it should be noted that this bias is dependent on the scale of hydrofoil.

2.6.2 Flow unsteadiness and TVC inception mechanism

Moreover, new perspective on the mechanism of vortex cavitation inception on marine propeller was drawn by the series of experimental works on a ducted propeller. Oweis et al. (2006) observed the vortex cavitation on a ducted thruster and reported that the secondary vortex from trailing edge is stretched by primary vortex's induction and resulted in earlier inception than the primary TVC.

Arndt (1991) did an intensive observation and flow visualization of TVC and the experimental work reported that the existence of vortex interaction at the elliptic foil tip could be related to TVC inception mechanism. In addition to the primary vortex from a blade tip, he inferred an existence of the secondary vortex from a separation bubble on a leading edge near the tip region from the oil pattern visualization. Then he pointed out the possibility of this secondary vortex has an important role of TVC inception, which was observed near tip region.

Even though, there is no direct measurement results on the vortex interaction near the hydrofoil tip, it should be pointed out that the vortex interaction can probably controls TVC inception for "open type" propellers. Those past works shows that the steady flow model in a classical theory of TVC should be re-constructed with taking account of the unsteadiness of the flow field.

2.6.3 Research works on co-rotating vortex-vortex interaction

As shown in the previous chapter, the co-rotating vortex-vortex interaction may contribute TVC inception near the hydrofoil tip. Therefore it will be beneficial to review several research works on co-rotating vortex-vortex interactions.

The intensive experimental measurement on co-rotating vortex merging process was carried out by Davenport et al. (1999). Their flow measurement revealed that the unmerged cores of co-rotating vortex pair appear to be turbulent, unlike a single vortex. In other words, the vortex interaction can make a lower pressure field than a single vortex.

Oweis & Ceccio (2005) carried out an experimental study on the vortex cavitation inception for a ducted propeller and they give a good summary of the vortex interaction. When two unequal strength co-rotating vortices merge into a single structure, the weaker vortex becomes into filaments under the effect of the stronger vortex. This complex vortex-vortex interaction induces unsteadiness during the merging process. The same vortex-vortex interaction can occur in the open type propeller, because the leading edge separation can make a vorticity as Arndt's work.

Chang et al (2007) tried to visualize the co-rotating vortex merging process in a water tunnel. They generated a vortex pair in a water tunnel and captured a still picture on the vortex merging process. In the picture, we can see the filament of vortex cavitation between a main tip vortex cavitation pair.

Hsiao et al. (2003)'s numerical study succeeded to simulate a vortex merging and its pressure drop by DNS. The work intended to simulate a vortex merging process, in which a weaker vortex is stretched and become filaments, then is trapped into a primary vortex. In the numerical calculation, two Lamb-Oseen type vortices with different circulations are given at upstream and whole merging process was simulated. The minimum pressure field was captured just before the merging. This DNS result may consistent to the statistical data on turbulence flow in Davenport's study. With this single-phase DNS simulation, Hsiao continued to simulate a bubble motion and its growth by Lagrange motion equation. They found that a bubble nucleus with a radius of 50μm was captured in to the vortex core and was activated by a low-pressure area due to a vortex interaction. Going back to the basics of cavitation, bubble has to experience a low pressure during enough long time. In this sense, this simulation showed that vortex interaction could generate not only a low pressure, but also a long duration time, which can activate a bubble nucleus.

2.7 Concluding remarks of this chapter

As explained up to this point, recent efforts revealed that TVC inception mechanism is more complicated than the classical model. Therefore, this study takes the strategy of not simply basing on the classical model and potentially approach to the new mechanism. To this end, close observation and measurement on TVC inception by using up-to-date measurement technologies were carried out. In addition, the nuclei distribution was well characterized and repeatability of "water quality" during the experiments was ensured.

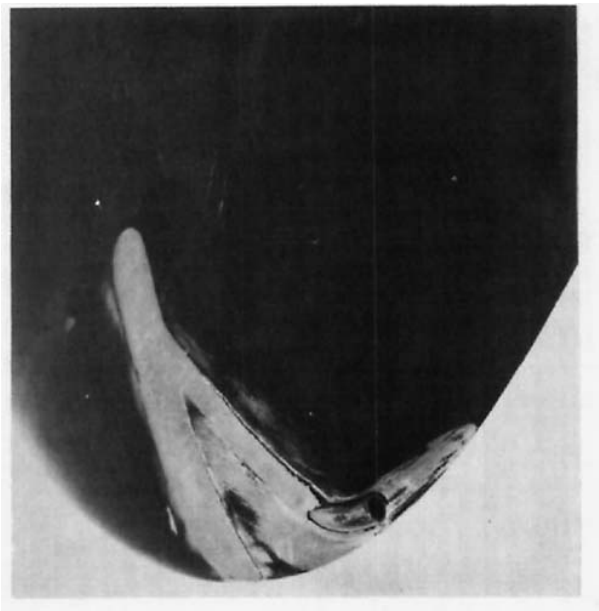

(a) Close up picture of an injection hole

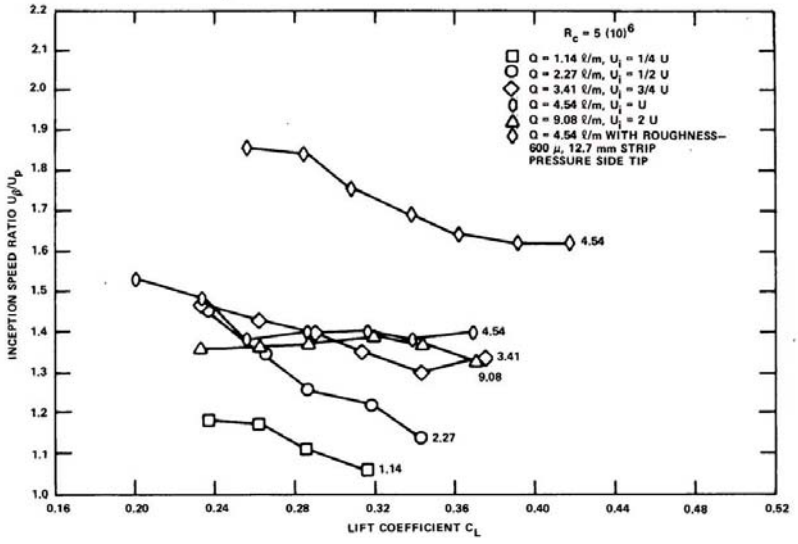

(b) TVC suppression effect

Figure 2-1: Active water injection test results (Souders & Platzer (1981))

In (b), U_β denotes inception speed with Active Mass Injection and U_p denotes inception speed w/o mass injection and U_j is the ratio between the injected mass velocity and the uniform velocity in the water tunnel

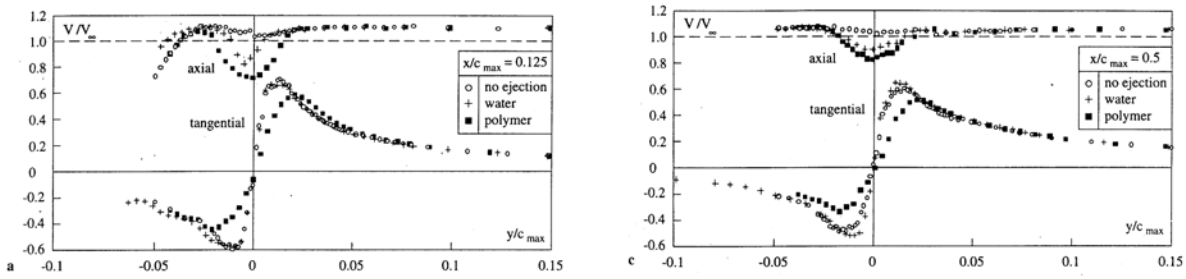

(a) Axial and tangential velocity around tip vortex

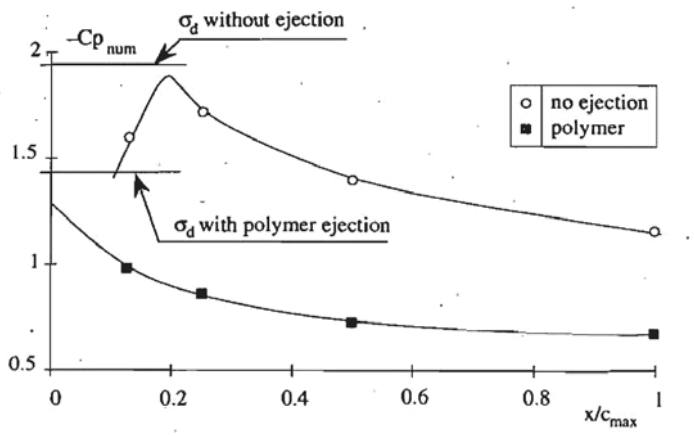

(b) Cavitation inception point and estimated static pressure

Figure 2-2: TVC suppression effect and flow field measurement
(Fruman et al. (1995))

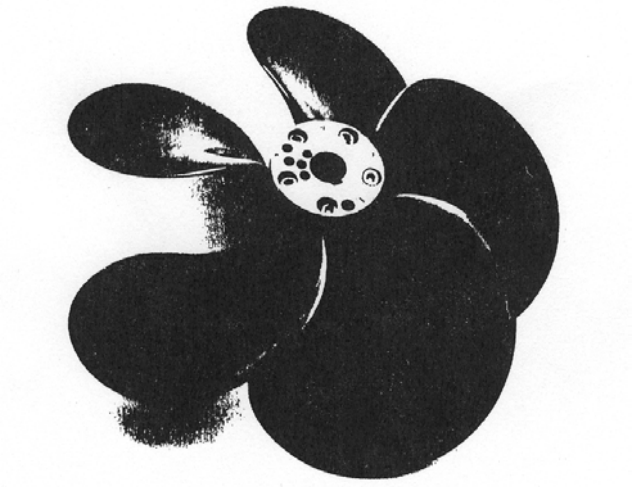

(a) Model propeller for injection test

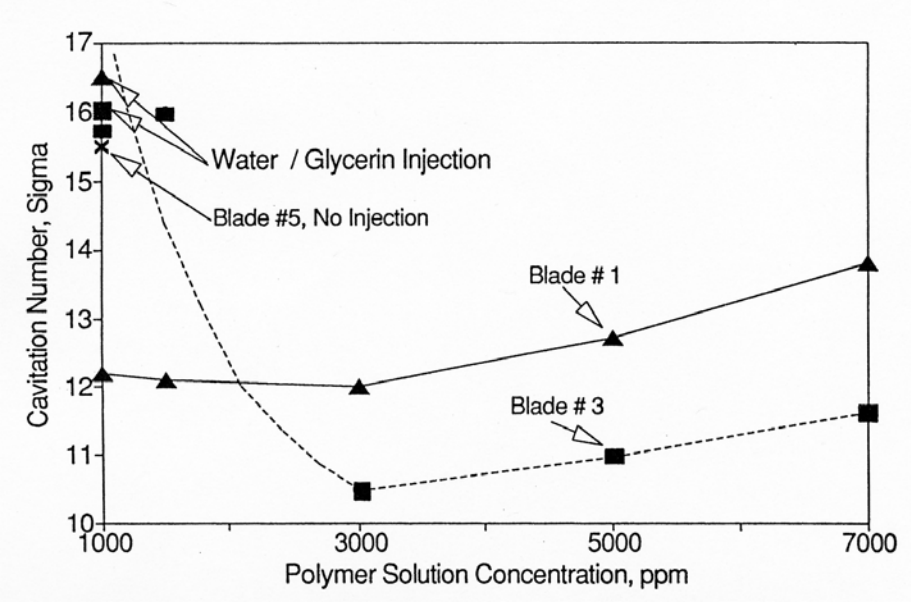

(b) TVC suppression effect due to polymer and other liquids injection

Figure 2-3: Model propeller experiment (Chahine et al. (1993))

References

Arndt, R.E.A., Arakeri, V.H., Higuchi, H, 1991, *"Some observations of tip-vortex cavitation"*, Journal of Fluid Mechanics, Vol. 229, pp. 269-289

Chahine G. L., Frederick, G. F., Bateman, R. D., 1993, *"Propeller tip vortex cavitation suppression using selective polymer injection"*, Journal of fluids engineering, Vol. 115, pp497-503

Chang, N.A., Yakushiji, R., Dowling, D.R., and Ceccio, S.L., *"Cavitation visualization of vorticity bridging during the merger of co-rotating line vortices"*, Physics of Fluids, (2007)

Choi, J., 2006, *"Dynamics and noise emission of vortex cavitation bubbles"*, PhD thesis of the University of Michigan, Ann Arbor

Davenport, W.J., Vogel, C. M., Zsoldos, J. S., 1999, *"Flow Structure produced by the interaction and merger of a pair of co-rotating wing-tip vortices"*, Journal of Fluid Mechanics, Vol. 394, pp.357-377

Ellis, A.T., Waught, J.G., Ting, R. Y., 1970, *"Cavitation Suppression and Stress Effects in High-Speed Flows of Water With Dilute Macromolecule Additives"*, Journal of Basic Engineering, pp.459-466

Franc, J. P., Michel, J.M., 2004, *"Fundamentals of Cavitation"*, Kluwer Academic Publishers

Fruman, D. H., Dugue, C., Pauchet, A., Cerrutti, P., Brianson-Majollet, L., 1992, *"Tip vortex roll-up and cavitation"*, 19th International symposium on naval hydrodynamics, Seoul, Korea

Fruman, D.H., Pichon, T., T., Cerrutti, P., 1995, *"Effect of drag reducing polymer solution ejection on tip vortex cavitation"*, Journal of marine science and technology, Vol. 1, pp13-23

Gindroz, B., Billet, M. L., 1993*, "Influence of the nuclei on the cavitation inception for different types of cavitation on ship propellers"*, ASME FED-Vol. 177, Cavitation inception, Louisiana, USA

Gindroz, B., Balio, G., F, Matera, F., Elefante, M., 1997, *"Influence of the Cavitation Nucle on the Cavitation Bucket when Predicting the Full-Scale Behavior of a Marine Propeller"*, 21st Symposium on Naval Hydrodynamics, pp839-pp850

Hsiao, C.T., Chahine, G.L., 2003, *" Effect of Vortex/Vortex Interaction on Bubble Dynamics and Cavitation Noise"*, Fifth International symposium on Cavitation CAV2003, Osaka, Japan, pp1-8

Hoyt, J.W., 1973, *"Jet Cavitation in Polymer Solutions, "Cavitation and Polyphase Flow Forum"*, ASME

Lindgren, H., Johnsson, C.A., 1964, *"Cavitaion Inception HEAD FORMS I.T.T.C. Comparative Experiments"*, 11th International Towing Tank Conference, Tokyo, Japan, pp219-pp232

McCormick, B. W., 1962, *"On cavitation produced by a vortex trailing from a lifting surface"*, Journal of basic engineering, Vol. 83, pp369-379

Oweis, G.F, Ceccio, S.L., 2005, *"Instantaneous and time-averaged flow fields of multiple vortices in the tip region of a ducted propeller"*, Experiments in Fluids, Vol. 38, pp615-pp636,

Oweis, G.F., D. Fry, Chesnakas C.J., Jessup, S. D., Ceccio, S.L., 2006, *"Development of a Tip-Leakage Flow- part1: The Flow Over a Range of Reynolds Numbers"*, Journal of Fluids Engineering, Vol. 128, pp751-pp755,

Shen, Y.T., Chahine, G., Hsiao, C.T., Jessup, S., 2001, *"Effects of Model Size and Free-Stream Nuclei on Tip Vortex Cavitation Scaling"*, 4th International Symposium on Cavitation CAV2001, Pasadena, USA

Souder W.G., Platzer G. P., 1981, *"Tip vortex cavitation characteristics and delay of inception on a three-dimensional hydrofoil"*, DTNSRDC Technical Report 81/007

Chapter Three

Nuclei Measurement

As explained in the previous chapter, the nuclei distribution in the water tunnel has a strong effect on TVC inception. The first step to take account for this effect is to establish a way to measure the nuclei distribution in the water tunnel. There are many ways to measure the nuclei and those methods are reviewed briefly. This study chose a cavitation susceptibility meter to (CSM) measure the nuclei density in the water tunnel and its measurement bias and error is evaluated for the specific set up in this study.

3.1 Nuclei Measurement Method

3.1.1 Optical Method

Optical methods can be categorized into two groups. One is taking optical images and counting the radius of each bubble. The most conventional method is holography, in which two pictures are taken at different angles and three-dimensional images are reconstructed. This method was also used to measure a bubble distribution in the bubble cluster of a cloud cavitation (Kato et al. (1999)). The IR (Infrared)-Laser was also applied for the light source of image acquisition for the nuclei measurement in a water tunnel (Nagaya et al. (2005)), but each observation needs a large number of images to acquire a distribution plot. Moreover, it is hard to distinguish images of bubbles from images of solid particles.

Mie-scattering is applicable for nuclei measurement. The test water is introduced in a box surrounded by a photo-detectors and the radius of the bubble is estimated from the scattering angle. Phase Doppler Particle Anemometry (PDPA) is also using optical scattering, but it is basically using Doppler shift. Friesch (2000) applied PDPA to the nuclei measurement in three different size water tunnels. This method also has the problem of not being able to distinguish solid particles from bubbles, thus introducing error in the result.

3.1.2 Acoustic Method

Acoustic measurement uses acoustic absorption by bubble resonance. If a bubble is located in water with an acoustic wave of pulsation, the bubble oscillates in the response to the acoustic excitation and re-radiate energy into the liquid. In other words, bubble acts as an oscillator with a natural frequency. The system is composed of a couple of acoustic emitter and receiver. Since the attenuation and the phase lag between the acoustic transducers are the function of the bubble radius (i.e. corresponding natural frequency) and bubble density, we can estimate a bubble nuclei radius and each density by solving an inverse problem.

Chahine et al. (2001) developed a commercial model of this system and carried out a calibration with an optical counting. It showed a good agreement. However, the acoustic field between acoustic transmitters might affect the result. In addition to that, imaginary “zero nuclei” water has to be prepared to take a background. Therefore this method is not straightforward method for the low nuclei density in the water tunnel, although this might be very useful for a high bubble density flow.

3.1.3 Cavitation Susceptibility Meter

In this effort, Cavitation susceptibility meter (CSM) was used to measure a bubble nuclei distribution. The method is using bubble dynamics to detect a bubble nucleus. From Rayleigh-Plesset equation, we can obtain the stability condition for the bubble radius and static pressure (Franc and Michel (2004)).

$$R_{crit} = \frac{4}{3} \cdot \frac{S}{P_v - P_{crit}} \qquad \text{(eq. 3-1)}$$

R_{crit} : critical radius of a bubble
S : surface tension
P_v : vapor pressure
P_{crit} : critical pressure for given radius

In other words, for a given bubble radius, there exists a critical pressure for its stability. If the ambient pressure around the bubble is larger than the critical pressure, the bubble size changes quasi-statically with following an equilibrium condition. But, once the static pressure suddenly becomes lower than the critical pressure, the bubble radius increases explosively, i.e. cavitation inception takes place.

CSM is using the critical pressure to estimate the bubble radius. The system is composed of a contraction flow section to measure the volume flux in the system and a venturi section to make a low static pressure part to activate a bubble nucleus in to a bubble cavitation (see Figure 3-1).

Bubble nucleus flowing in the pipe pass through a low static pressure in this venturi section and, if the static pressure is lower than the critical pressure, bubbles cavitate and generate acoustic signals. The pressure signal is detected by a piezo-electric transducer located at the slightly downstream from the venturi throat. Since the system has a variable speed pump on its downstream, the static pressure at venturi can be controlled. The number of acoustic signals from venturi is thought to correspond to the number of bubble nucleus, whose radius is larger than the critical radius related to the static pressure at a venturi throat.

The original idea is implemented by Oldenziel (1982) and some modification is done by Pham et al. (1995). The measurement system used in this work has a center-body at the venturi part. Gowing (1999) carried out a comparative test between results from an old type venturi without a center-body and a new version with center-body.

3.1.4 Reason why CSM was used in this study

As summarized above, there are many ways to measure cavitation nuclei in a water tunnel and each method has both advantages and disadvantages. 19th ITTC

(International Towing Tank Conference) did a comparative test between three different measurement technologies (Gindroz and Marjollet (1992)) and a significant difference on the results from those methods was found, due to the physics of the measurement itself. 23rd International Towing Tank Conference (ITTC) (2002) carried out a survey on the nuclei measurement method for water tunnel facilities and concluded that there is no "standard method".

However, to the author's knowledge, only the CSM has been used for cavitation inception problems, in which the cavitation inception physics was discussed with the nuclei distribution, while other methods were used for just confirming the repeatability of the test or general tendency at different tunnel size. Therefore, CSM was chosen as the instrument to measure the nuclei distribution though recognizing the necessity of carrying out a thorough evaluation of its measurement bias and error.

3.2 Cavitation Susceptibility Meter Set up

The water inside the water tunnel is taken at an upstream corner into 25.4mm (1 inch) diameter vinyl tube to CSM venturi part. CSM is set on the ground floor and the venturi section center is 2.6m lower than the test section center. The variable speed pump is connected to the downstream of CSM venturi section and water is returned back at lower duct. The actual dimension and its arrangement are shown in Figure 3-2. The detail of the water tunnel is explained in the next chapter.

3.3 Measurement bias and uncertainty

Although CSM has been used for previous studies, the measurement biases and uncertainty for this specific set up is evaluated with up to date technologies. The bias due to bubble slip velocity and the bias due to static pressure difference are evaluated numerically. Then the biggest factor, the bias due to the limited dead time of CSM event counting algorithm, is evaluated by the comparison with a high-speed video imaging.

3.3.1 Bias due to bubble slip velocity difference inlet

Oldenziel (1982), who originally invented this venturi type nuclei measurement technology, introduced a numerical model on the measurement bias due to the bubble

motion at the inlet for sampling line. The flow velocity in the sampling line has to be different from the velocity at the water tunnel. Consequently, this makes the pressure difference and the radial motion of the bubble. Since the radial excursion due to this pressure gradient is dependent on the bubble size, we need to evaluate the resulting measurement bias.

Figure 3-3 shows the effect general geometry of the inlet. The measurement bias on the nuclei number with a certain bubble radius can be related to the radial excursion length.

$$\frac{\partial n_s}{n_s} = 1 - \frac{(d_s - l_s)^2}{d_s^{\,2}} \qquad \text{(eq. 3-2)}$$

n_s : number of nuclei

d_s : inlet diameter

l_s : excursion length

Oldenziel derived an approximation for the radial excursion from the motion equation of the bubble as follows,

$$l_s = \frac{\beta R^2}{\nu}(u_0 - u_s) \qquad \text{(eq. 3-3)}$$

u_0 : velocity in the water tunnel

u_s : velocity in inlet tube

R : bubble radius

β : constant =0.3

This bias was evaluated along the experiment condition range. The flow rate of the venturi (this controls the inlet velocity) Q_{vent} was ranged from 0.7 l/s to 1.3 l/s and the bubble radius was changed from 0.1 micron to 100 micron. Figure 3-4 shows the

calculated bias and it is less than 10% for the bubbles with a radius smaller than 100micron.

3.3.2 Bias due to static pressure difference

As shown in Figure 3-2, the CSM venturi part was located lower than the test section height, the bubble behavior in a different water head was calculated numerically and corresponding negative tension difference was also evaluated.

As the first step, the static pressure inside of the water tunnel loop and a branched line to CSM was estimated by simply assuming the volumetric conservation. Then the unsteady bubble behavior given by Rayleigh-Plesset equation eq. 3-4 is solved by numerically.

$$R\frac{dR^2}{dt}+\frac{3}{2}\left(\frac{dR}{dt}\right)^2=\left\{\left(P_{\infty 0}-P_v+\frac{2S}{R_0}\right)\left(\frac{R_0}{R}\right)^{3\gamma}-P(t)+P_v-\frac{4\mu}{R}\left(\frac{dR}{dt}\right)-\frac{2S}{R}\right\} \quad \text{(eq. 3-4)}$$

$P_{\infty 0}$: *initial ambient pressure*
γ : *Ratio of the specific heat of the gas*
μ : *viscosity*

The time-domain bubble radius history is plotted in Figure 3-6. The steady solution given by the equilibrium condition is also plotted in the same figure and it can be concluded that the equilibrium solution can capture the bubble behavior.

For each measurement results, the bubble size corresponding to the negative tension is entered into the numerical calculation of the equilibrium condition and the resulting bubble radius was inverted into a negative tension again. Figure 3-7 shows the negative tension shift due to the static pressure difference. The static pressure shift was at most 5% to the negative pressure value.

3.3.3 Bias due to dead time of CSM event counting algorithm

The whole CSM system is consists of a venturi measurement section and an analog circuit, which processes output signals from a piezo-electric sensor. The circuit, after applying high-pass/low-pass filters, processed an acoustic signal from bubble

collapse into a TTL pulses by voltage comparator. Since this pulse signal has a finite width, the circuit could under-count the multiple acoustic signals happening within a TTL pulse width as one event. In other words, the circuit can generate lower number of events, if the bubble density is too high.

This problem is widely known as "measurement bias due to a dead time" and a mathematical model has been already established. Under the condition that the bubble cavitation event happens randomly and the dead time is extended by an event happening within a pulse width, the "extended dead time model" can be applied. The measurement bias can be given by the following equation (Ida (2007)).

$$n = r \cdot \exp(-r\tau) \qquad \text{(eq. 3-5)}$$

n : counted event number

r : actual event number

τ : dead time

Figure 3-8 shows the calculated result with τ =0.67msec, which is implemented on CSM circuit. The under-counting bias is less than 10% for the nuclei density of n < 0.1 (nuclei/cm^3).

On the other hand, CSM event counting algorithm can over-count an acoustic signal from one bubble as multiple events, if the acoustic signal continues longer than a given pulse width. Ideally, a bubble cavitation is thought to generate a large pulse acoustic signal of short duration and that the venturi has little reverberation. However, high-speed video camera observations in this study show that bubble cavitations in a large negative tension (in a low static pressure at the Venturi throat) generate long acoustic signals, which exceeds a pulse width as defined by the event counting circuit. By using high-speed video, another bias was found at low negative tensions in the venturi throat. The system may not be able to detect a low level acoustic signal that the bubbles generate in this condition.

Since under/over-counting bias factors depend on the different parameters (i.e. the negative tension at a venturi throat and bubble density), those biases have to be evaluated

in a whole measurement environment regime. The comparison with CSM event counting algorithm results and high-speed video imaging was carried out in this study.

Figure 3-9 shows the bubble counting signal taken from the CSM circuit and the sequence of high speed video images synchronized to the signal at P_{crit}-P_v= 80kPa (P_{crit} is the static pressure at the venturi throat). The activated bubble grows and collapses in a short time as a typical bubble cavitation, which can be seen on an axi-symmetric body. However, in other case (see Figure 3-10), an activated bubble grows and became a small sheet cavitation, then collapses into bubble clusters. This bubble cluster makes multiple acoustic emissions and generates long signals from one activated nuclei. This long signal is counted as a multiple nuclei.

Then, as the next step, the comparison of nuclei number counted by CSM analog circuit and the nuclei number actually observed by a high-speed camera was carried out. To observe passing bubbles activated on an axi-symmetric center body from the whole viewing angle, a mirror was put on the backside of the CSM venturi. At a certain condition of the water tunnel, ~20 bubbles were counted on the high-speed video. Then synchronously the event-counting signal from CSM analog circuit was also acquired. The result is shown on the nuclei density plot (see Figure 3-11). The number written on the plot is the "over/under counting rate", which can be given in the following equation.

$$Over/UnderCountingRate \equiv \frac{Number\ of\ Counted\ Event\ by\ High\ Speed\ Video}{Number\ of\ Counted\ Event\ by\ CSM} \qquad \text{(eq. 3-6)}$$

As expected from the initial observation, the CSM tends to over-count nuclei at larger negative tension. Conversely, bubbles tend to be under-counted at lower negative tension, probably due to a low signal to noise ratio. It can be seen that under-counting is strongly dependent on negative tension value. But the over-counting tendency is dependent on a negative tension but also another factor, the static pressure in the test section. It can be inferred that the flow velocity in the venturi also controls the bubble behavior and its lifetime. Figure 3-12 is the plot between an over/under counting rate and cavitation

number at the venturi throat at different water tunnel conditions. The cavitation number at the venturi throat is given by the following equation.

$$\sigma_{vent} = (P_{up} - P_v) / \frac{1}{2}\rho\left(\frac{Q_{vent}}{S_{vent}}\right)^2 \quad \text{(eq. 3-7)}$$

P_{up} : Static pressure at upstream of venturi throat

Q_{vent} : Flow rate at venturi throat

S_{vent} : Sectional area at venturi throat

As shown in the plot, the over/under counting rate is primarily dependent on the cavitation number at the venturi throat, σ_{vent}. Pham et al. (1995) did a similar cavitation observation, when they developed a new CSM with a large center-body surrounded by a straight pipe, and concluded that bubble cavitation behaves like a sheet cavitation in the venturi section static pressure with $\sigma_{vent} < 0.7$.

3.3.4 Measurement Uncertainty

A measurement uncertainty is strongly dependent on the measurement time length or counted event numbers. In this study, CSM measurements were carried out by keeping the following rules;

- Measurement was done from smaller negative tension to larger negative tension (from high flow velocity to low flow velocity).
- Measurement was started from a certain negative tension, in which a few bubbles were counted in 60 seconds.
- Event rate was counted for 60 seconds, until the total event rate exceeds 100. Then the measurement time was shortened to 30 seconds.
- Event rate was counted for 30 seconds, until the total event rate exceeds 100. Then the measurement time was shortened to 10 seconds.

- Event rate was counted for 10 seconds until the resulted nuclei density exceeds 0.1 (nuclei/cm3).
- Each measurement was repeated three times at the same negative tension.

Ideally, the measurement has to be taken for a long enough time to generate a small uncertainty. However, the measurement was required to be done in an hour in this study, because the water in the pressure control tank would empty out after four or five hours and all CSM measurements were done just before or just after other experiments (i.e. the TVC inception test) to maintain the consistency.

Even though, three times measurement was not enough to evaluate the measurement uncertainty, the uncertainty with one standard deviation is plotted on Figure 3-13. The error bar is collapsed within a marker size at most data points, but the lowest nuclei density point at ~0.0001 has a large uncertainty.

3.4 Summary of Measurement Bias and Error

The sources of measurement biases and errors are summarized in Table 3-1. The maximum contributing factor is the over/under-counting bias due to a dead time. It should be noted that the measurement bias and error of CSM is still acceptable, in terms of accuracy of the nuclei measurement, even though the value of bias and error seems to be very large.

First of all, the difficulty of nuclei measurement itself has to be pointed out. As reviewed in 3.1.4, the measurement value itself is strongly dependent on the choice of the device. The comparison test among different measurement technologies generated the difference by the order of tenth (see 23rd ITTC (2002)). Therefore, the policy of the nuclei measurement is not to decide the absolute "true" value of nuclei density, but to keep a consistency or repeatability through the cavitation test.

In addition to that, the drastic nuclei density control can accept the measurement error and bias. By changing the dissolved oxygen content rate, it is possible to control the nuclei density by the order of tenth in the density. Figure 5-23 shows the actual measurement result in the university of Michigan's 9-inch water tunnel at two different

oxygen content rates and the density between two oxygen content rate (DO=19% & 50%) gives a significant difference in a nuclei density.

Finally, it can be noted that largest factor is not significant in the range of nuclei radius, which will generate cavitation. The cavitation is thought to be triggered by a bubble nucleus with the radius of 10 (μm). This critical radius corresponds to the critical pressure at the order of 10^4. Figure 3-11 shows that CSM' gives the smallest bias in this range. In other words, CSM system is "well-designed" to capture the bubble radius in this range.

From those points discussed above, CSM expected to give enough information on the bubble nuclei in the water tunnel experiment.

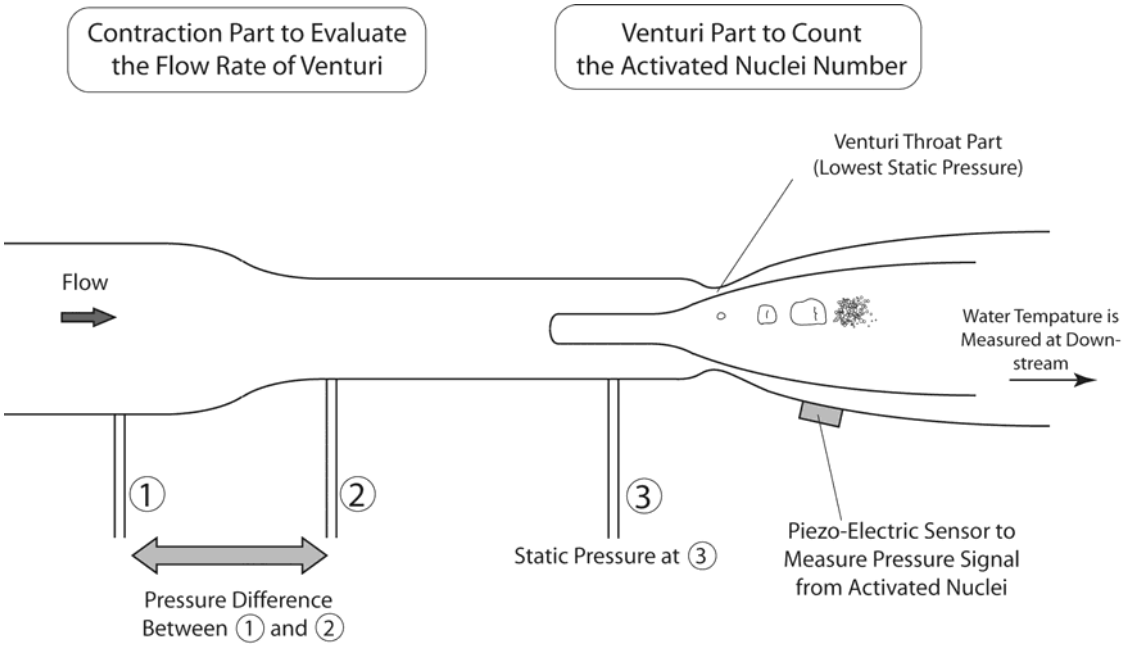

Figure 3-1: Mechanism of cavitation susceptibility meter

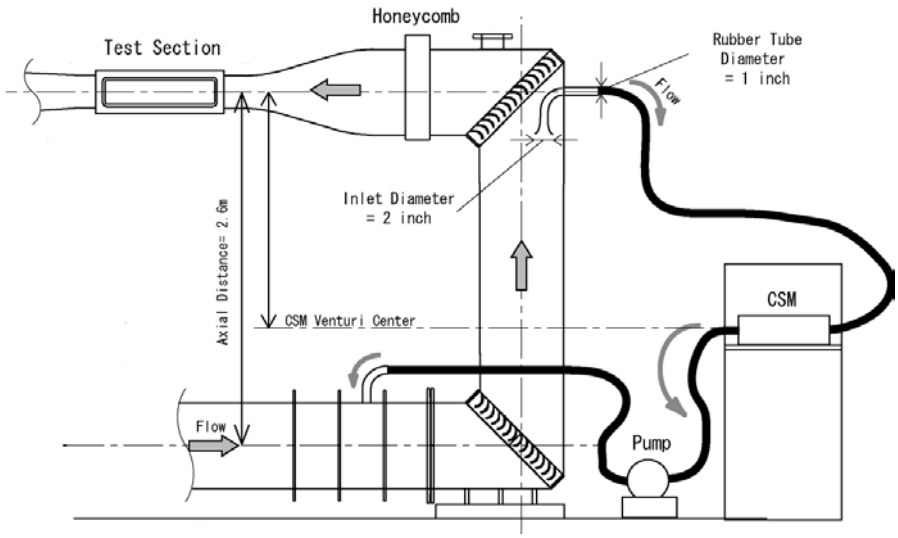

Figure 3-2: CSM set-up at University of Michigan 9 inch water tunnel

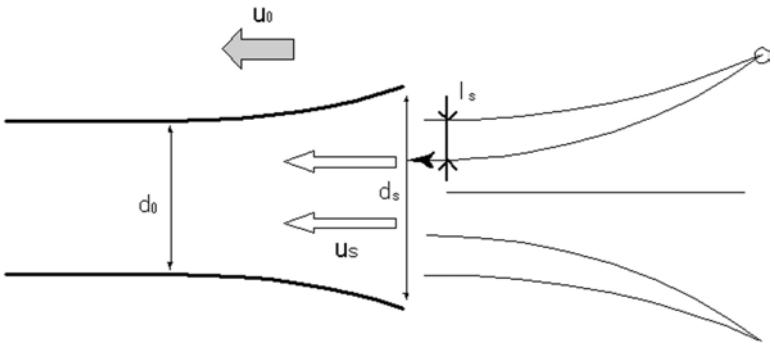

Figure 3-3: Geometry of CSM inlet

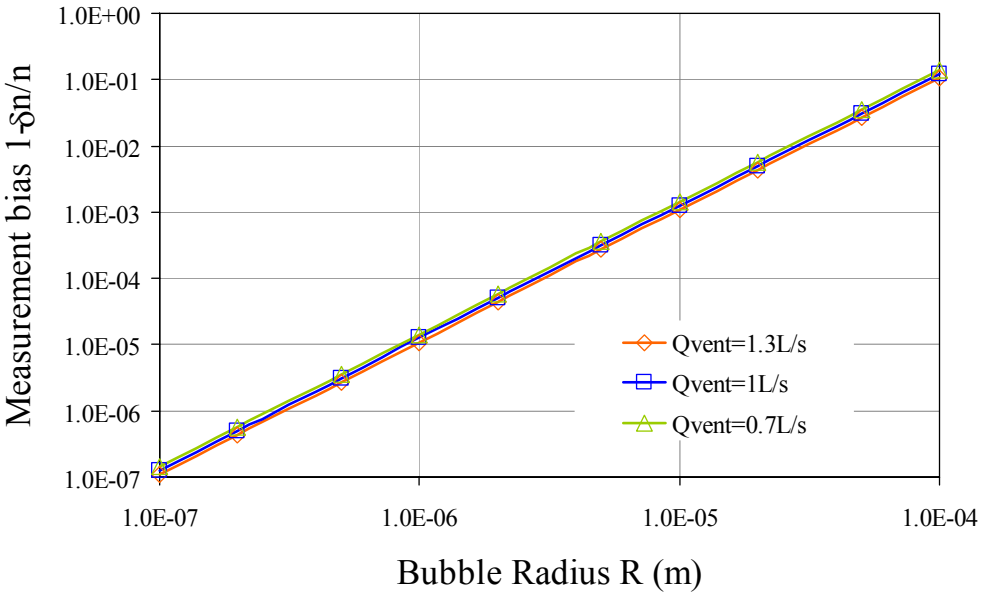

Figure 3-4: Measurement bias due to a slip velocity at inlet

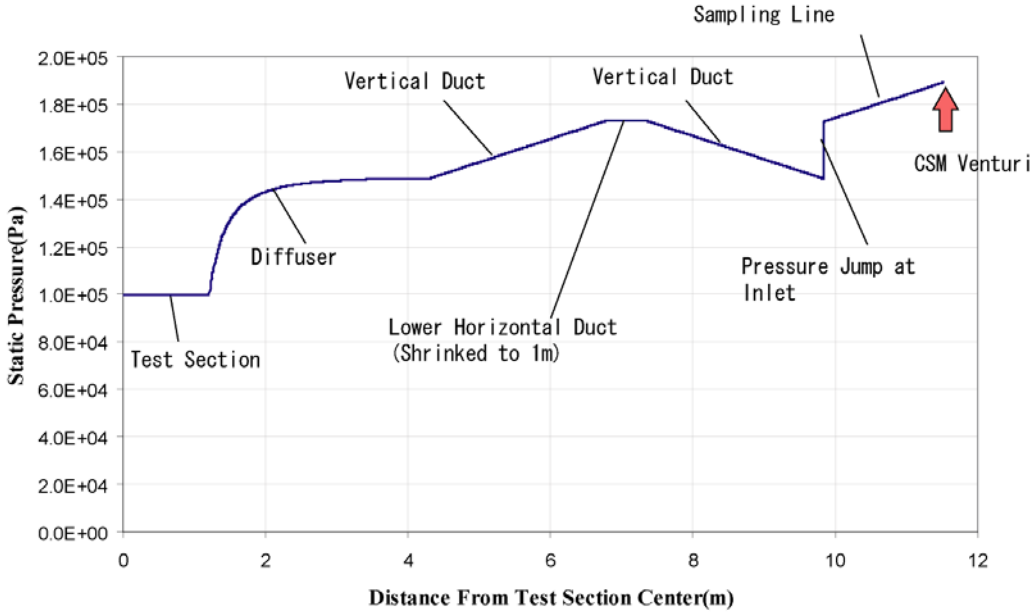

Figure 3-5: Pressure distribution along bubble trajectory from test section to CSM venturi ($P_{(test\ section)}$=10,000Pa, Q_{vent}=1e-3 m^3/s, U_{inf}=10m/s)

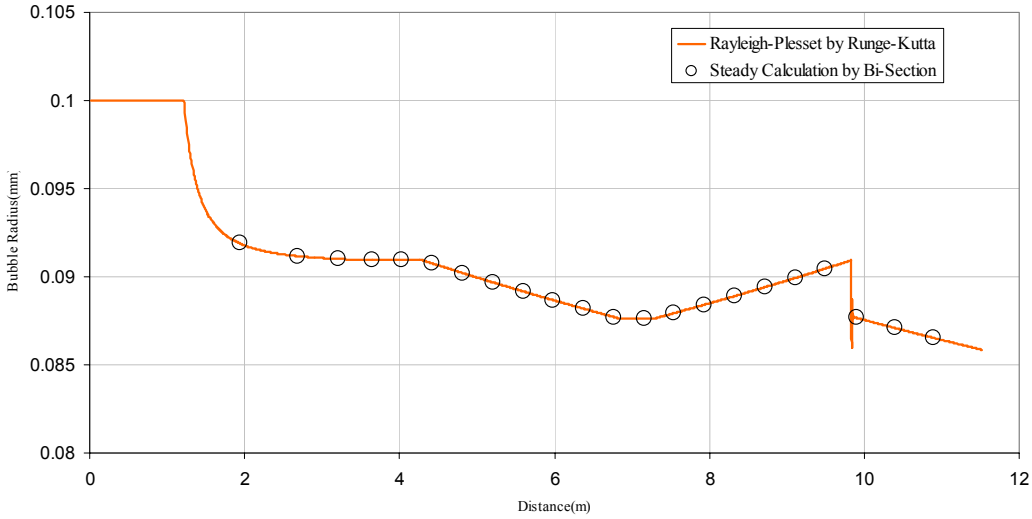

Figure 3-6: Bubble radius history for Rayleigh-Plesset equation and equilibrium condition
(Initial Bubble Raidus = 100 μm)

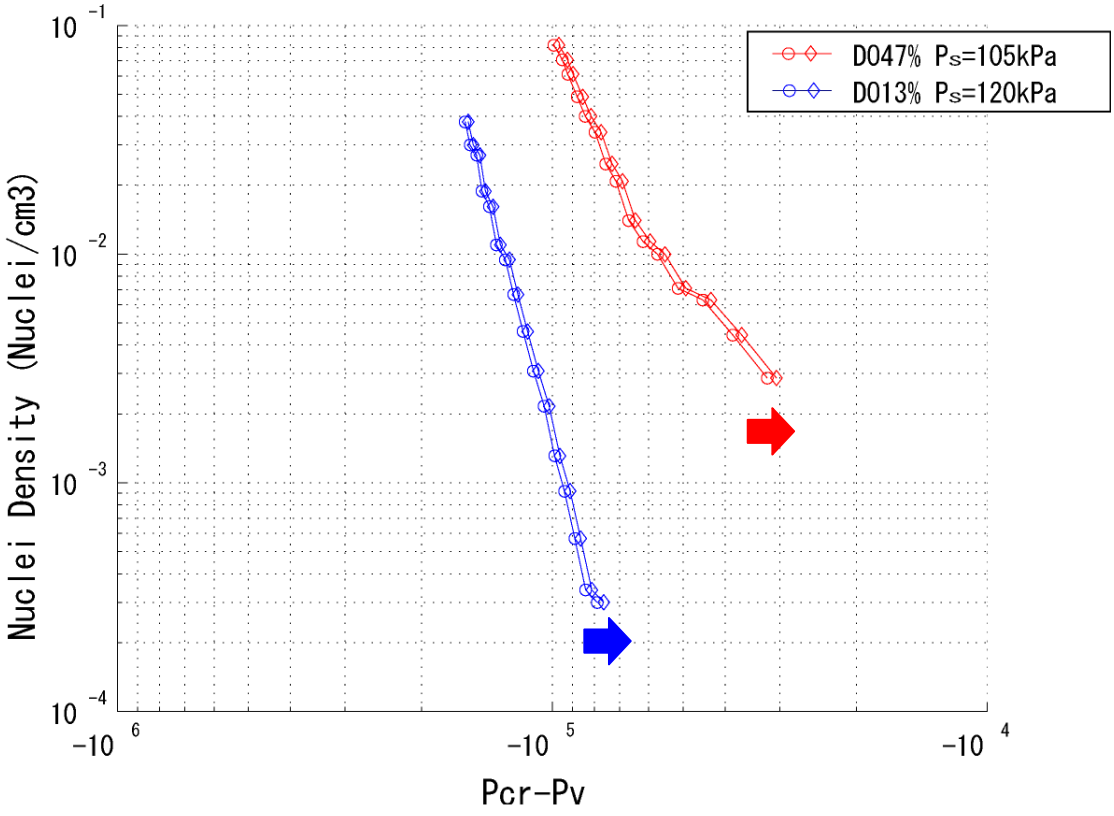

Figure 3-7: Negative tension shift due to static pressure difference

Left lines correspond to the original data obtained from CSM and it is shifted to a right line with taking account of static pressure difference.

Ps denotes the static pressure at test section.

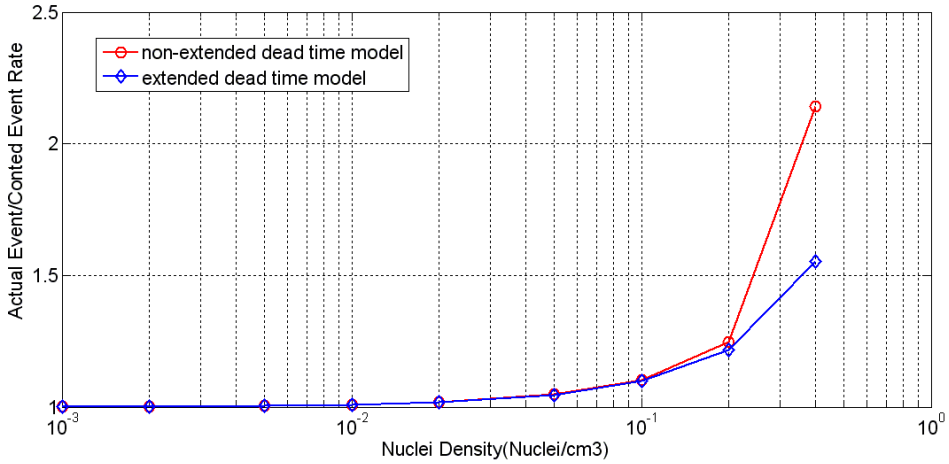

Figure 3-8: Under counting bias due to dead time

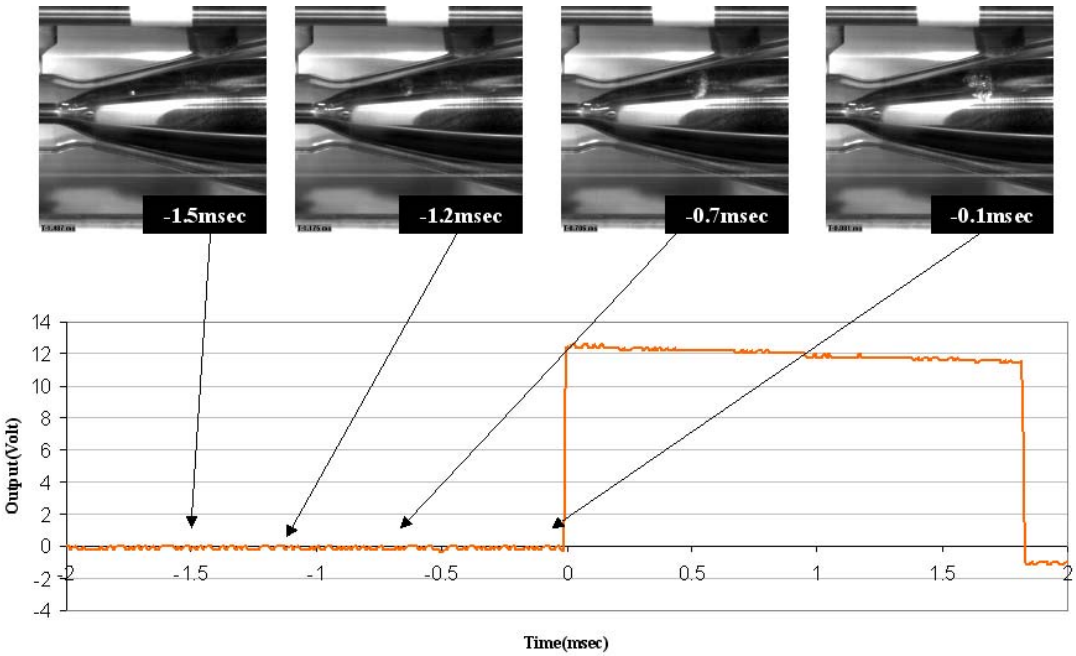

Figure 3-9: Activated bubble counted for 1 event
(U_{inf}=10m/s, P_{crit}-P_v=80kPa)

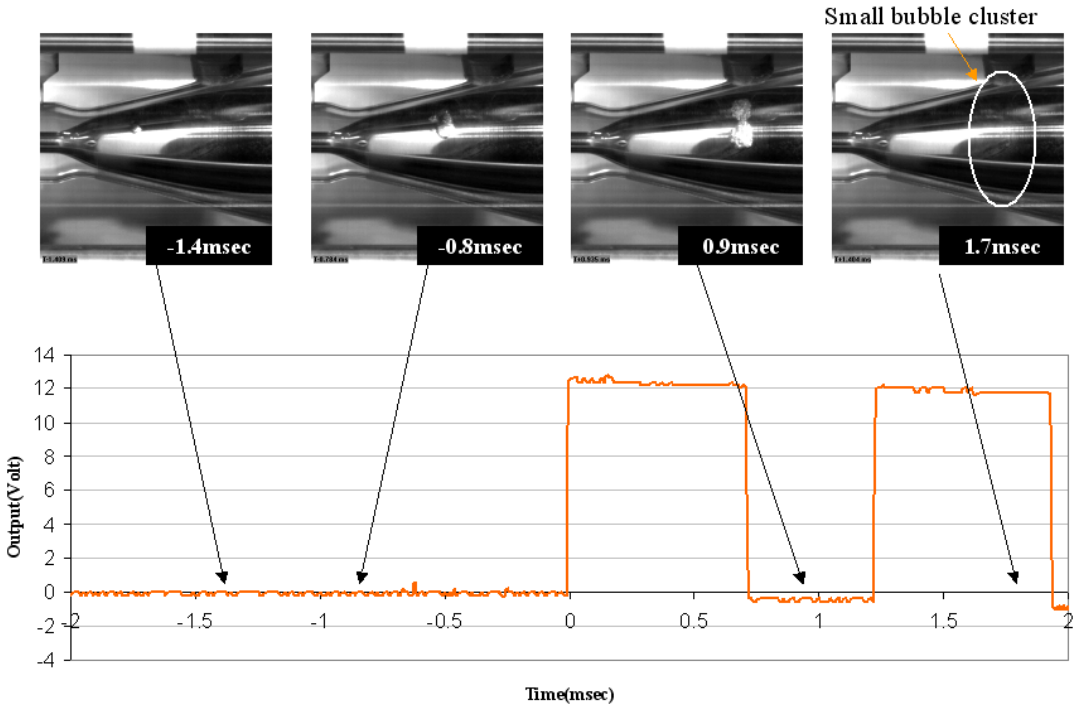

Figure 3-10: Activated bubble counted for 2 events
(U_{inf}=10m/s, P_{crit}-P_v=80kPa)

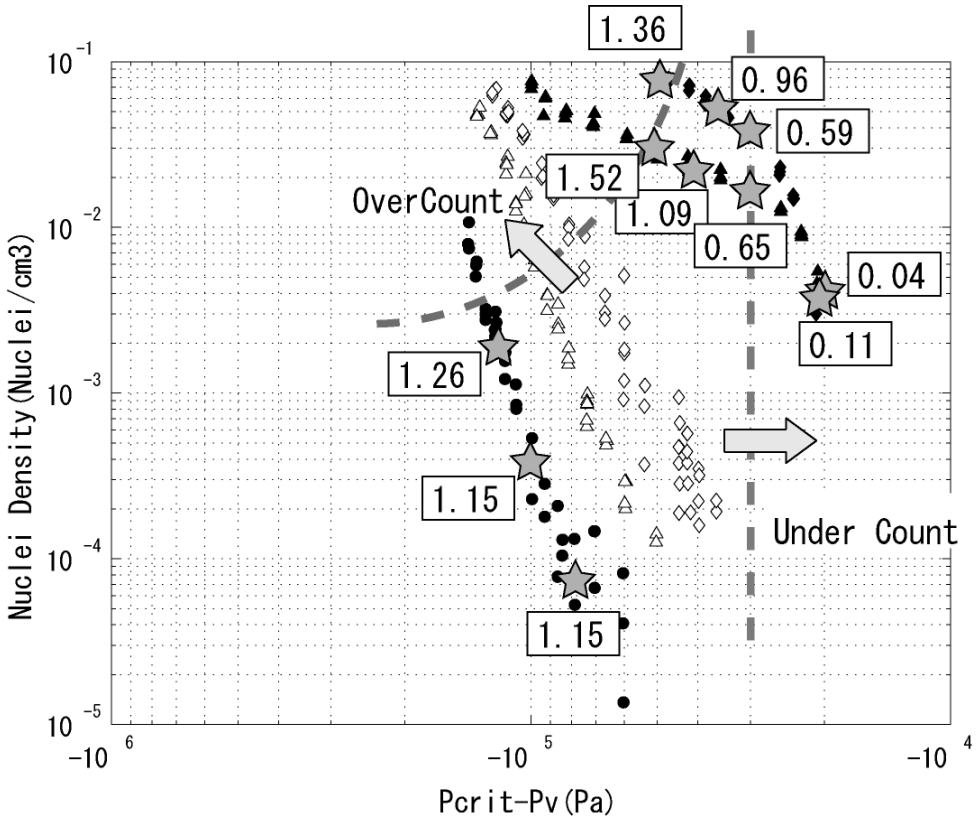

Figure 3-11: Over/Under-counting bias by a calibration with high-speed imaging

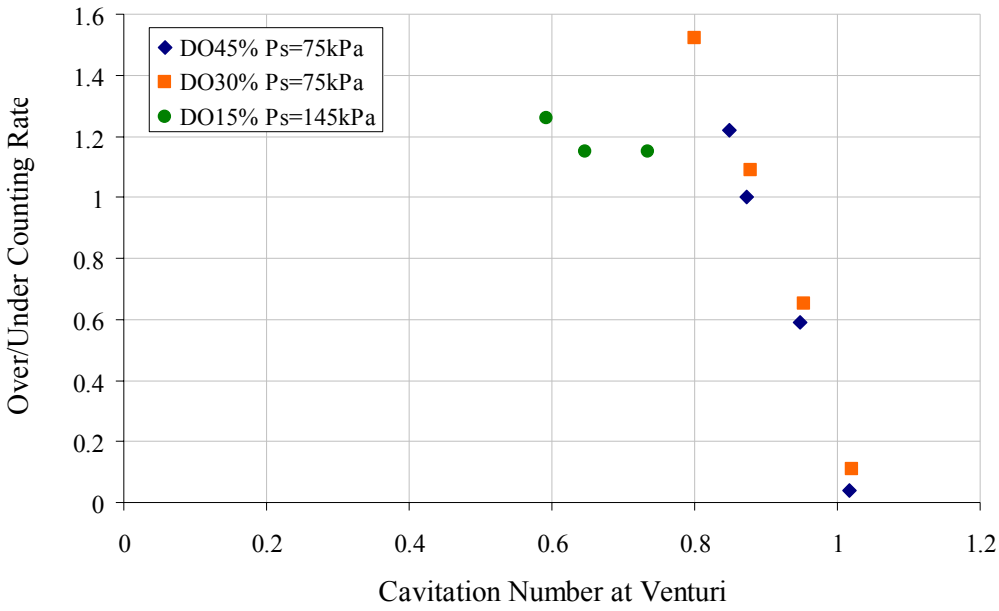

Figure 3-12: Over/Under-counting bias and cavitation number at venturi throat

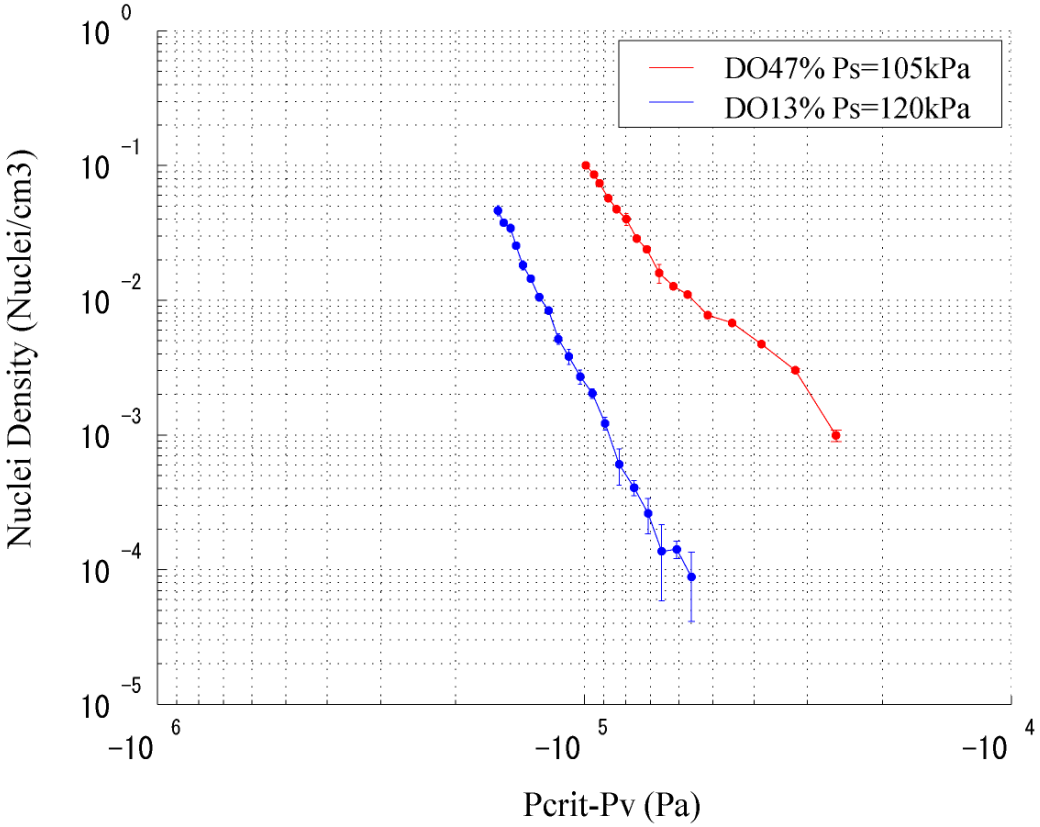

Figure 3-13: CSM measurement results

(Error bar denotes one standard deviation from 3 data sets.)

Table 3-1: Summary of Measurement Bias and Error for CSM

		Factor	Evaluation method	Maximum value	Note
1	Bias	Bubble slip velocity at inlet	numerically	At most ~10% in density	(for R=100micron bubble)
2	Bias	Static pressure difference	numerically	At most ~5% in negative tension	(at Pcrit-Pv=-25kPa)
3	Bias	Under-counting due to a dead time	numerically	At most ~10% in density	At a density is 0.1 (nuclei/cm3)
4	Bias	Over/under counting due to bubble life time	experimentally	**Can generate 10%-150% from the actual value indensity**	Dependent on a caitation number at a center body venturi
5	Uncertainty		experimentally	Can generate 50% standard deviation indensity	At very low event rate (n~1e-4(nuclei/cm3))

References

23rd ITTC, 2002, *"The Specialist Committee on Water Quality and Cavitation"*, Proceedings of 23rd International Towing Tank Conference, Vol.2, pp459-491

Chahine, G. L., Kalumuck, K. M., Cheng, J-Y. Frederick **,** G. S. , 2001*, "Validation of Bubble Distribution Measurements of the ABS Acoustic Bubble Spectrometer with High Speed Video Photography"*, Fourth International Symposium on Cavitation, Pasadena, CA,

Franc, J.P., Michel, J.M., 2004, *"Fundamentals of Cavitation"*, Grenoble Sciences

Freisch, J., 2000, *"Ten Years of Research in Hydrodynamics and Cavitation Tunnel HYKAT of HSVA"*, NCT'50 International Conference on Propeller Cavitation, Newcastle upon Tyne, U.K.

Gindroz, B., Briancon-Marjollet, L., 1992, *"Experimental Comparison between Different Techniques of Cavitation Nuclei Measurement"*, Proceedings of 2nd International Symposium on Propeller and Cavitation, Hangzhou, China

Gowing, S., 1999, *"Comparison of a Centerbody and a Standard Cavitation Susceptibility Meter"*, 3rd ASME/JSME Joint Fluids Engineering Conference, San Francisco, USA

Ida, T., 2007, *"Monte Carlo simulation of the effect of counting losses on measured X-ray intensities"*, Journal of Applied Crystallography, Vol. 40(5), pp.964-965

Kato, H. ,Yamaguchi, H., Maeda, M, Kawanami, Y., Nakasumi, S., 1999, "*Laser Holographic Observation of Cavitation Cloud on a Foil Section"*, J. Visualization, The Visualization Society of Japan and Ohmsha, Ltd., Vol.2, No1 pp.37-50

Nagaya, S., Yakushiji, R., *"Measurement Technique for Cavitation Nuclei Distribution in a Cavitation Tunnel"*, Technical Report 6899, Technical Research and Development Institute, Japan Defense Agency, September 2005, (in Japanese)

Oldenziel, D.M., 1982, *"A New Instrument in Cavitation Research: The Cavitation Susceptibility Meter"*, Journal lf Fluids Engineering, Vol. 104, pp.136-142

Pham, T.H., Michel, J.M., Lecoffre, Y., 1995 *"Development of a New Type of CSM: Design Concepts and Investigation of Performance Characteristics"*, International Symposium on Cavitation CAV'95, Deauville, France

Chapter Four

Polymer Injection System and Other Experiment Set-up

The general experiment set-up of the present study carried out in 9inch cavitation tunnel in the University of Michigan is explained in this chapter. The description focuses on a polymer injection system and the polymer degradation due to a shear flow in the injection line.

4.1 Water Tunnel

University of Michigan's 9-inch water tunnel was used for this study (see Figure 4-1). The test section has 228mm (=9 inch) square shape with rounded corner. The contraction ratio is 6.4, and the flow turbulence level was controlled by a honeycomb located upstream from the contraction. The water velocity in the tunnel was propelled by a mixed flow pump at the lower duct. The tunnel was connected to a small pressure control tank, and the static pressure in the tunnel was controlled by changing the air pressure in this tank.

The flow velocity was measured by taking a differential pressure measurement at the contraction. The differential pressure gauge OMEGA PX83DI-075D5T was used and calibrated with water head. The velocity obtained from the pressure difference was calibrated with 2-D PIV measurement in the test section center and its error was 0.1% at the hydrofoil mount location.

The static pressure was measured at upstream from the entrance of the test section by an OMEGA PX203-030A5V. The idea of locating a static pressure sensor at upstream from the test section was to avoid a pressure fluctuation due to cavitation of a test model. As the measurement point was not exactly located in the test section, the difference of the static pressure between the measurement point and the foil location was measured when no model was put on the test section. The static pressure at the "foil location" is located on the sidewall on the test section beside the foil tip and the location is shown in Figure 4-6. The static pressure at the test section was obtained by using this correlation.

Finally, the cavitation number at the test section is calculated by the following equation.

$$\sigma_\infty = \frac{P_S - P_V}{\frac{1}{2}\rho \cdot U_{\inf}{}^2} \qquad \text{(eq. 4-1)}$$

P_S ; Static pressure at test section (Pa) (as shown in Figure 4-6*)*

ρ ; density of water (kg/m3)

$U_{\inf}$; Test section velocity from differential pressure (m/s)

The standard deviation due to a time series fluctuation of the cavitation number was calculated to be 0.1. Then the total error on cavitation number σ_∞ was estimated to be +/-0.3, and the main source is the velocity measurement error.

4.2 Hydrofoil

4.2.1 Geometry

An elliptic plan form foil was used for this study. Its chord length and half-span length was 114.3mm and respective aspect ratio is 0.785. The foil's profile is NACA66 modified by DTRC (David Taylor Research Center) given in Figure 4-5 and Table 4-1. The maximum ratio of the thickness to chord is 0.099. The foil is made of brass and an injection hole was drilled from the root to its tip. The details of the injection line are shown in Figure 4-2 and Figure 4-3.

4.2.2 Behavior of Injected Polymer

Figure 4-4 is the high-speed video images on the behavior of injected polymer near by the injection hole. (a) was taken in the "non-injection" condition and TVC is fully developed at this static pressure (σ=2.8). This bubble tube is thought to be the tip vortex path. (b) and (c) was taken in the condition with polymer injection. At the smaller injection flow rate (Q_{jet}=2.8(cc/s) in (b)), the injection velocity from the hole, V_{jet} is estimated to be 0.7 (m/s) from the following equation. This corresponds to 9% of the uniform velocity, U_{inf}=8(m/s). In the larger flow-rate case (Q_{jet}=22.6(cc/s) in (c)), V_{jet} is estimated to be 11.2(m/s) and this is 140% of the uniform velocity.

$$V_{jet} = \frac{Q_{jet}}{S_{injectionhole}} \qquad \text{(eq. 4-2)}$$

$S_{injectionhole}$ *; Sectional area of injection hole (2.01 e-6 (m^2))*

At both flow rates ((b) and (c)), we can see that the injected polymer is entrained in to the vortex core just nearby the injection hole outlet.

4.2.3 Injection hole effect on cavitation inception

Since the injection hole changed geometry of on the foil, this can introduce a local cavitation due to the edge or other secondary vortex. Therefore, the cavitation inception point of the foil used here has to be compared with the data for the original foil.

As this study is using the same geometry as Souders (1981), the cavitation inception point form their study can be used for the reference. In Souders' study, the cavitation inception point was given as follows (for Re=2.5e6).

$$\sigma_i = 14.7 C_L^{\,2} \qquad \text{(eq. 4-3)}$$

For our case, C_L for α = 8 degrees is 0.574. But we need to correlate Reynolds number effect by using McCormick's law given in (eq. 2-1). (In our case, Reynolds number based on the foil root length is 9.0e5.)

Finally, the cavitation inception point in our study is estimated to be σ_i=3.2. The still picture for this study is shown in Figure 5-1 and the activated bubble was captured in the picture of σ=3.1. In our study, the cavitation inception point in "non-injection case" was defined to be σ_i=3.5. However the cavitation inception point detected by a laser bubble detector tends to give a higher cavitation inception point than the visual observation. Taking account of the definition of the cavitation inception point and still picture observation, the estimated cavitation inception point from an original geometry corresponds to the cavitation inception point obtained in this study with an injection hole.

4.3 Injector

Aqueous polymer solution or water was injected by a syringe pump system. The syringe pump system was composed of two Plexiglas tubes, piston heads and pushing rods connected to a step motor. 3m long PVC tube connects the syringe pump system and the foil. Before injection, polymer solution was prepared in a bucket and sucked into the syringe tube. The filling speed was always kept to be 3.3 cc/s. The injection speed was controlled by a step motor speed. By comparing with a weight measurement, the injection volume rate can have an error of 10%.

4.4 Polymer mixing procedure and polymer characterization by pressure drop

Aqueous solutions of Polyox WSR301 were used in this study. A powder of Polyox WSR301 was taken from a container and was mixed with a water to achieve a concentration of 2000 wppm. The water was taken from a city water supply and the contaminated Chlorine was removed by a sodium thiosulfate. The shower of the water was poured into a bucket and powder was seeded onto a shower of water gradually. After 24 hours, the aqueous solution becomes clear, as polymer became completely hydrated. 2500 wppm solution prepared in the above-defined procedure was kept for 2 weeks and it did not show a significant change in its rheology as measured by the procedure described below. The water was weighed with an Acculab SV-30 scale with an error of +/- 0.005kg, and the polymer was weighed with an Acculab VIC-212 scale with an error of +/- 0.01g. The polymer was then slowly added to the water while it was being stirred. The base polymer solution was at 2000 wppm, this was then diluted to the concentrations used

during testing. The polymer solution preparation was accurate to +/- 3% the final concentration achieved.

The polymer degradation was evaluated by measuring the pressure drop of a fully developed turbulent pipe flow. The pressure drop is related to the wall shear stress, which can be used to characterize the level of degradation of the polymer. The set up was composed of a long pipe and a branched pipeline to measure the pressure difference between 60 inches (see Figure 4-7). The flow rate was evaluated by a weighing the total fluid mass that flown into a bucket at the exit of the pipeline. The aqueous polymer was diluted into 10 wppm (which is thought to be enough to realize the maximum drag reduction) and placed in a pressure vessel of 30 L in capacity. The pressure vessel was pressurized by Nitrogen forcing the polymer solution to flow into the pipeline. In the first section, the flow becomes fully developed with a turbulent boundary layer. After the turbulent developing section, the tube was connected to another section to measure the pressure difference.

Results from the pressure drop measurement are plotted in Prandtl-Karman coordinates (see Figure 4-8). The vertical axis uses $1/\sqrt{f}$ (f denotes a frictional drag "coefficient" nondimensionalized by a uniform velocity) and the horizontal axis uses $\mathrm{Re}\cdot\sqrt{f}$ (Reynolds number is based on a bulk velocity in a pipe and pipe diameter). In other words, $1/\sqrt{f}$ means a ratio of bulk to turbulent velocities and $\mathrm{Re}\cdot\sqrt{f}$ can be interpreted to be the ratio of bulk to turbulent velocities.

Figure 4-8 shows the typical behavior of a polymer solution. Even though the perfect physical explanation on polymer drag reduction is still unknown, we can draw a general figure of the polymer behavior. When the flow rate is low (regime (A) in Figure 4-8), the wall boundary layer is laminar and solution behaves as water. Then, as flow rate goes up, the flow starts to have a turbulent boundary layer and the shear at the wall increases. In the polymer solution, the polymer chain structure is stretched and its recoiling is thought to change a momentum mixing process in a turbulent boundary layer. Beyond a certain point, polymer solution starts to reduce drag (regime (B)). As flow rate goes up more, this drag reduction effect is saturated. In this regime (C), a new momentum mixing process in the turbulent boundary layer is thought to be established.

Polymer solution is degraded by a high shear stress, since the high strain can break the link of polymer molecules. Winkel et al. (2008) introduced a criterion for the polymer degradation due to shear stress as follows;

$$\gamma = \frac{U}{d} < 10{,}000 \qquad \text{(eq. 4-4)}$$

As explained in the previous chapter, the polymer was injected through the narrow tube. Therefore it is necessary to know the degradation due to the shear flow in the injection tube. The flow rates used in this study and concentration are summarized in Table 4-2 and the corresponding shear rates γ were also calculated. It seems that each experiment condition does not hit the criteria given in eqn. 4-2, but may possibly have a bigger local shear rate.

The preparation and the dilution of the polymer solution described above were the same procedure used for the TVC suppression tests. Then the injector line was connected to a brass tube piece, which has the completely same geometry as the elliptic foil injector (see Figure 4-10).

As explained before, the pressure drop measurement system only can evaluate up to the maximum drag reduction polymer, whose concentration is about 10 wppm. Therefore, the polymer solutions prepared for the TVC suppression study had to be diluted into 10 wppm for the pressure drop measurement. During the dilution, it is necessary to mitigate additional degradation sources, such as the splashing of water or other possible factors, which can generate strong shear forces. To avoid additional degradation, the injector tip was put on the pressure vessel filled with a non-chlorine water. The weight of the pressure vessel and water was measured beforehand to know how much high concentration polymer has to be injected to make 10 wppm concentration. After injecting a certain amount of polymer solution from a syringe pump. The diluted 10 wppm polymer was examined through the pressure drop measurement tube.

The degradation check was done at the two different concentrations (see Table 4-2) and two different injection rates. Figure 4-11 to Figure 4-12 shows a skin friction measurement results at three different concentrations; 31wppm, 125wppm. In comparison

with a sample 10wppm polymer solution, 31wppm solution after the injection of Q_{jet}=22.6cc/s was highly degraded. The minimum shear stress causes drag reduction (which corresponds to the border between (A) and (B)) is thought to be a function of the molecular weight (the number of molecules in a link) and polymer concentration. Therefore it is possible that the 31wppm solution after the injection of Q_{jet}=11.3cc/s was slightly degraded, since the minimum drag reduction point for injection case is slightly larger than the (MDR) maximum drag reduction line. For 125 wppm concentration case, the degradation in Q_{jet}=11.3cc/s case is negligible. But the injected polymer was highly degraded in Q_{jet}=22.6cc/s. It can be expected that TVC suppression effect is reduced by this degradation, but the detail will be discussed with TVC suppression data in the next chapter.

Figure 4-1: University of Michigan 9-inch water tunnel

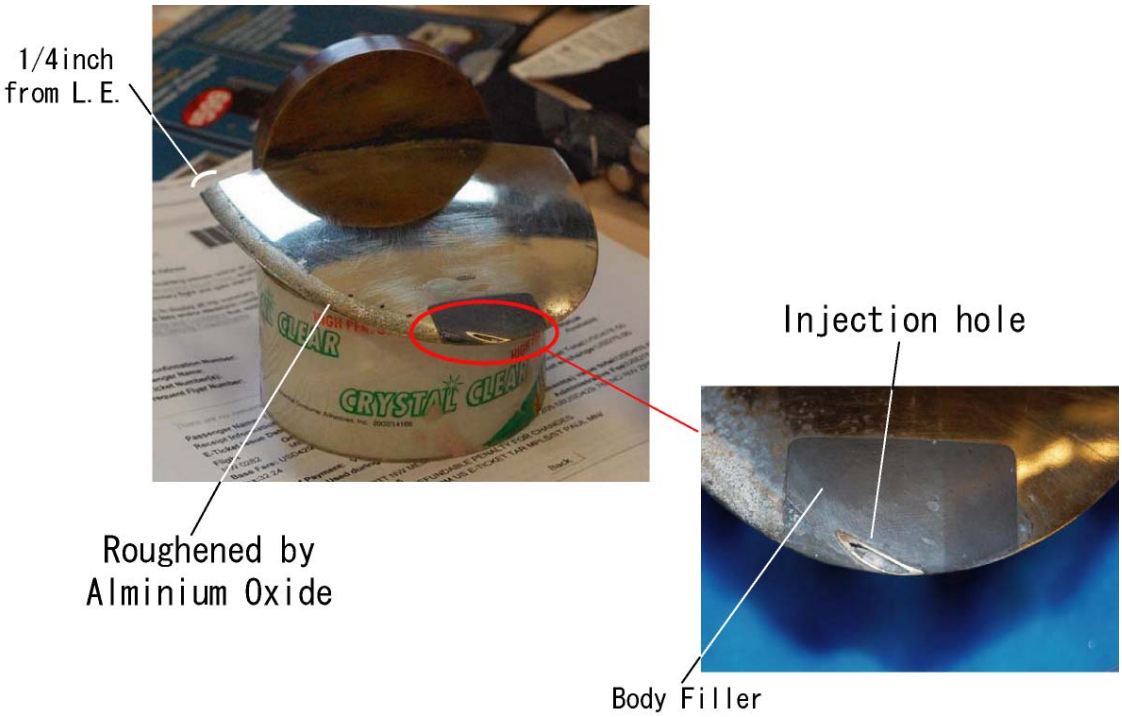

Figure 4-2: Hydrofoil model used in this study

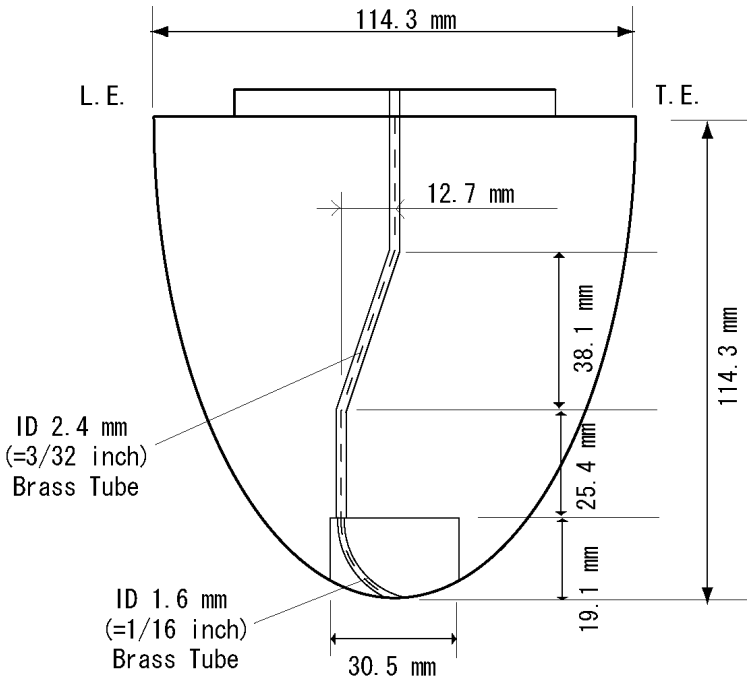

Figure 4-3: Foil geometry

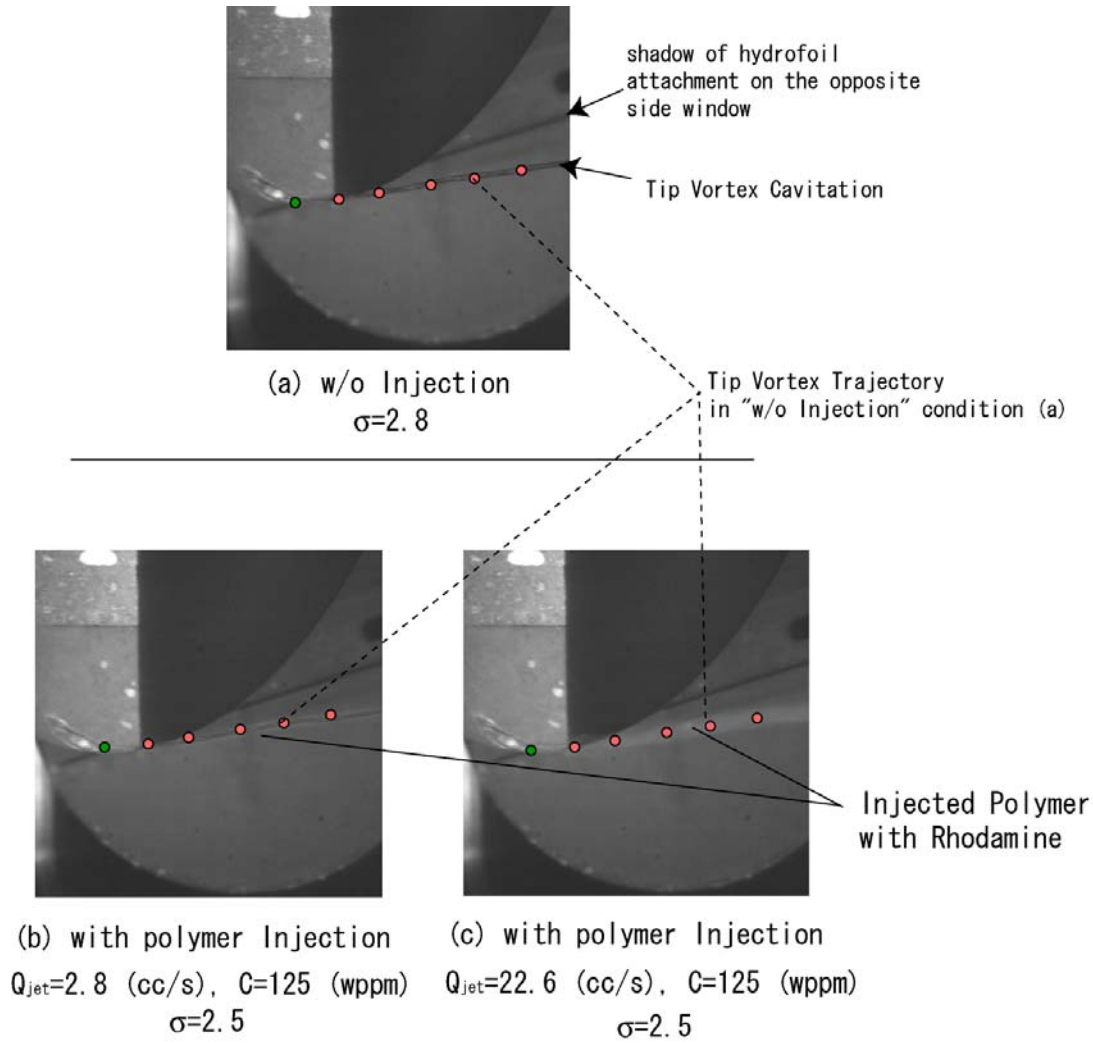

Figure 4-4: Injected polymer behavior nearby the injection hole

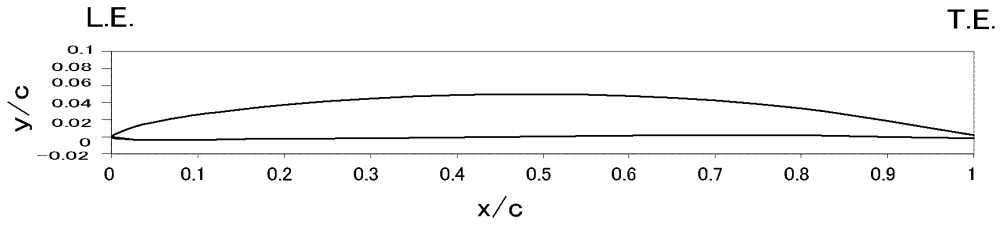

Figure 4-5: Profile of NACA66 foil used in this study

Table 4-1: Hydrofoil offset

x/c	y_upper/c	y_lower/c
0	0.0000	0.0000
0.025	0.0113	−0.0034
0.05	0.0171	−0.0036
0.1	0.0257	−0.0033
0.2	0.0375	−0.0025
0.3	0.0448	−0.0016
0.4	0.0488	−0.0008
0.5	0.0498	0.0002
0.6	0.0477	0.0012
0.7	0.0424	0.0021
0.8	0.0331	0.0020
0.9	0.0184	−0.0004
1	0.0017	−0.0017

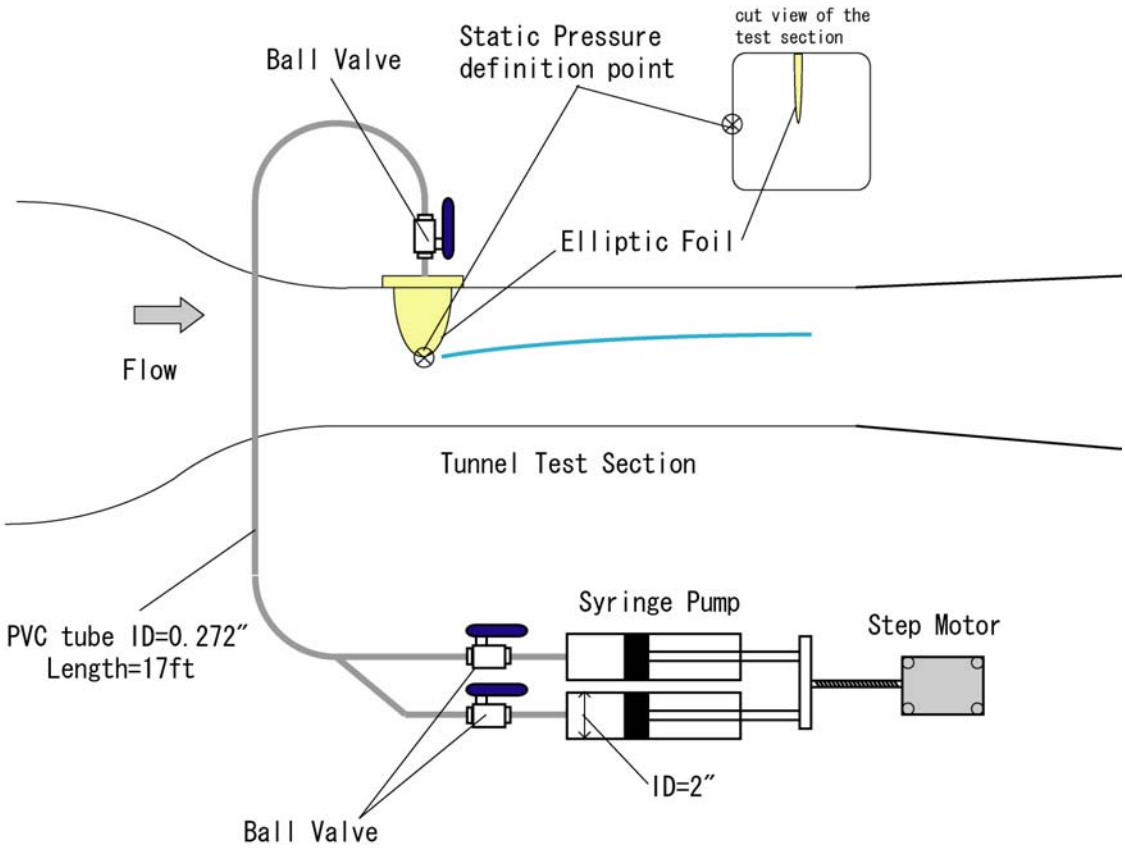

Figure 4-6: Injector and Hydrofoil

Table 4-2: Injection conditions and pressure drop measurement conditions

		Concentration C (wppm)			
Injection Flow Rate Q_{jet} (cc/s)	Shear Rate γ (s-1)	10	31	125	500
22.6	7200		○	○	
11.3	3600		○	○	
5.6	1800				
2.8	920				

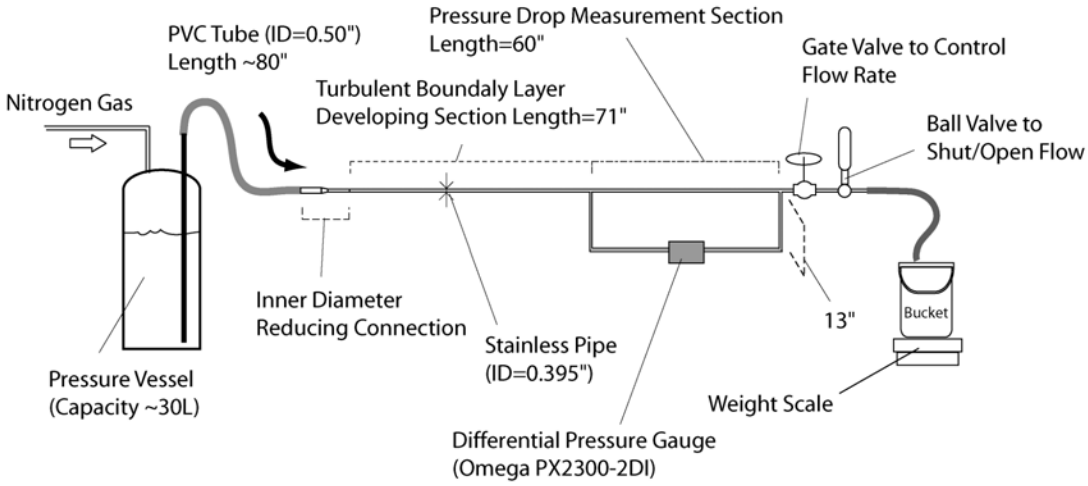

Figure 4-7: Pressure drop measurement system to characterize polymer solution

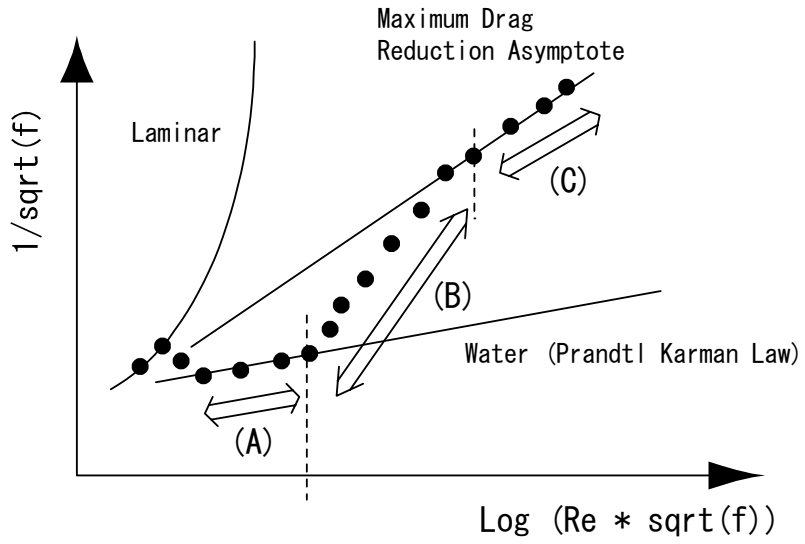

Figure 4-8: Pressure drop measurement result on Prandtl-Karman coordinate

Figure 4-9: Simulated injection hole for polymer characterization (right) and actual hydrofoil (left)

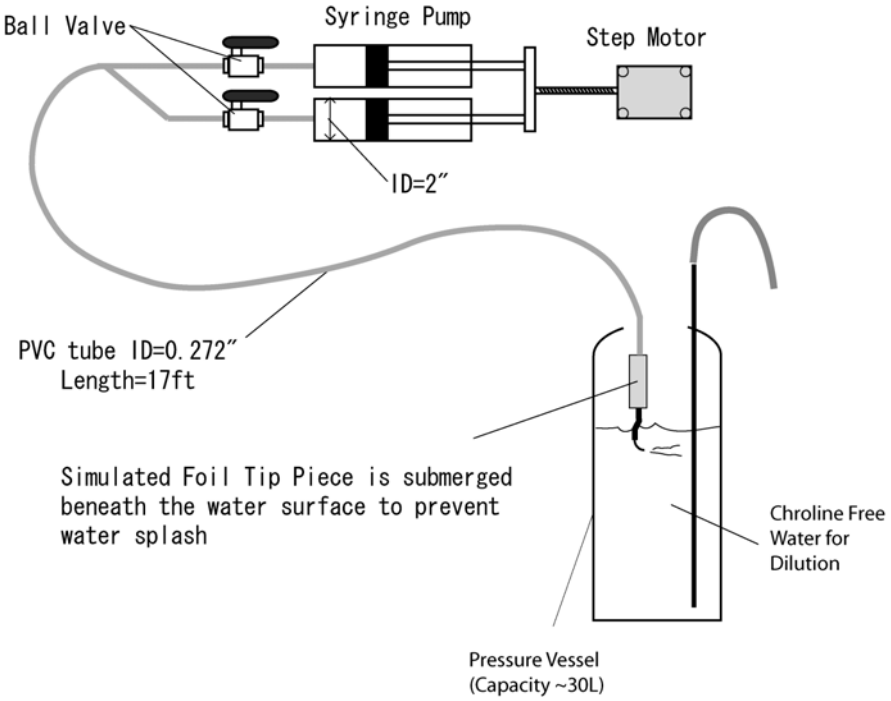

Figure 4-10: Polymer dilution procedure for degradation checks

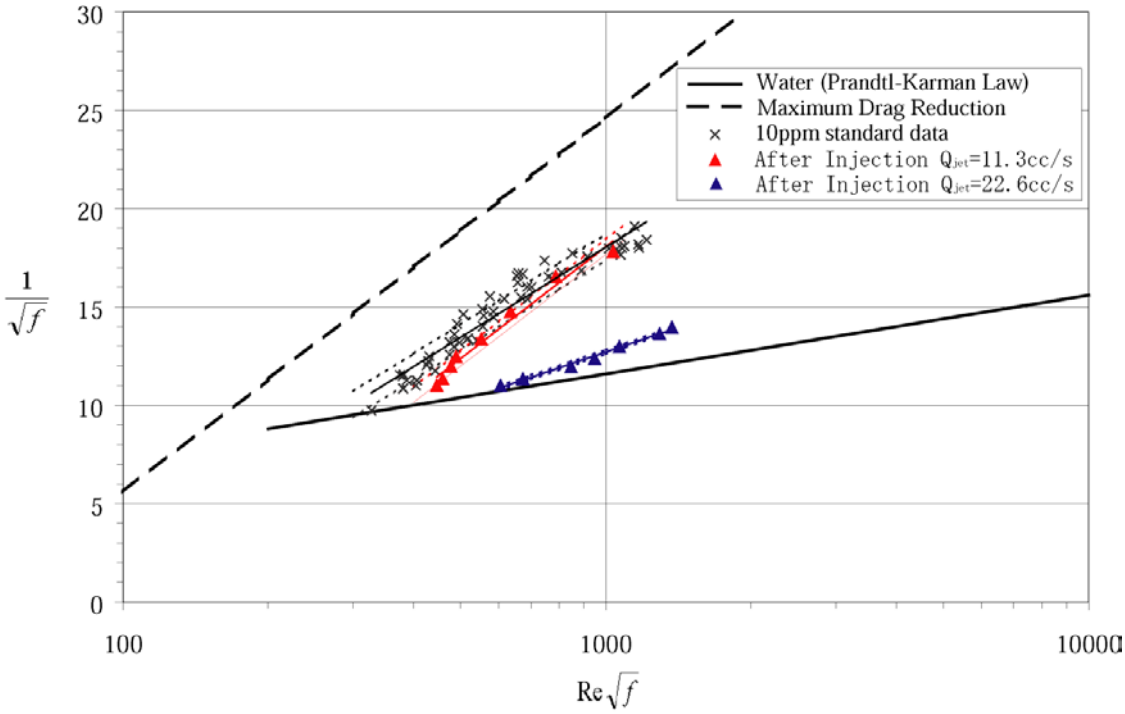

Figure 4-11: Pressure drop measurement for C=31wppm

Solid line shows a regression line and dotted line shows error bar
with average root mean square from a solid line

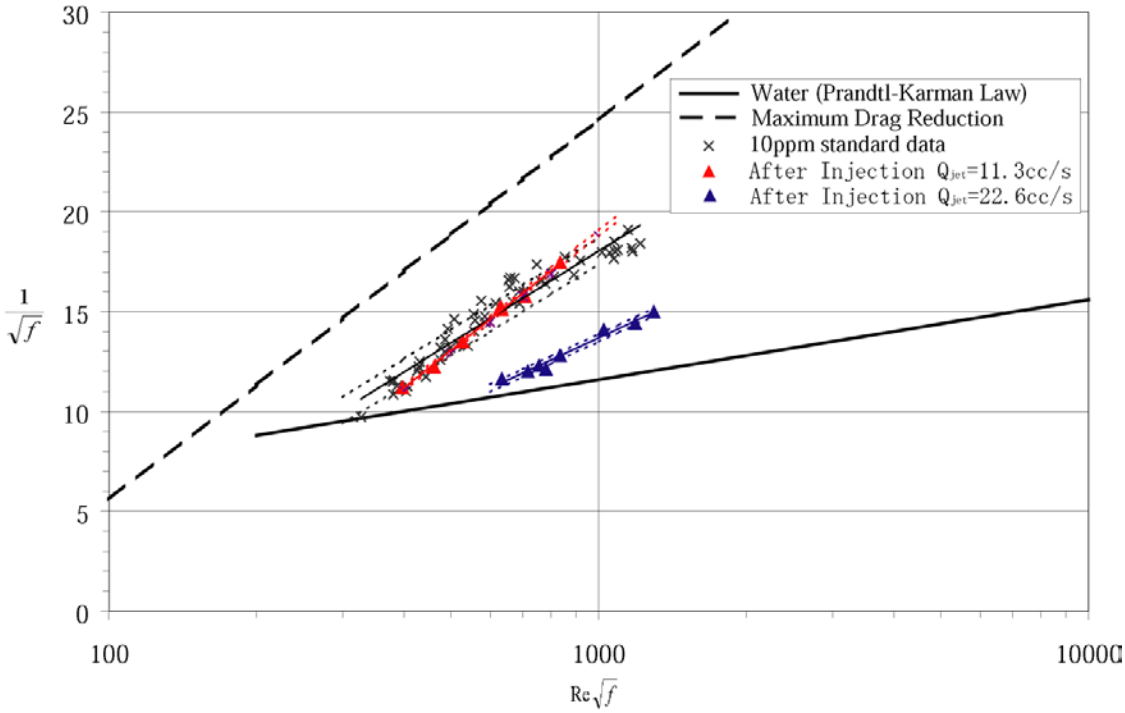

Figure 4-12: Pressure drop measurement for C=125wppm

Solid line shows a regression line and dotted line shows a error bar
with average root mean square from a solid line

References

Souder W.G., Platzer G. P., 1981, *"Tip vortex cavitation characteristics and delay of inception on a three-dimensional hydrofoil"*, DTNSRDC Technical Report 81/007

Winkel, E.S., Oweis, G., Vanapalli, S.A., Dowling, D.R., Perlin, M., Solomon, J., Ceccio, S.L., *"High Reynolds Number Turbulent Boundary Layer Friction Drag Reduction from Wall-Injected Polymer Solutions"*, submitted for Journal of Fluid Mechanics

Chapter Five

Cavitation Desinence Test

To evaluate TVC suppression effect due to polymer/water injection quantitatively, a new method to estimate cavitation desinence through bubble detection was developed and implemented in this study. Coupled with this new method, TVC suppression effect was evaluated at different polymer solution concentrations (including pure water injection) and different injection flow rates. The water quality dependence was also surveyed in comparison with nuclei measurements.

5.1 General observation on tip vortex cavitation and suppression

Figure 5-1is the pictures taken at different cavitation numbers at constant angle of attack (α=8deg) and uniform velocity (U_{inf}=8m/s). As shown in the pictures, the foil was attached from the topside window of the test section.

At high cavitation numbers ($\sigma \sim 3.1$), TVC appears as discrete bubble "sausage". As static pressure decreases, TVC becomes a continuous bubble tube and finally the bubble becomes a twisted ribbon, which was observed in Arndt's (1991) experiment.

Figure 5-2 shows pictures taken with polymer injection. The concentration and flow rate was C=125 wppm and Q_{jet}=5.6cc/s respectively. We can see that the polymer injection definitely suppresses TVC.

5.2 Cavitation Desinence definition and laser bubble detector

After the observation, TVC suppression effects were quantitatively evaluated at different polymer concentrations, including pure water, and injection flow rates. However, to evaluate TVC suppression, it is necessary to establish a quantitative method to define the " degree of cavitation". The underlying difficulty of this measurement is that the phenomenon is very discrete around cavitation inception/desinence conditions, which we observed qualitatively.

5.2.1 Review of Cavitation Inception/Desinence Detection

23rd ITTC (2002) carried out a large survey on the definition of "cavitation inception point" among marine propeller testing facilities. As with the nuclei measurement technology described in Chapter Three, they found the definition of "cavitation inception point" is no more consistent.

Visual observation is the simplest way, but it is strongly dependent on the lighting and is obviously not reliable for discrete cavitation events. Some facility use acoustic measurement. Sheet cavitation or continuous TVC can make a significant difference on the broadband noise spectrum, but it would be hard to detect a small noise on a spectrum data. "Event Rate Analysis" introduce by French research group (Gindroz et al. (1993)) used an acoustic measurement method to detect cavitation inception. In their experiment, cavitation inception point was defined as the condition, in which one acoustic peak is detected in one second. This method sounds reasonable and should correlate to nuclei density measurements, but it should be pointed out that the acoustic signal from TVC is more complicated. (Choi (2006)) showed that one activated nuclei can generate multiple peaks and this behavior is strongly dependent of the macroscopic flow structure.

5.2.2 New parameter to evaluate cavitation inception/desinence

In this study, a new method to detect a bubble existence by laser scattering was implemented. Figure 5-3 shows a general set-up for the system. He-Ne laser was fixed to shoot a laser beam in the TVC trajectory. To control the light intensity, a laser attenuator and series of color filters were placed on the laser path. On the opposite side of the test section, a photo diode was aligned to measure the brightness of the laser once it traversed the water tunnel test section. The photo diode generates a voltage signal, proportional to

the number of photons coming in. When there is a bubble in the path of the laser, the laser is scattered. On the contrary, the laser directly shoots the photo diode, when the bubble is absent. By taking a time series signal from a photo diode, the existence of the bubble at a specific location can be determined.

In the early stage of this research, the author aimed to count the number of bubble by counting the number of peaks. However, the results were not consistent for the same experimental condition. Figure 5-4 shows still picture images taken at the same experiment condition. As we can see, a long continuous bubble can split into many bubbles due to a small fluctuation of environmental conditions (i.e. static pressure, water properties). Instead of using the number of bubbles, a new parameter showing the "degree of cavitation" is introduced in this study.

From the voltage signals from the photo diode, the ratio between the time lengths, in which the voltage is lower than a certain threshold (T1) and the total measurement time length (T2) can be calculated (see Figure 5-5). Since the voltage signal decreases when a bubble exists on the vortex path, T1 can be thought to be the time length where bubbles exist at a specific measurement point.

5.2.3 Calibration with high-speed video images

The threshold value, T1, for establishing the detection of a bubble was established in conjunction with a high-speed video camera. A high-speed camera was placed under the test section to see the bubbles flowing through the laser path. Then the images were taken at 3 different cavitation numbers, in which TVC starts to incept visually. The images were analyzed by a Matlab image-processing program, detecting edge of the bubbles. For each image, the horizontal length of bubble is integrated (L1 in Figure 5-6) and ratio to the total inspection length (L2) was taken. For photodiode signal, 10 sets of 10-second data are taken and the same length data was taken by high-speed video camera. However, it should be noted that both measurement could not be done simultaneously, since the high intensity light affects a photodiode signal. Therefore, during the calibration, the test section pressure was controlled first, then photodiode signal measurement and high speed video imaging were done in independently. Figure 5-7 shows a result from both measurement and the error bar shows one standard deviation from 10 data sets. By

changing the threshold levels, 2.7 Volt (90% from the full scale of photodiode signal) was found to be the best matching value. At "non-bubble condition", the output from a photodiode has a standard deviation of 0.015 Volt. Therefore, this threshold is enough large to avoid the inherent signal fluctuation.

5.3 Test matrix and experiment procedure for desinence test

The series of cavitation desinence tests were carried out among the different polymer concentrations and injection flow rates, summarized in Table 5-1. In this sequence, dissolved oxygen content rate of the water tunnel was controlled to between DO=20% to 30%. City water, which was expected to have saturated oxygen content rate, was used to dilute the polymer solution. The effect on the oxygen content rate (or nuclei density) was evaluated and the results are at the end of this chapter.

The laser bubble detector was aligned at z/c=200%, since the tip vortex is fully rolled –up at this far down stream position and nuclei entrapment effect is also saturated. The attack angle of the foil and the uniform velocity in the test section was kept at α=8deg and U_{inf}=8m/s respectively (see Figure 5-8).

In the experiment, only one concentration polymer can be tested in one day, because the whole preparation and data acquisition takes 5-6 hours. The specific concentration was prepared by a few hours prior to the data acquisition. In the data acquisition stage, the test section pressure was lowered enough to have a continuous TVC without injection. After the static pressure was stabilized, 10-second voltage signal from the photodiode was acquired without injection and the same measurement was repeated for polymer injection case with different flow rates. Then the static pressure was gradually increased to the next static pressure and the measurement was repeated. The cavitation number, σ was increased until bubbles were not detected in the test section in the "non-injection" case.

Figure 5-9 is the plot of T1/T2 versus cavitation numbers taken in "non-injection condition" and "with injection condition", the corresponding still picture images are shown in Figure 5-1.

The cavitation desinence point in this study was defined as follows. As cavitation number increases, T1/T2 value decreases. The cavitation number in which T1/T2 line crosses 0.01 is called to be "cavitation desinence point", $\sigma_{d,}$ in this study.

5.4 Results from desinence test

Figure 5-10 to Figure 5-14 shows the results from each concentration. It was found that the higher concentrations suppressed the desinence cavitation more, but in higher concentration, suppression effect was saturated at higher injection rates.

5.4.1 New parameter to compare with past works

To compare the result with the previous works on TVC suppression by polymer/water injection, a new parameter Q_{jet}/Q_{core}, which shows how much polymer was injected into the vortex core is introduced here. Q_{jet} is the volumetric flux injected and it can be obtained from the injector speed. On the other hand, Q_{core} is the volumetric flux of vortex core estimated by the following calculation. Figure 5-15 shows the conceptual idea and the definition of those values.

In the classical theory, the vortex is expected to have the Gaussian distribution of the vorticity and it has the tangential velocity profile shown and its radial profile is given by the following equation.

$$v_t(r) = \frac{\Gamma_0}{2\pi r}\left(1 - \exp\left(-k_1 (r/r_c)^2\right)\right) \qquad \text{(eq. 5-1)}$$

$v_t(r)$; *tangential velocity*

Γ_0 *; circulation of vortex*

r_c *; vortex core radius*

k_1 ; *constant =1.255*

Due to the viscosity, the vortex center has a "viscous core". Q_{core} is the value by multiplying the section area of this vortex core and uniform velocity.

$$Q_{core} = U_{\inf} S_{core} \quad \text{(eq. 5-2)}$$

U_{inf}: Uniform velocity (m/s)

S_{core}: Sectional area of the vortex core(m^2)

To obtain an exact section area, the flow measurement is required. However, since several previous works do not have velocity measurement data, the viscous core size was estimated under the assumption that the viscous core diameter is the same as the turbulent boundary layer thickness based on the root chord length.

$$S_{core} = \pi \frac{d_c^{\,2}}{4}$$

$$d_c = 2r_c \sim \delta$$

d_c: vortex core diameter (m)

r_c: vortex core radius(m)

δ: boundary layer thickness(m)

In Fruman (1995)'s study, the flow around the tip vortex is measured by LDV. The viscous core radius r_c was 0.8 mm at z/c=25%. For their experiment, the turbulent boundary layer thickness was calculated using Schlichting's relationship.

$$\delta = 0.37 \cdot C_{Root} \left[\mathrm{Re}_{Root}\right]^{-0.2} \quad \text{(eq. 5-3)}$$

$$\mathrm{Re}_{Root} = \frac{U_{\inf} \cdot C_{Root}}{\nu} \quad \text{(eq. 5-4)}$$

C_{Root} ; chord length at root

This estimation gives δ=1.87mm and the core diameter (=$2r_c$) is 86% of the estimated value. Therefore, it can be justified the assumption is not far from the actual value.

For a marine propeller, TBL thickness was obtained based on a propeller diameter. Instead of using a Reynolds number based on the root chord length, the Reynolds number (Kempf's Reynolds number) was obtained from the propeller diameter and the propeller rotation speed.

$$\mathrm{Re}_{Kempf} = 0.7\frac{nD^2}{\nu}$$

n: propeller rotation rate (rps)

D: propeller diameter (m)

Chesnakas et al. (1998) carried out a intensive flow field measurement for propeller wake and the vortex core size obtained to be r_c= 10.1mm. For this case, TBL thickness based on the propeller diameter is 5.9mm. Therefore, it can be concluded that the vortex core size estimation is also not unreasonable for the model propeller.

Table 5-2 shows the actual values of injection flow rate, Q_{jet}, and values of estimated vortex core flux rate Q_{core} for the past studies. Table 5-3 summarizes a polymer/water injection condition in comparison with past studies . As shown, the injection volume in this study covers wider range than previous works.

5.4.2 Discussion and Comparison with past works

To gauge the improvement the difference between the baseline value, σ_b, taken in "non-injection condition" and the tested cases cavitation desinence number, σ_d, were plotted against concentration and Q_{jet}/Q_{core}. As these values increased, the suppression effect does not increase proportionally (see Figure 5-16). It can also be observed that the effect was linear with volumetric neither flow rates nor concentration (see Figure 5-17).

Consequently it was expected that the concentration, C (wppm), times Q_{jet}/Q_{core} which represents the flux of polymer with respect to the vortex core volume flux, would show the same trend (see Figure 5-18). Unlike in previous studies where the effect was saturated, the parameter range tested in this study was able to capture the progression of the TVC suppression. It was found that in a semi-log scale they generated a set of parallel lines, so consistent trends can be observed.

Fruman et al. (1995) observed TVC suppression effect was lower by a factor of two compared to the effect observed in this effort. The difference between these two studies could be due to the injection port location, which Chahine et al. (1993) noted to be of importance. The discrepancy could also be due to an error in the core size estimation of the present effort.

Figure 5-18 does not attempt to separate the TVC suppression effect of a fluid injected to the core and the added effect of the polymer in this fluid. It was assumed that the mass injection and the polymer effect on cavitation suppression were independent of each other, and can be linearly added. Therefore the TVC suppression effect of the injected mass, σ_m, was estimated for the different flow rates used by directly obtaining them through water injection experiments, or estimating their value from linear interpolation from two adjacent experimental data points. Figure 5-19 attempts to show the TVC suppression effect in a semi-log plot due to the polymer, and polymer flux rate only.

Figure 5-20 shows that the present effort results have similar trends as Souders and Platzer's (1981) data for active water injection. The similarity implies that Q_{jet}/ Q_{core} can be a scaling factor.

5.4.3 Water quality dependence

Previous studies related TVC suppression physics to a flow structure, but there should be other factors, which can contribute the suppression. Chahine and Fruman (1979) carried out the experiment to evaluate how a polymer solution affects on the bubble dynamics. They reported that the bubble dynamics was not changed drastically enough to generate a significant TVC suppression. However, another factor, the nuclei distribution in the injected polymer or water in the tunnel, may probably control the TVC suppression.

To evaluate the nuclei dependence, two sets of experiment were carried out. For the first one, two different nuclei distribution in the water tunnel was tested for the same polymer solution. In addition to that, polymer solutions with two different oxygen content rates were tested.

For the first test, the same polymer solutions were prepared by using city water (which was expected to have saturated dissolved oxygen). In the first step of the experiment, the cavitation desinence test was conducted with oxygen content rate of DO=50%. Then the nuclei distribution was measured just after the desinence test. In the next step, water in the tunnel was highly degassed to DO=19% and the same desinence test and CSM measurement were done.

For the second test, two different polymer solutions were prepared. 2500 wppm polymer solution was diluted with city water (expected to have a saturated oxygen rate) and highly degassed water taken from the water tunnel (DO=19%). Two different polymer solutions were tested in the highly degassed tunnel water (DO=19%).

As shown in Figure 5-22, the nuclei content in the aqueous polymer solution doesn't affect the result. On the other hand, TVC suppression effect was shifted for different "background" nuclei distribution, as we can see in Figure 5-21. However, the shifted distance is not the same for DO=19% case and 50% case. In other words, TVC suppression effect at Figure 5-23 shows the nuclei distribution measured by CSM in DO=19% and DO=50%. It should be pointed out that the nuclei distribution in DO=19% is dependent on the static pressure and the nuclei density increases in lower static pressure. This can account for the inconsistent shift in Figure 5-21.

The above data and discussion would support that the nuclei distribution in the water tunnel background controls TVC inception in both "non-injection" and "polymer injection cases". From those experiments, it can be inferred that the primary factor controlling the TVC suppression is the flow field modification due to polymer injection.

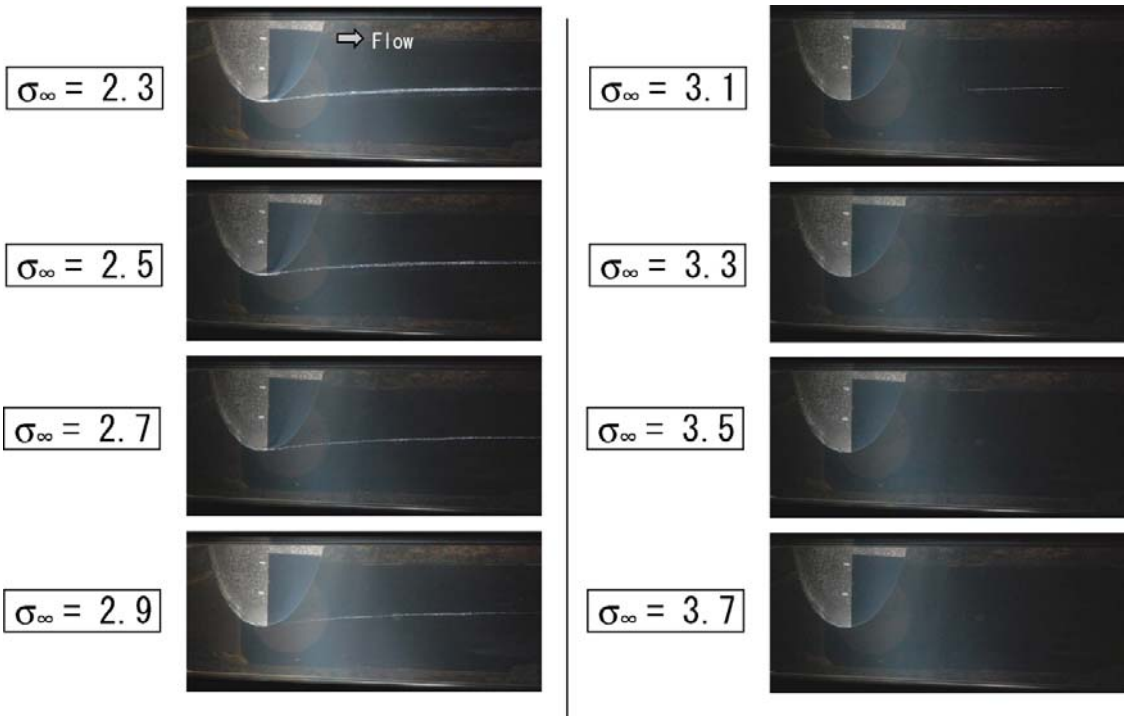

Figure 5-1: Cavitation appearance without injection (U_{inf}=8m/s α=8deg)

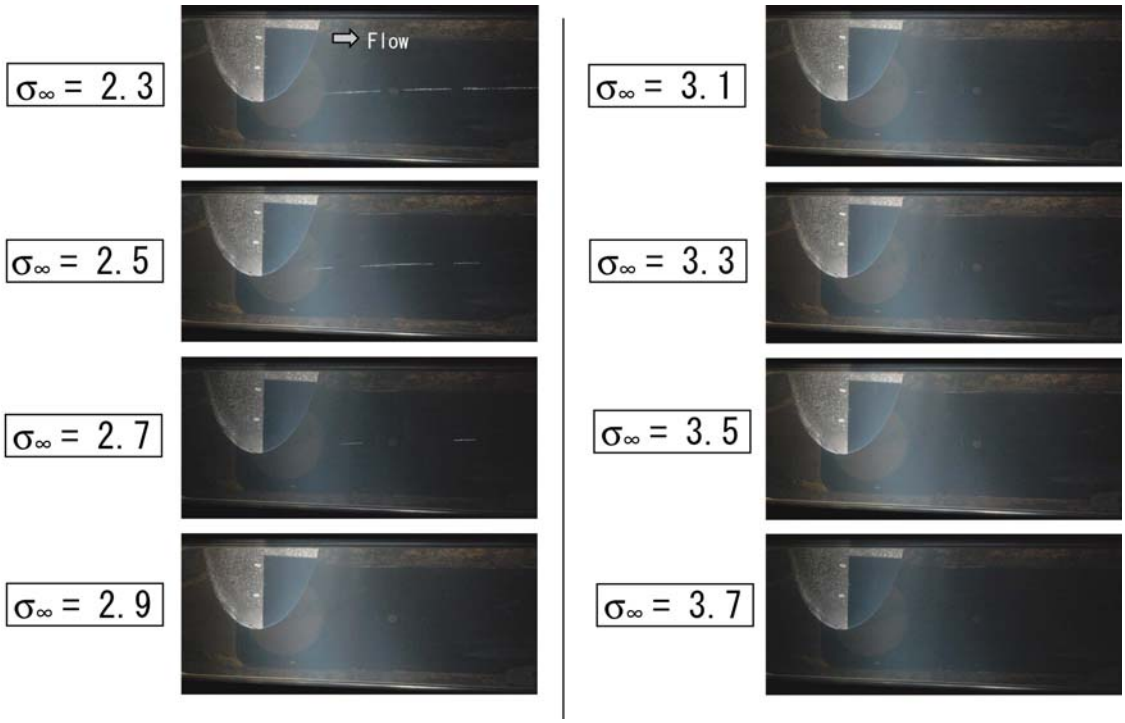

Figure 5-2: Cavitation Appearance with polymer injection
(U_{inf}=8m/s α=8deg C=125wppm, Q_{jet}=5.6cc/s)

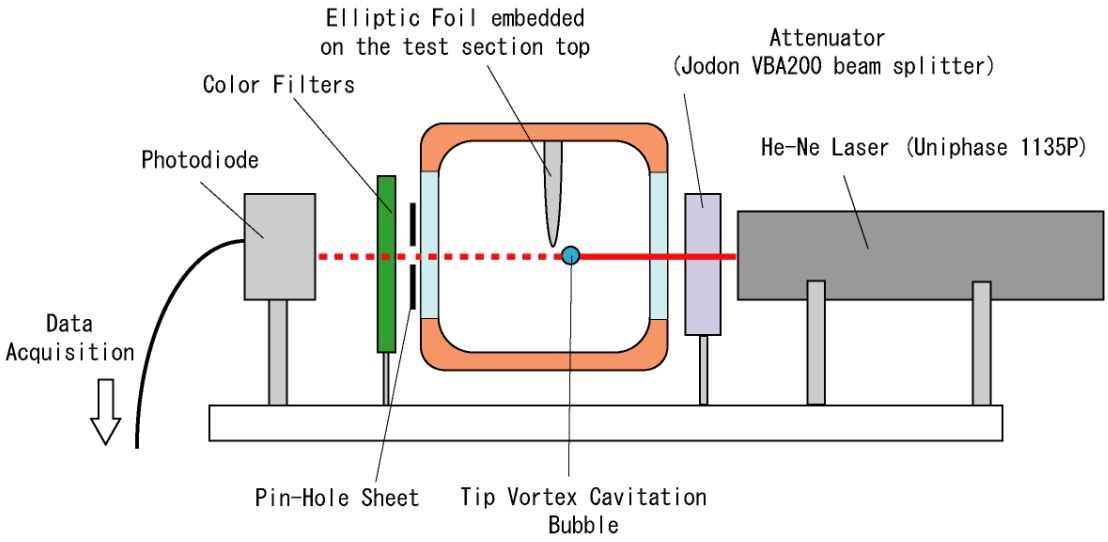

Figure 5-3: Set-up of laser bubble detector

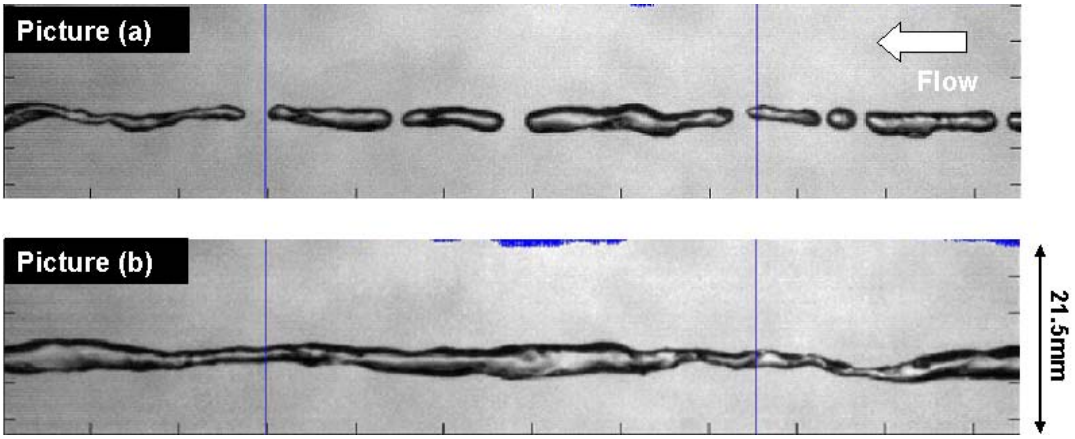

Figure 5-4: TVC bubble image taken by high-speed video camera

Picture (a) and (b) is taken at the same cavitation number (σ_∞=1.4)

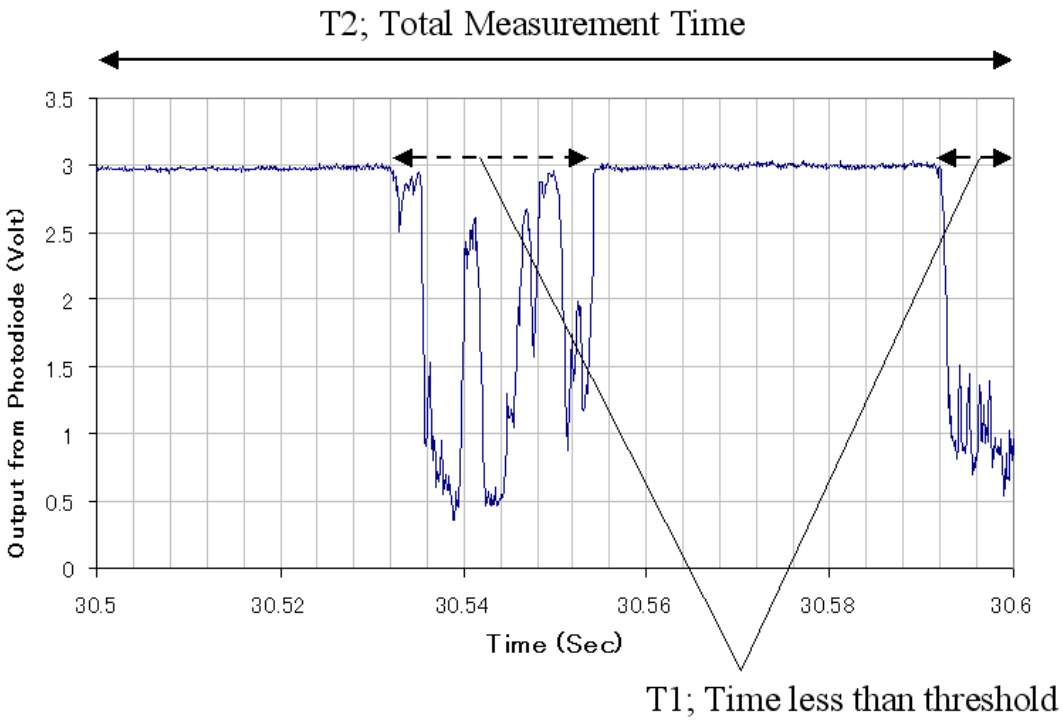

Figure 5-5: Voltage signal from the photodiode and the definition of T1/T2

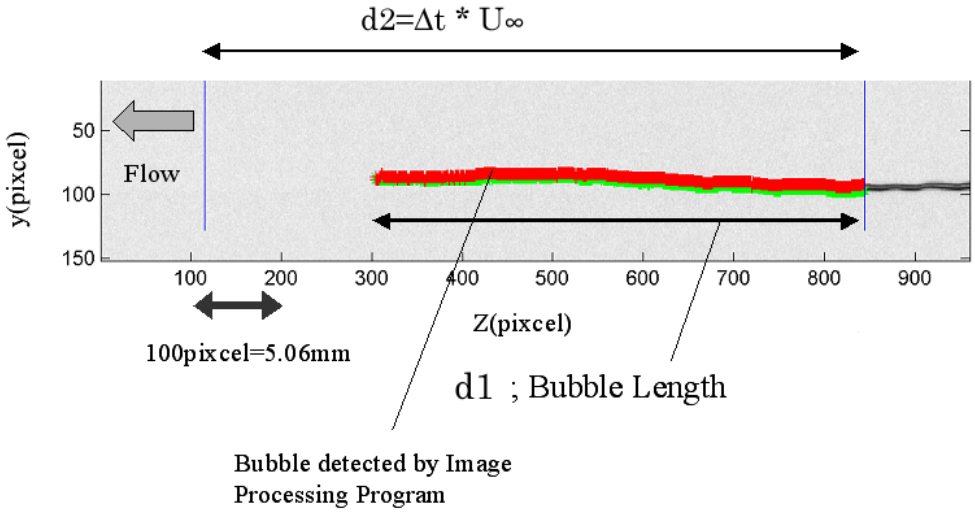

Figure 5-6: High-speed video image and the definition of d1 and d2

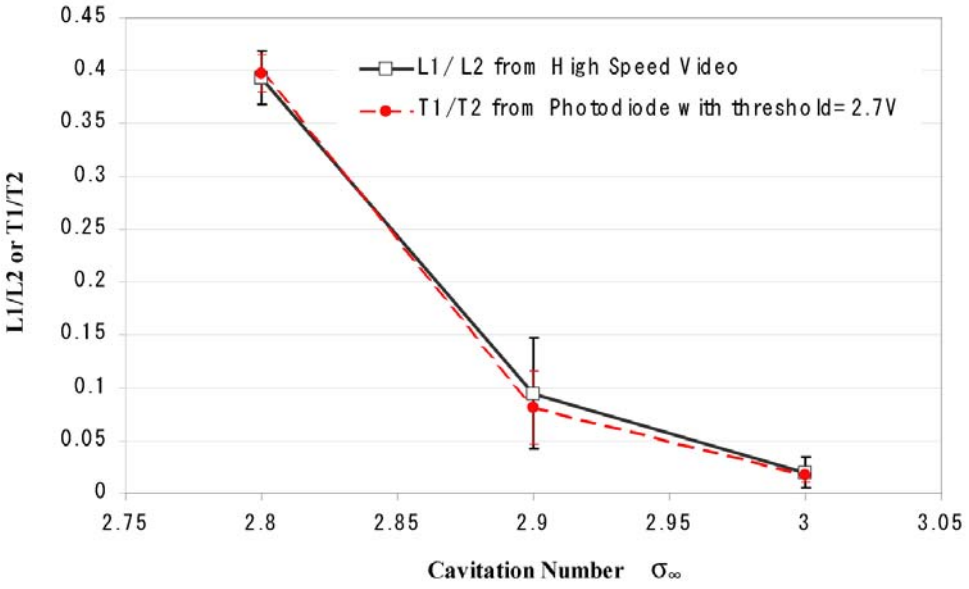

Figure 5-7: Calibration Result

Error bar shows one standard deviation from 10 data sets

Table 5-1: Experiment Conditions for Desinence Test

Injection Flow Rate Q_{jet} (cc/s)	Concentration C (wppm)				
	Water	10	31	125	500
43.2	○				
22.6		○	○	○	○
11.3	○	○	○	○	○
5.6		○	○	○	○
2.8	○	○	○	○	○

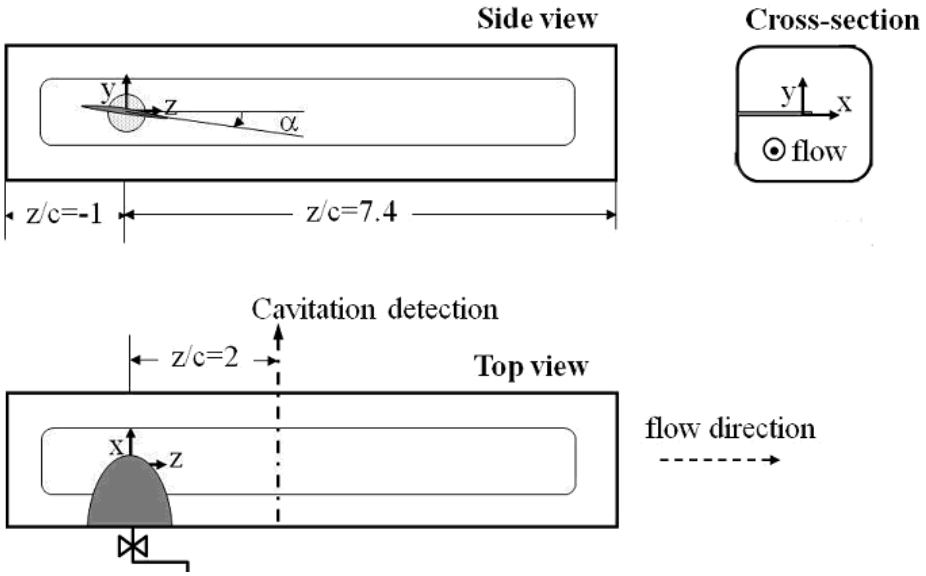

Figure 5-8: Cavitation Desinence Test Set-up

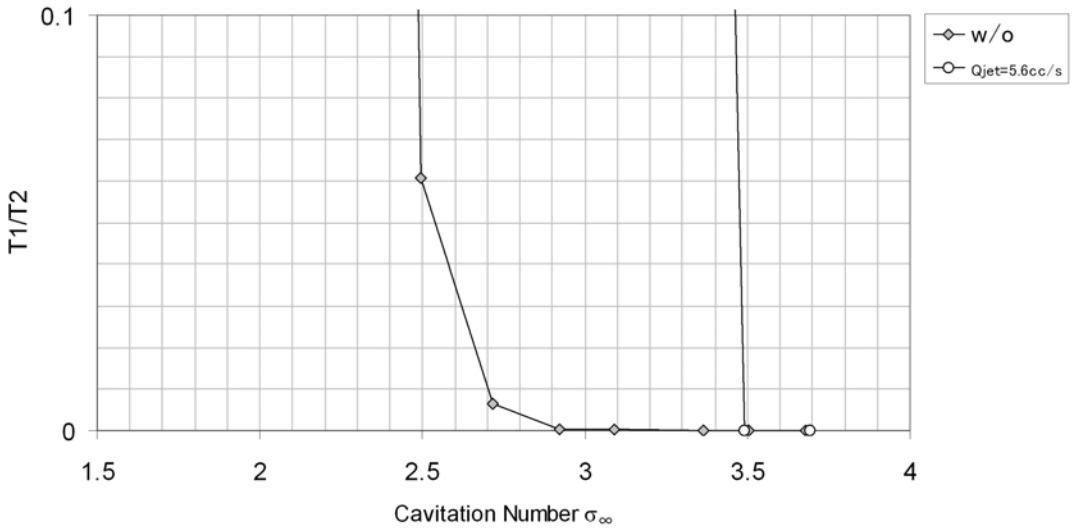

Figure 5-9: T1/T2 plot corresponding Still Picture Observation in Figure 5-1 and Figure 5-2

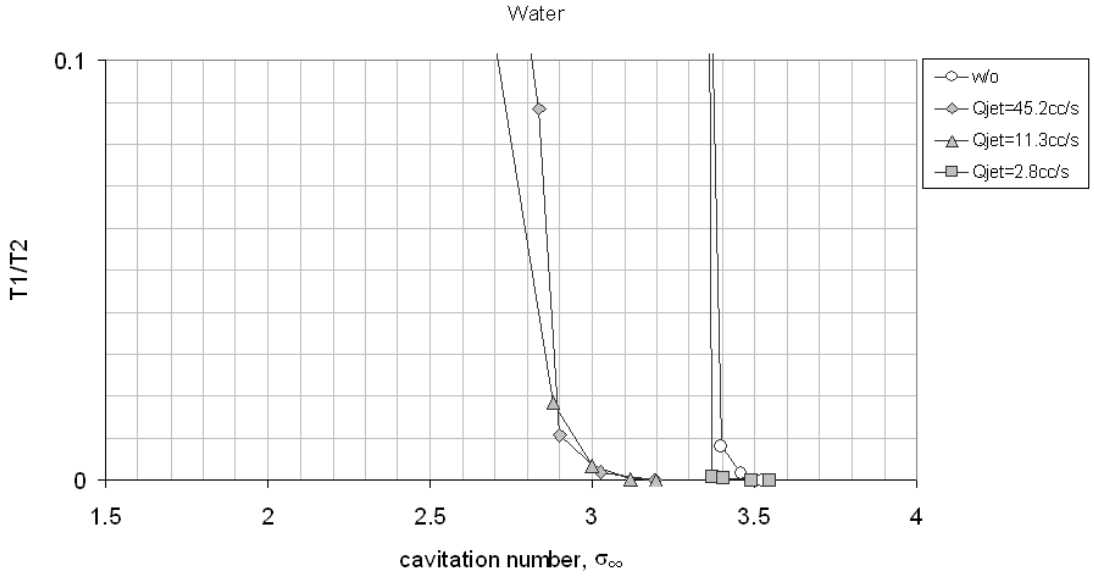

Figure 5-10: T1/T2 plot at water injection (U_{inf}=8m/s α=8deg)

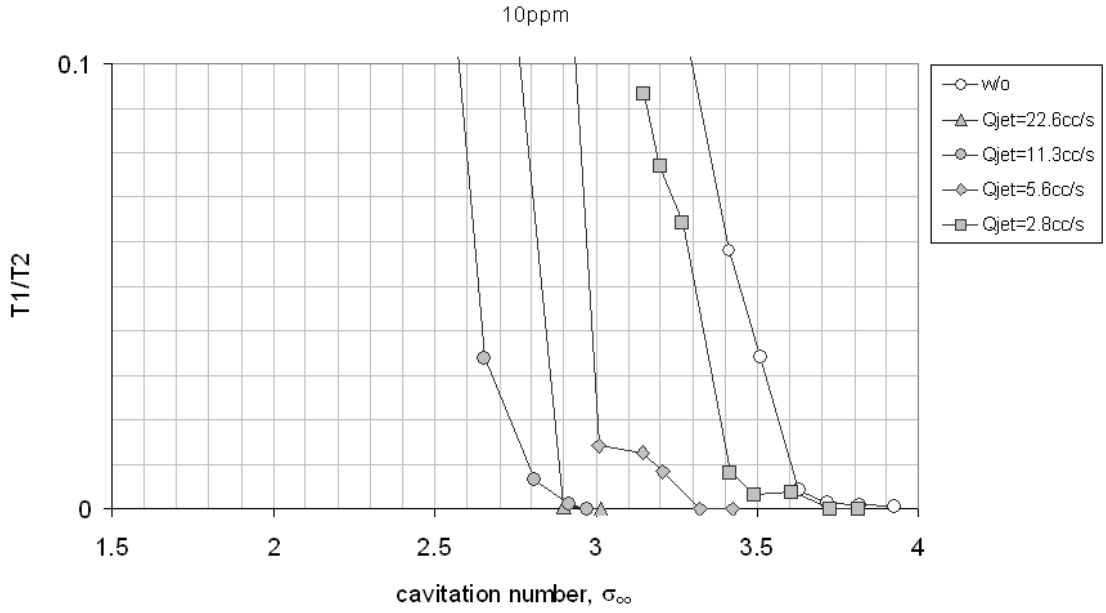

Figure 5-11: T1/T2 plot at C=10wppm (U_{inf}=8m/s α=8deg)

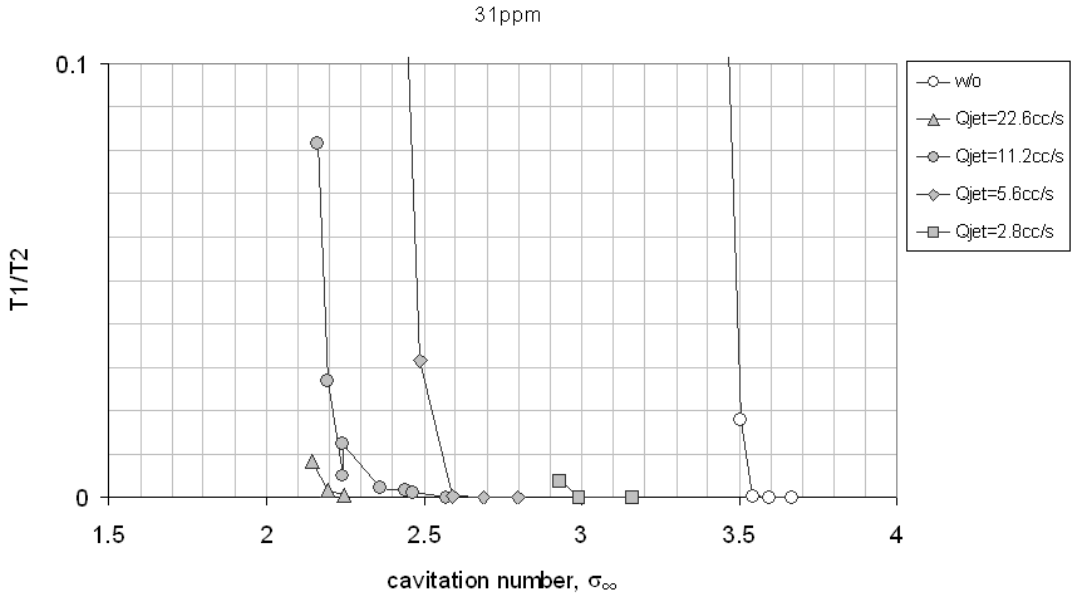

Figure 5-12: T1/T2 plot at C=31wppm (U_{inf}=8m/s α=8deg)

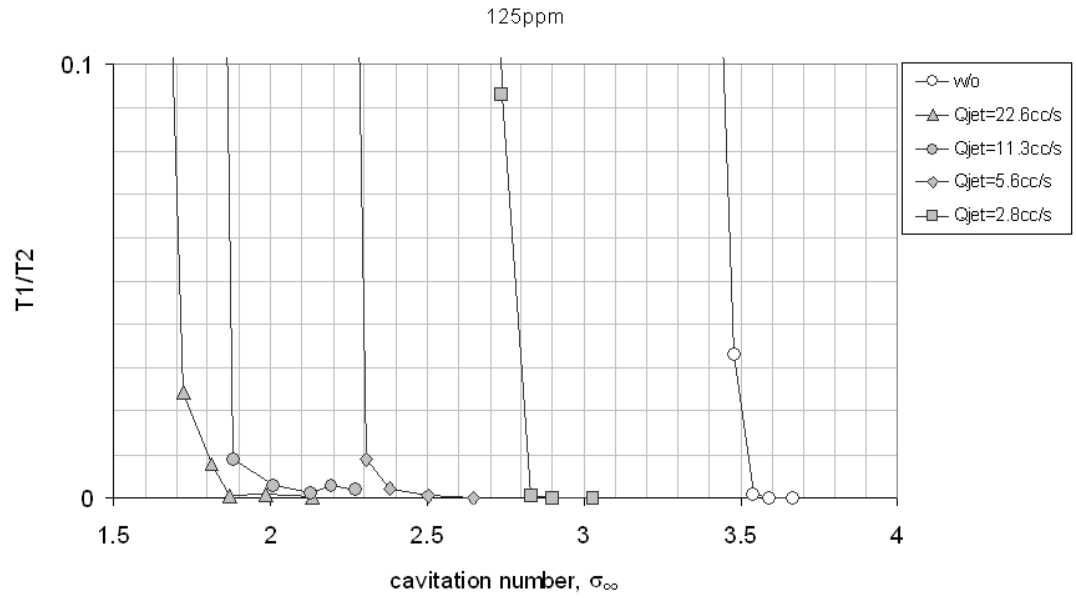

Figure 5-13: T1/T2 plot at C=125wppm (U_{inf}=8m/s α=8deg)

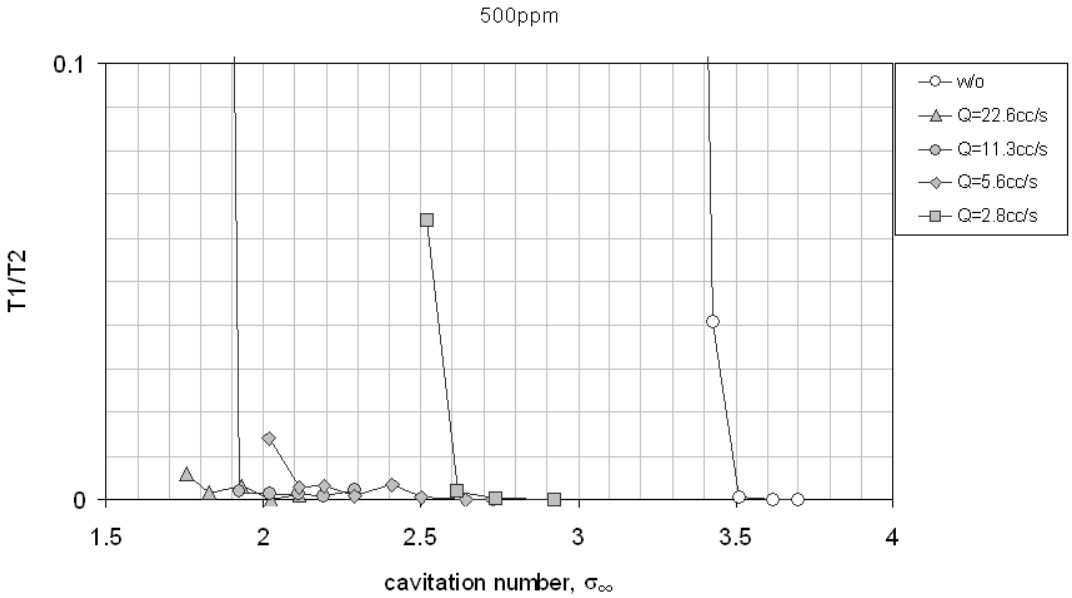

Figure 5-14: T1/T2 plot at C=500wppm (U_{inf}=8m/s α=8deg)

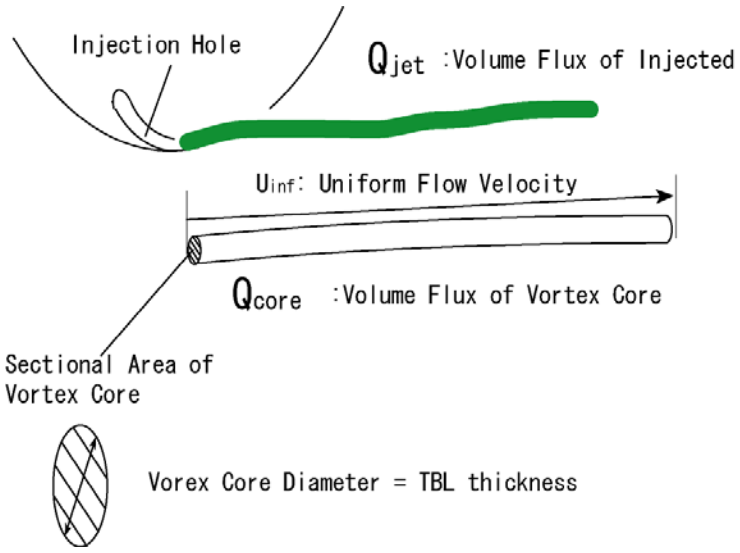

Figure 5-15: The definition of Q_{jet} and Q_{core}

Table 5-2: The estimated value of Q_{core} and Q_{jet} value for the past studies

	Maximum Chord Length C_{max} (m)	Flow Velocity U_{inf} (m/s)	Reynolds Number Re	TBL Thickness δ (m)	Vortex Core FluxRate Q_{core} (m/s)	Injection Flow Rate Q_{jet} (m/s)
Fruman	8.00E-02	12.5	1.00E+06	1.87E-03	3.42E-05	3.40E-06
						4.70E-06
Chahine	9.30E-02	10.6	9.90E+05	2.18E-03	3.96E-05	5.56E-07
						2.22E-06
Souders & Platzer	3.05E-01	13.1	4.00E+06	5.40E-03	3.00E-04	1.90E-05
						1.51E-04
This Study	1.14E-01	8.0	9.14E+05	2.72E-03	4.64E-05	1.41E-06
						2.26E-05

Table 5-3: Injection conditions of this study in comparison with past studies

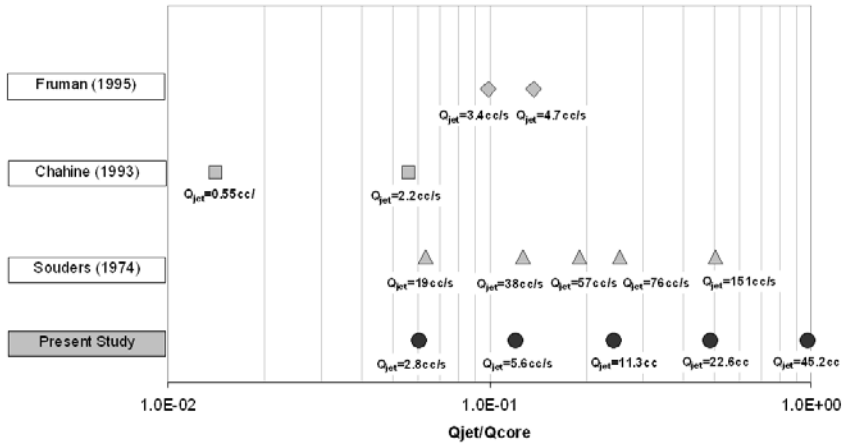

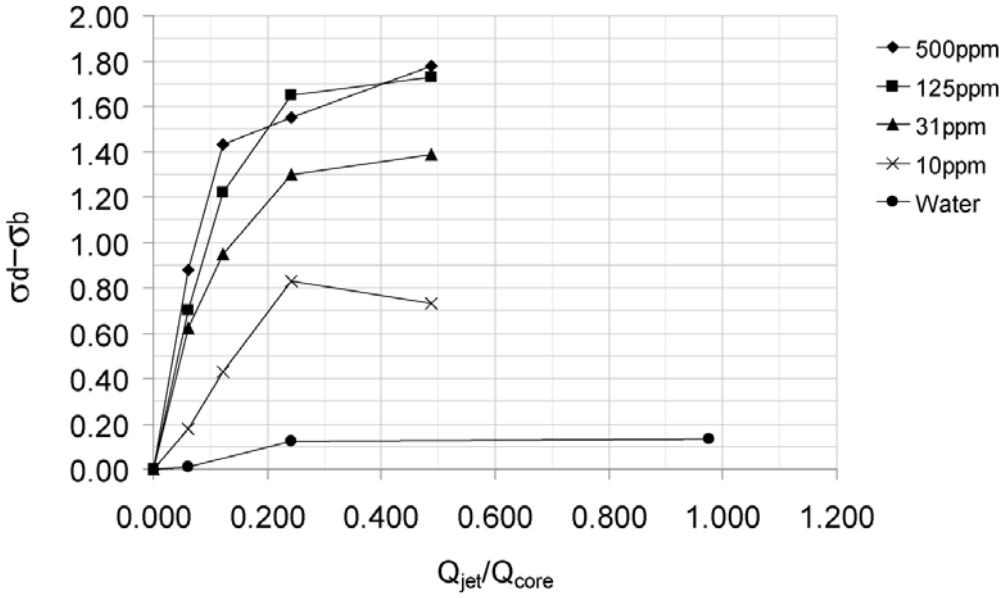

Figure 5-16: TVC suppression effect versus injection flow rates

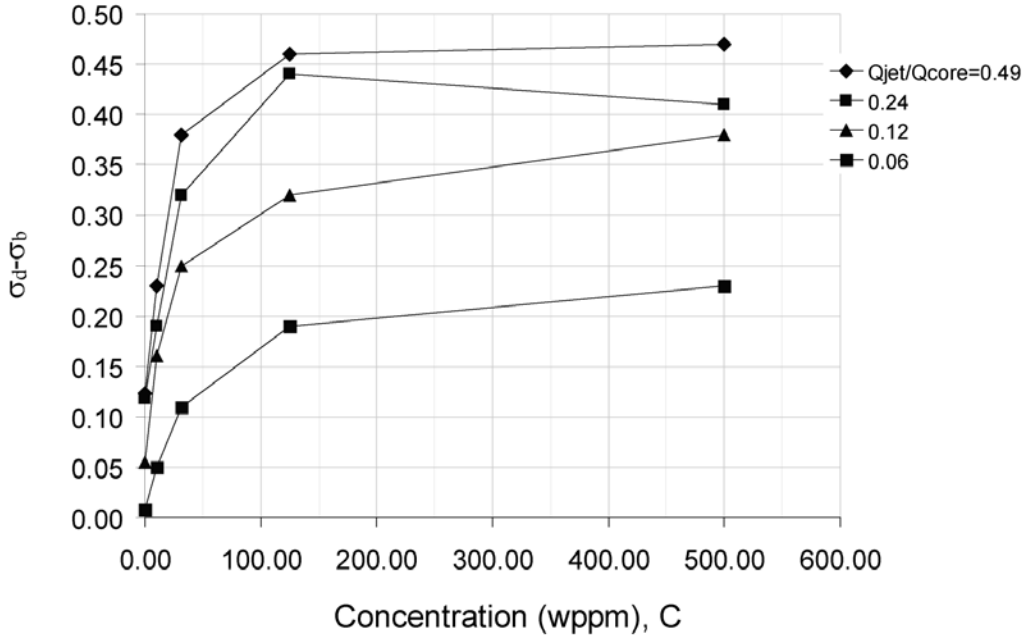

Figure 5-17: TVC suppression effect versus polymer concentration

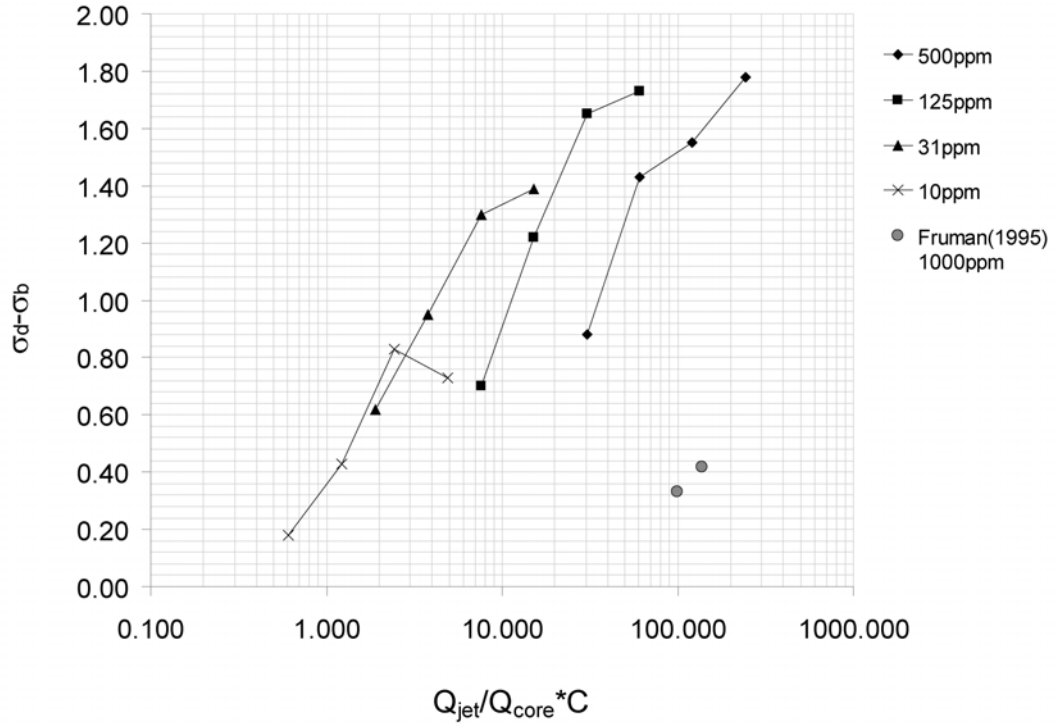

Figure 5-18: TVC suppression effect versus polymer concentration in vortex tube

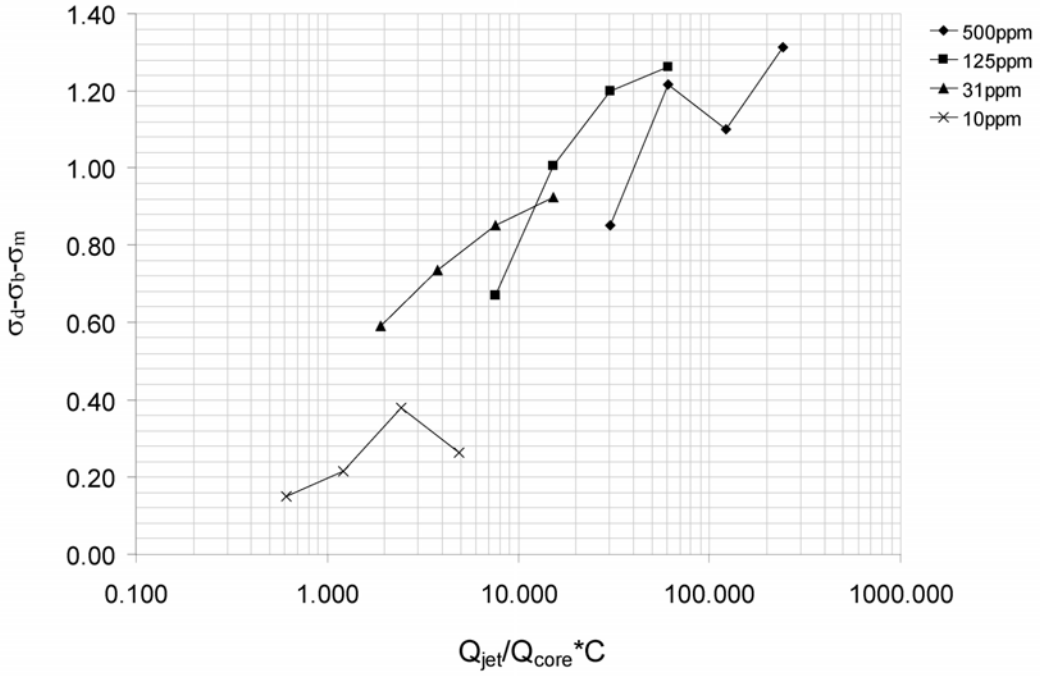

Figure 5-19: TVC suppression effect taking account of mass injection effect

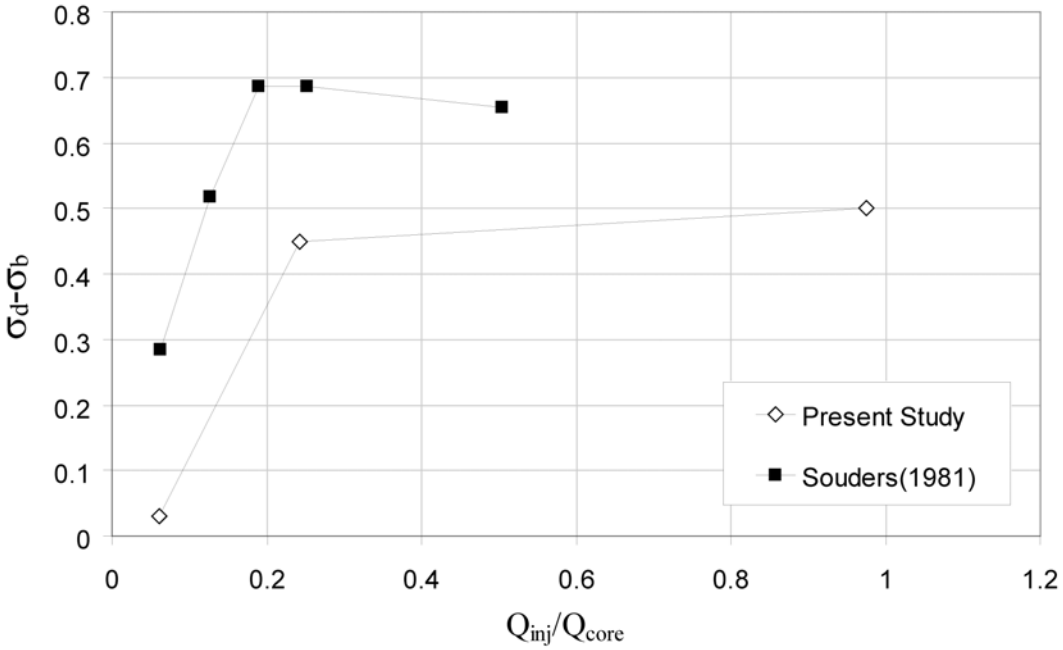

Figure 5-20: Water injection effect in comparison with Sounders(1981)

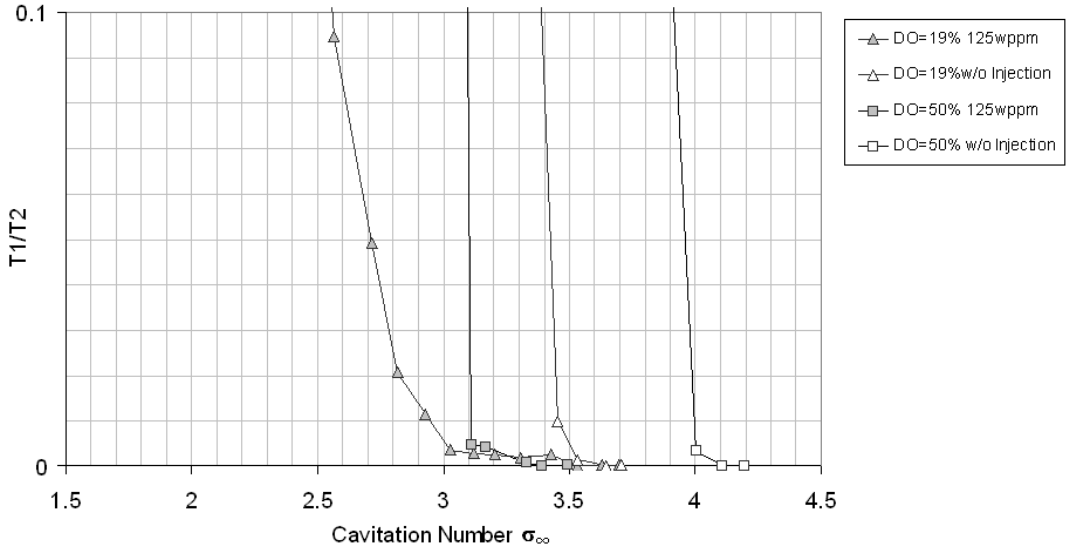

Figure 5-21: Dependence on nuclei distribution in tunnel water

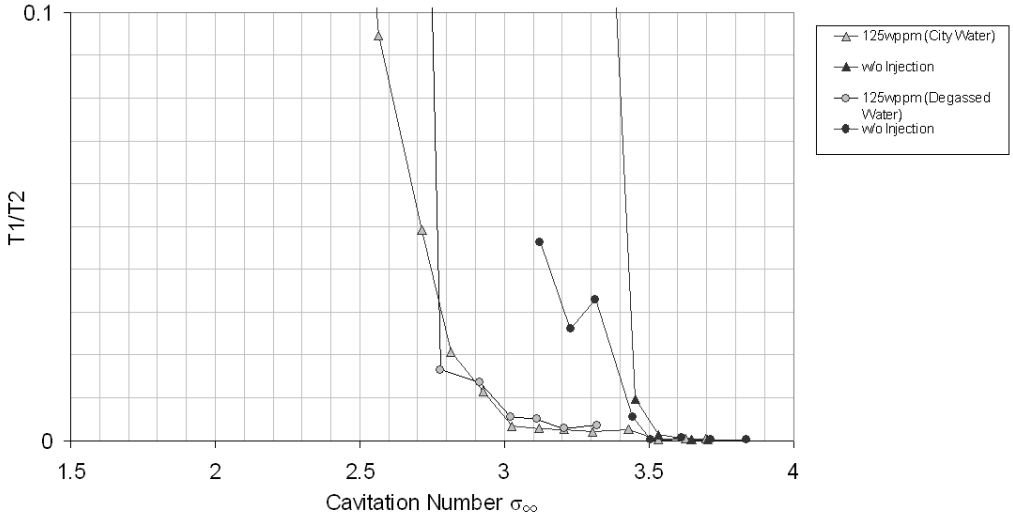

Figure 5-22: Dependence on nuclei in aqueous polymer solution

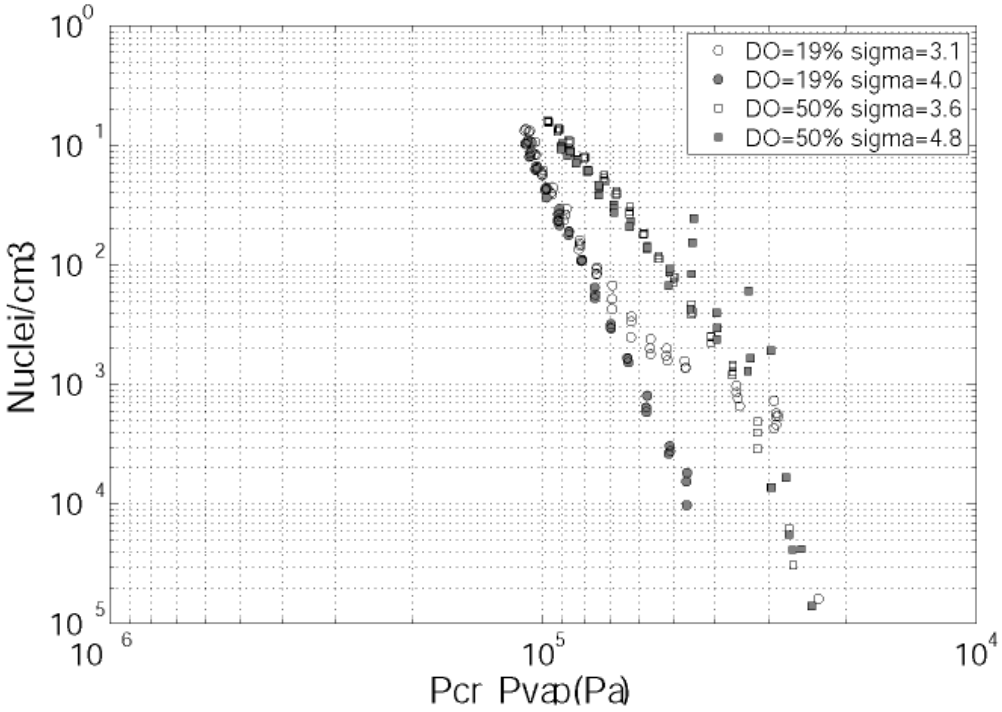

Figure 5-23: Nuclei measurement result corresponding to desinence test

References

23rd ITTC, 2002*, "The Specialist Committee on Water Quality and Cavitation"*, Proceedings of 23rd International Towing Tank Conference, Vol.2, pp459-491

Chahine, G.L., Fruman, D.H., 1979*, "Dilute Polymer Solution Effects on Bubble Growth and Collapse",* Physics of Fluid, Vol. 22, pp. 1406-1407

Chesnakas, C.J., Jessup, S.D., 1998, "Cavitation and 3-D LDV tip-flow field measurements of propeller 5168", NSWCCD Technical Report

Chapter Six

Flow field measurement by stereo particle image velocimetry

To approach the underlying physics of TVC suppression by polymer injection, a series of flow field measurement was carried out using stereo particle image velocimetry (SPIV). A previous study by Fruman (1995) carried out flow field measurements by Laser Doppler Velocimetry (LDV), but the data obtained in the study were limited due to the LDV's long data acquisition time. Studies of this nature require that the background concentration in the tunnel water be kept to less than 10 wppm in order to avoid changes in lift. Therefore, a quick measurement technology is strongly desired. In this decade, SPIV has become a practical measurement method and it has been applied for vortex cavitation studies (Choi (2006), Oweis et al. (2006)).

In this study, SPIV was applied for flow field measurements of the trailing vortex with polymer/water injection at different concentrations and different injection volume rates. Based on the SPIV measurement, the static pressure in the vortex center was estimated by integrating the momentum equation.

6.1 Experiment Set up

Similar to the cavitation desinence test, a hydrofoil was mounted on the top window in the tunnel test section. Two cameras were located on the both side of the test section window viewing through glass prisms embedded on the tunnel window to suppress image distortions (see Figure 6-1). A transverse laser sheet with a thickness of 6~7mm was made by a couple of cylindrical lenses from the bottom of the test section

(see Figure 6-2). Two double pulse Nd:YAG laser (Spectra Physics model Pro-250 series) were used as a laser sources and the laser beams were delivered by a sequence of optical mirrors. The double pulse laser was flashed with a time difference, Δt, of 25 microseconds. Two CCD cameras (LaVision Flow Master 3) with Nikon 105mm micro lenses were used and Scheimpflug mounts were inserted between a camera body and optical lens. CCD cameras capture 1280 pixel by 1024 pixel rectangular images.

Because of the convenience of keeping a whole optics set-up, a special top window to attach a hydrofoil was manufactured. The window allows the user to put a hydrofoil at three different stream-wise locations in the test section (see Figure 6-3).

6.2 Image processing

Using the set up explained in Chapter 6.1, 33.7mm by 25.1mm size rectangular images were obtained. The original particle images are shown in Figure 6-4. As shown in Figure 6-3, the laser sheet hits the foil for the measurements at z/c=25%. The original image contains the reflection from the hydrofoil. The images were post-processed by LaVision Davis version 7.2 software. The multi interrogation (128 pixel to 16 pixel) window size with 50% overlapping was used for the velocity vector fields' calculation. As a result, 173 by 129 vectors with 0.196mm grid spacing were obtained. The post-processed velocity fields from the instantaneous images are shown in Figure 6-5 and Figure 6-6.

6.3 TVC trajectory

TVC trajectory was traced before the SPIV measurement. The measurement was based on the still images taken from the test section side. The trajectories were measured in three different attack angles (α= 4, 6, 8 deg) and two different flow velocities (U_{inf}=8, 12 m/s), and there was no significant difference on the TVC trajectories in different conditions (see Figure 6-7).

In classical wing theory, a tip vortex trajectory has to be dependent on a flow velocity and an attack angle (or hydrofoil lift), because the tip vortex roll-up process should be changed by those conditions. However the experimental data on TVC trajectories were insensitive to those conditions. This insensitivity was also observed in

Arndt et al (1991)'s study, although their numerical simulation shows the trajectory is different for different attack angles.

6.4 Measurement bias and uncertainty

In the following measurements, the average velocity field is obtained from 500 image averaging. Figure 6-8 shows the typical vortex properties from four different numbers of averaged frames (the post-processing procedure will be explained later). From the viewpoint of keeping the background polymer concentration in the tunnel water under an acceptable level, the shortest measurement time was desired. Therefore the averaging number of 500 images was chosen for this study.

To evaluate the measurement bias, the velocity field with empty tunnel was measured and was compared with 2-D PIV results, in which the laser sheet was aligned to the stream direction. Finally the axial component has an error of 2% from 2-D velocity measurement.

6.3 Flow field measurement result

Table 6-1 shows a table with the experimental conditions for the SPIV measurement. Measurements were done at different concentrations and different injection flow rates. Figure 6-9 gives an idea on the geometry of this flow field measurement. Since the vortex path is not parallel to the flow direction, the vortex core location moves up at downstream.

6.3.1 General Observation

Figure 6-10 shows the whole axial velocity contour from 500 image averaging. At the right side top, we can see the low velocity region and this may be induced by the wake of the hydrofoil and the reflection from the hydrofoil contained in original images. Figure 6-11 to Figure 6-14 shows the close up contours with different injection flow rates. For all cases, the axial velocity distributions are not axi-symmetric around a vortex center. Fruman's (1992) study carried out a large amount of LDV measurement on 3-D elliptic foils and the axial velocity profile in a span-wise direction on a small hydrofoil (span=120mm and chord=80mm) shows the unsymmetrical axial velocity profile just downstream from the tip (z/c=15%), but the profile becomes more symmetric at z/c=25%.

They found that the axial velocity profile is strongly dependent on the size of the foil and this axial velocity profile can be governed by a vortex roll-up process and the mechanism is still unrevealed.

Figure 6-15 to Figure 6-19 shows the tangential velocity profile for different injection rates. The tangential velocity profile is also not symmetric around a vortex center. Fruman's (1992) data shows the similar characteristics, in which the tangential velocity on a suction side is bigger than the velocity on a pressure side.

It is difficult to observe a significant difference in both axial and tangential velocity contours between "without injection condition" and "injection condition". The detailed post-processing was done to capture the vortex properties and the procedure will be explained below.

6.3.2 Vortex core size

For a tangential velocity contour, a vortex center was detected from a vorticity distribution. Then vortex radius was found from a tangential velocity profile along a radial direction.

At the first step of the post-processing, the vortex center was found from a vorticity distribution. Figure 6-20 shows the vorticity contour obtained from the vector field in Figure 6-15. To keep a robustness, the spatial low –pass filter was adopted, in which 2*2 high frequency components are removed from the original 129*173 order spatial Fourier transformed functions. The vortex center was defined at the point with the maximum vorticity value.

The vortex radius was detected from the tangential velocity profile along the different radial directions from A to B in Figure 6-22. The vortex radius is finally obtained by averaging the value from 14 different directions.

In "without injection condition", the vortex radius at z/c=25% was found to be r_c=1.84mm. To compare with Fruman(1998)'s data, the vortex, the vortex radius was non-dimensionalized by the turbulent boundary layer thickness (given in (eq. 5-2)). The ratio between the vortex radius and the turbulent boundary layer thickness is 0.68 in this study and 0.87 for Fruman's case. Therefore, the vortex core obtained in this study is comparable to those presented in the literature.

With polymer injection, the vortex radius is not significantly increased at all measurement cases (see Figure 6-27 and Figure 6-28). This is not consistent to Fruman's (1995) findings.

6.3.3 Circulation distribution

Circulation around a vortex center, Γ is calculated by integrating a vorticity in the following equation.

$$\omega_z \equiv \frac{\partial v_x}{\partial y} - \frac{\partial v_y}{\partial x} \qquad \text{(eq. 6-1)}$$

Due to the viscous effect around a vortex core, the radial circulation increases as the radial distance increases and, finally tends to converge at a certain level (see Figure 6-23). In this study, the flow field from SPIV is affected by a shadow image of the foil at r~8mm. Therefore the vorticity within r<7.5mm was integrated to calculate a circulation, Γ.

The circulation of around a tip vortex was non-dimensionalized by a circulation at a root location, Γ_0. The circulation at the root is estimated numerically. A boundary element method, developed by Yamaguchi (1999), was used. The numerical program was used to calculate the flow around a 2-D foil, in which the vortex sheets are distributed on the camber line of the foil and doublets are distributed on a foil surface. The circulation around a root of foil was calculated to be Γ_0 =0.571.

Figure 6-24 shows a circulation distribution at three different axial locations. This shows that the vorticity gradually increases as location goes downstream from the foil tip. This corresponds to classical wing theory, in which a vortex sheet is rolled up eventually. Here, it should be noted that Γ/Γ_0 value at this study (~0.2) is close to Fruman (1995)'s study and the measured roll-up tendency is similar to Fruman's data with STE foil (Straight trailing edge).

6.4 Static Pressure Estimation and vortex properties

The static pressure at a flow field can be estimated by integrating Euler's equation, as follows:

$$\frac{\partial P}{\partial x} = -\rho\left(v_x \frac{\partial v_x}{\partial x} + v_y \frac{\partial v_x}{\partial y} \right)$$

$$\frac{\partial P}{\partial y} = -\rho\left(v_x \frac{\partial v_y}{\partial x} + v_y \frac{\partial v_y}{\partial y} \right) - \rho g$$

$$\Delta P = \int_{\mathrm{Re}\,ferencePo\,\mathrm{int}}^{VortexCenter} \left(\frac{\partial P}{\partial x} dx + \frac{\partial P}{\partial y} dy \right) \qquad \text{(eq. 6-2)}$$

v_x, v_y ; *Velocity components in x, y direction*

ΔP ; *Static pressure difference between a reference point and vortex core*

Liu et al. (2006) applied this method to obtain a static pressure in a flow field from instantaneous PIV measurement vector fields. In their study, the static pressure at whole flow field was calculated and a special algorithm to save a computational time was implemented. In this study, we just aim to calculate the static pressure only in a vortex core. Therefore, equation was simply integrated on multiple paths that connect the vortex center and the reference location. The reference locations were on the most outward position in a vector flow field measurement (see Figure 6-25).

In this study, the obtained flow field area was limited and the reference location still cannot be treated as a uniform flow location. So the static pressure at the reference was calculated using Bernoulli's equation:

$$P_{ref} = P_{TestSection} + \frac{1}{2}\rho\left(U_{\mathrm{inf}}{}^2 - v_{ref}{}^2 \right) \qquad \text{(eq. 6-3)}$$

$$P_{VortexCenter} = P_{ref} - \Delta P \qquad \text{(eq. 6-4)}$$

$P_{TestSection}, U_{\inf}$; *Static pressure and velocity at test section (Pa), (m/s)*

P_{ref}, v_{ref} ; *Static pressure and velocity at reference location(Pa), (m/s)*

$P_{VortexCenter}$; *Static pressure at vortex center(Pa)*

To know the uncertainty of this procedure, the pressure estimation was carried out along 21 different path, shown in Figure 6-25. Figure 6-26 shows the resulted static pressure obtained from 21 different integration paths. The estimated values from path #1-#10 are smaller than the values form #11-#20. The averaged pressure drop value is 63,469 (Pa) and the standard deviation from 21 paths is 4,494 (Pa). As this pressure estimation neglect the viscous term in the momentum conservation equation, the dependence on the path shown in Figure 6-26 can be introduced by the viscous effect around a core.

To keep robustness, it is better to have a large derivation distance for the direction with large velocity gradient. Therefore path #11 is chosen to calculate the static pressure beyond this part, since the integral path is parallel to the velocity gradient. The static pressure value is non-dimensionalized as a pressure coefficient Cp, which is given by the following equation.

$$Cp = \frac{P_{VortexCenter} - P_{TestSection}}{\frac{1}{2}\rho U_{\inf}^{2}} \qquad \text{(eq. 6-5)}$$

The resulting static pressure and vortex properties are summarized in Figure 6-31 and Figure 6-32. From the figures, it can be noted that the static pressure estimated at the center of the vortex was not sensitive to the injection conditions. Moreover, it remained quite similar to the “non-injection case”. This apparent inconsistency between the expected results from the cavitation desinence test and the estimated C_p value from the SPIV measurements will be discussed in the next chapter.

6.5 Instantaneous static pressure estimation

In the previous chapter, the static pressure in the vortex core as estimated from the time average flow field. In this chapter, the pressure fluctuation in the vortex core from the instantaneous flow field was tried.

Instead of (eq. 6-2), we need to integrate the conservation equation with time derivative terms as follows.

$$\frac{\partial P}{\partial x} = -\rho\left(\frac{\partial v_x}{\partial t} + v_x\frac{\partial v_x}{\partial x} + v_y\frac{\partial v_x}{\partial y}\right)$$

$$\frac{\partial P}{\partial y} = -\rho\left(\frac{\partial v_y}{\partial t} + v_x\frac{\partial v_y}{\partial x} + v_y\frac{\partial v_y}{\partial y}\right) - \rho g \qquad \text{(eq. 6-6)}$$

In the original research by Liu et al. (2006), the four-pulse laser was used to obtain two velocity fields in a short time (Δt between two flow fields is the order of ten micro seconds). This study used a double pulse laser with a frequency of 8Hz and we just obtained 8 flow fields in a second. Therefore, the calculation can underestimate a time derivative term.

Figure 6-33 shows the standard deviation of the estimated pressure for 500wppm polymer injection cases with different injection flow rates. The standard deviation is quite large to the average value and there is no significant difference between “non-injection” case and “polymer injection” case. This post-process failed to capture the pressure difference due to the erroneous instantaneous flow field.

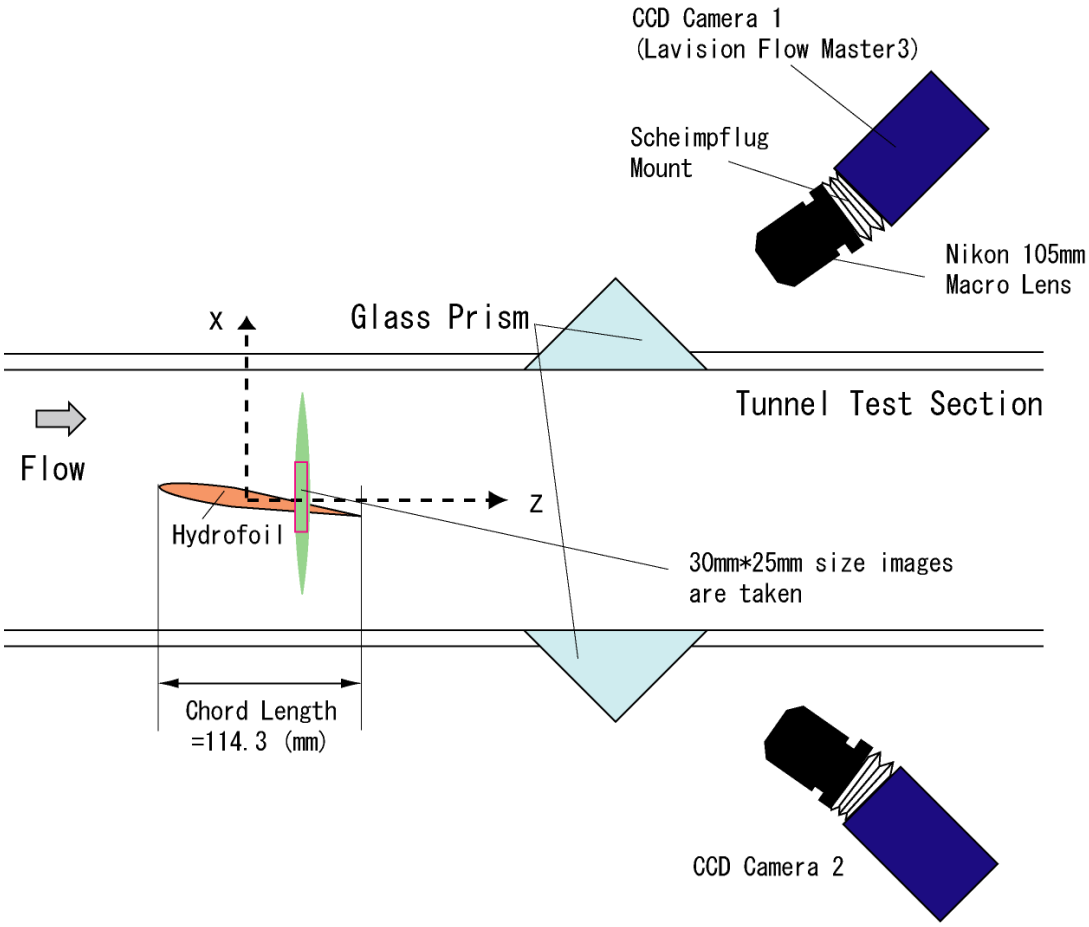

Figure 6-1: Top view of SPIV set up

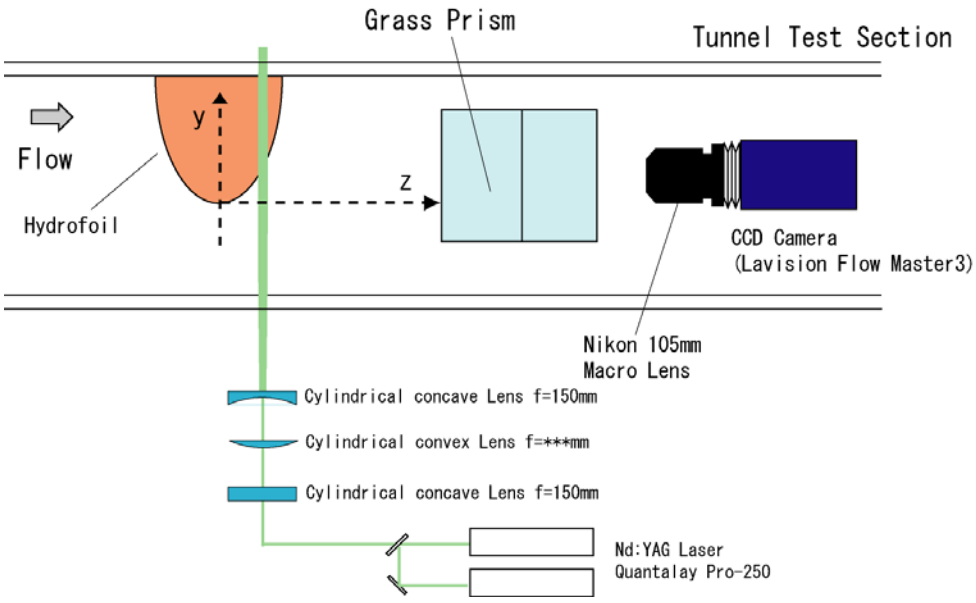

Figure 6-2: Side view of SPIV set up

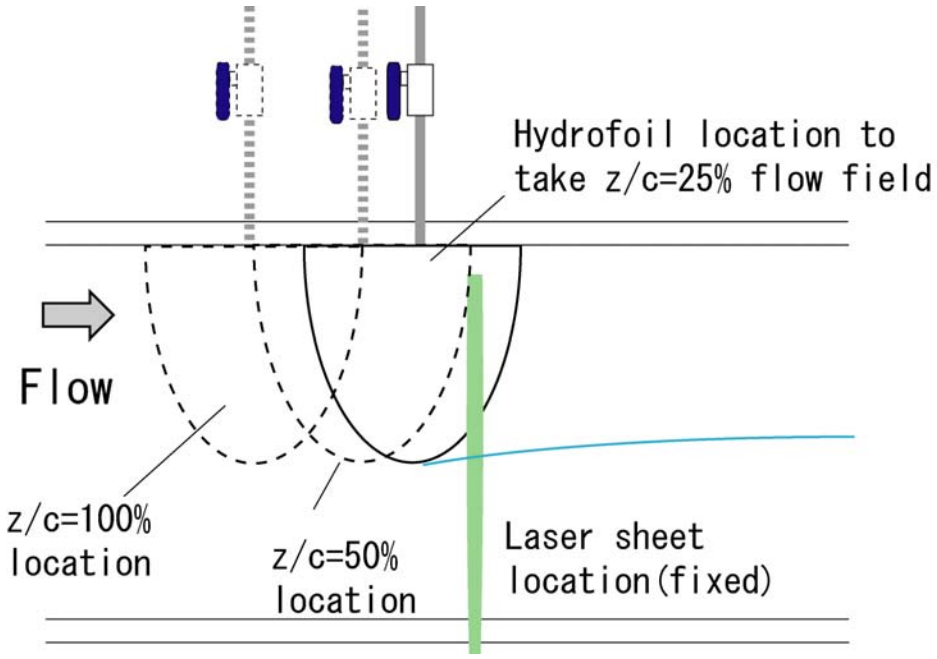

Figure 6-3: Foil mount set up

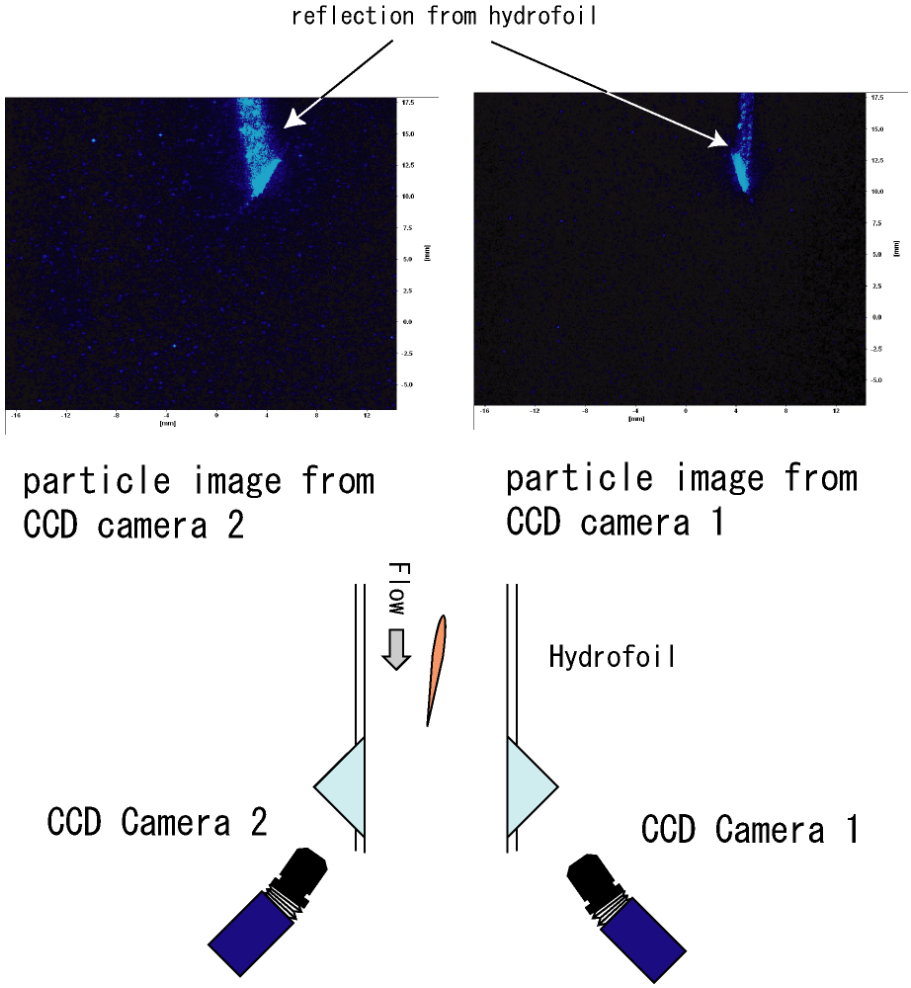

Figure 6-4: Original particle images obtained by CCD cameras

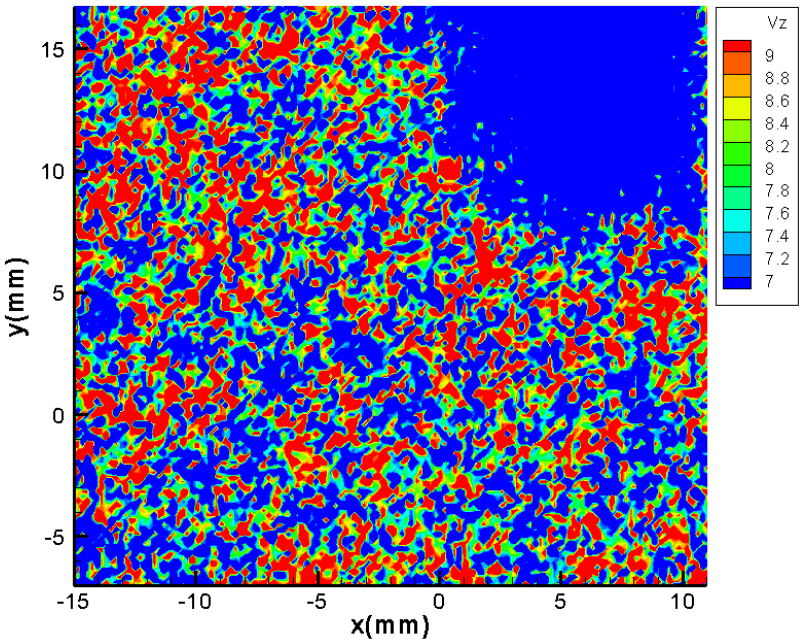

Figure 6-5: Instantaneous axial velocity contour (z/c=25%) in "non-injection case"

(α=8deg, U_{inf}=8m/s, unit in (m/s))

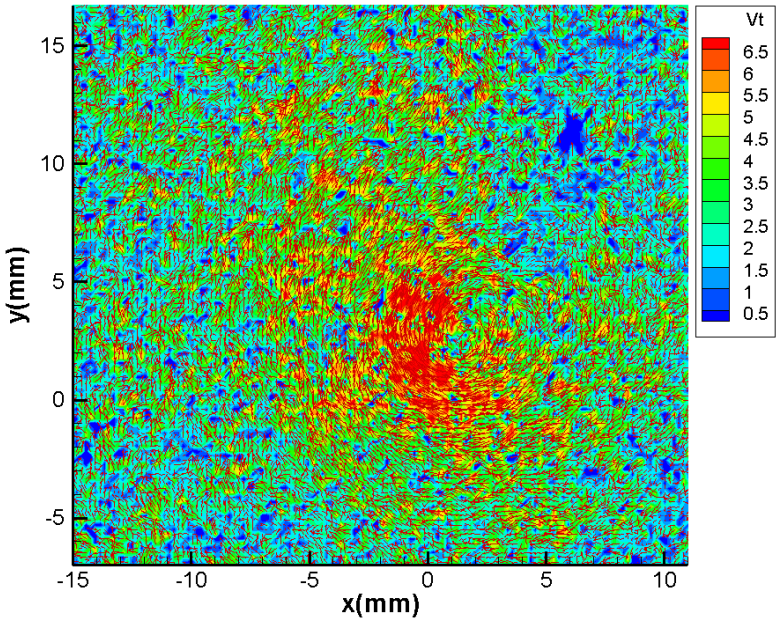

Figure 6-6: Instantaneous tangential velocity contour (z/c=25%) in "non-injection case"

(α=8deg, U_{inf}=8m/s, unit in (m/s))

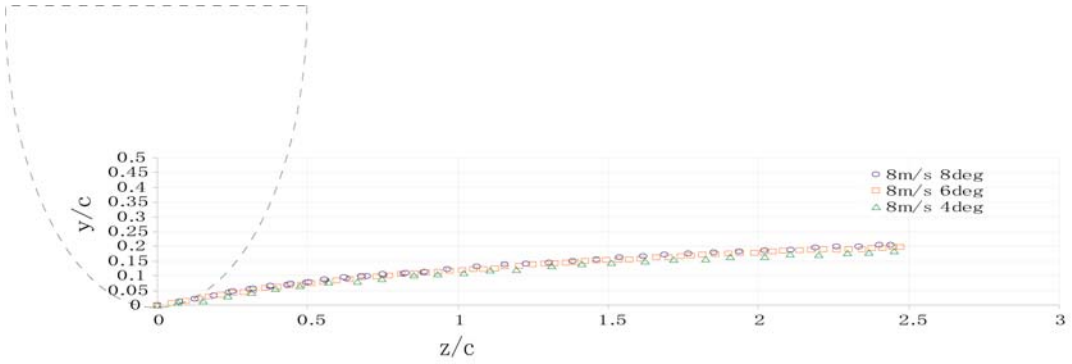

(a) Constant velocity with different attack angles

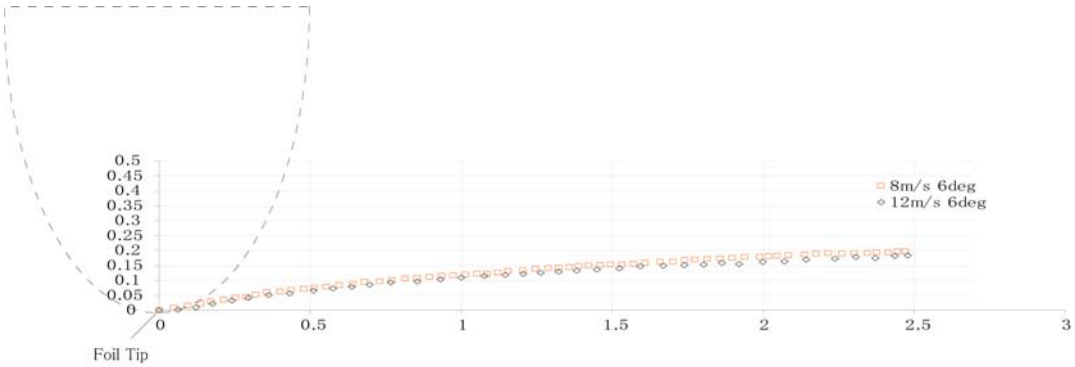

(b) Constant attack angle with different velocities

Figure 6-7: Tip vortex trajectory

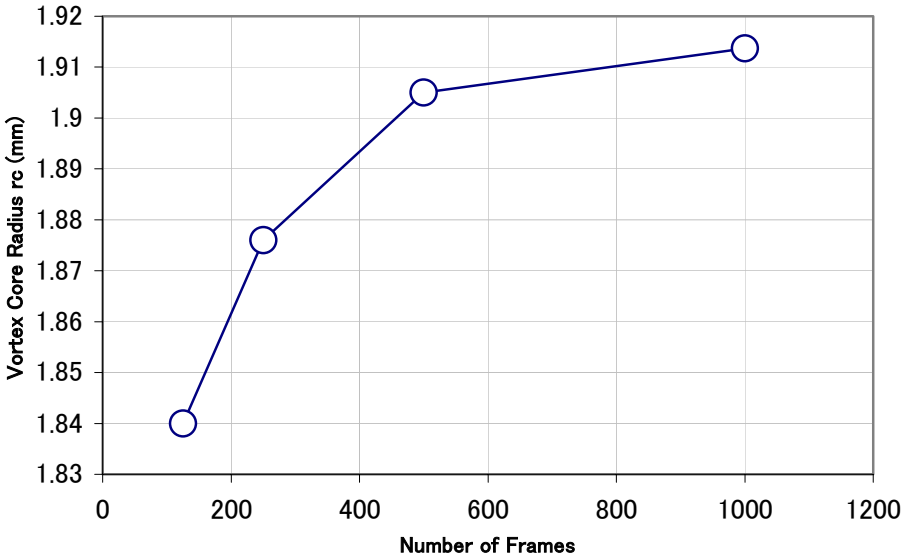

(a) Vortex core radius

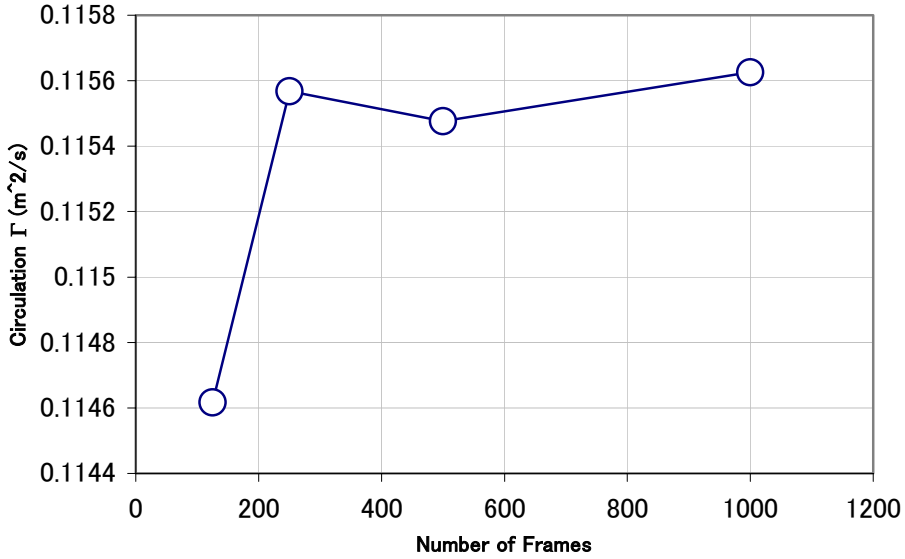

(b) Circulation at z/c=25%

Figure 6-8: Vortex properties at different averaging numbers

(α=8deg, U_{inf}=8m/s, "non-injection case")

Table 6-1: SPIV measurement conditions

(a) Measurement conditions at z/c=25%

	Flow Rate Q_{jet}			
Concentration C	2.8 (cc/s)	5.6 (cc/s)	11.3 (cc/s)	22.6 (cc/s)
Water	○		○	○
31 (wppm)	○	○	○	○
125 (wppm)	○	○	○	○
500 (wppm)	○		○	○

(b) Measurement conditions at z/c=50%

	Flow Rate Q_{jet}			
Concentration C	2.8 (cc/s)	5.6 (cc/s)	11.3 (cc/s)	22.6 (cc/s)
Water	○		○	○
31 (wppm)	○	○	○	○
500 (wppm)	○	○	○	○

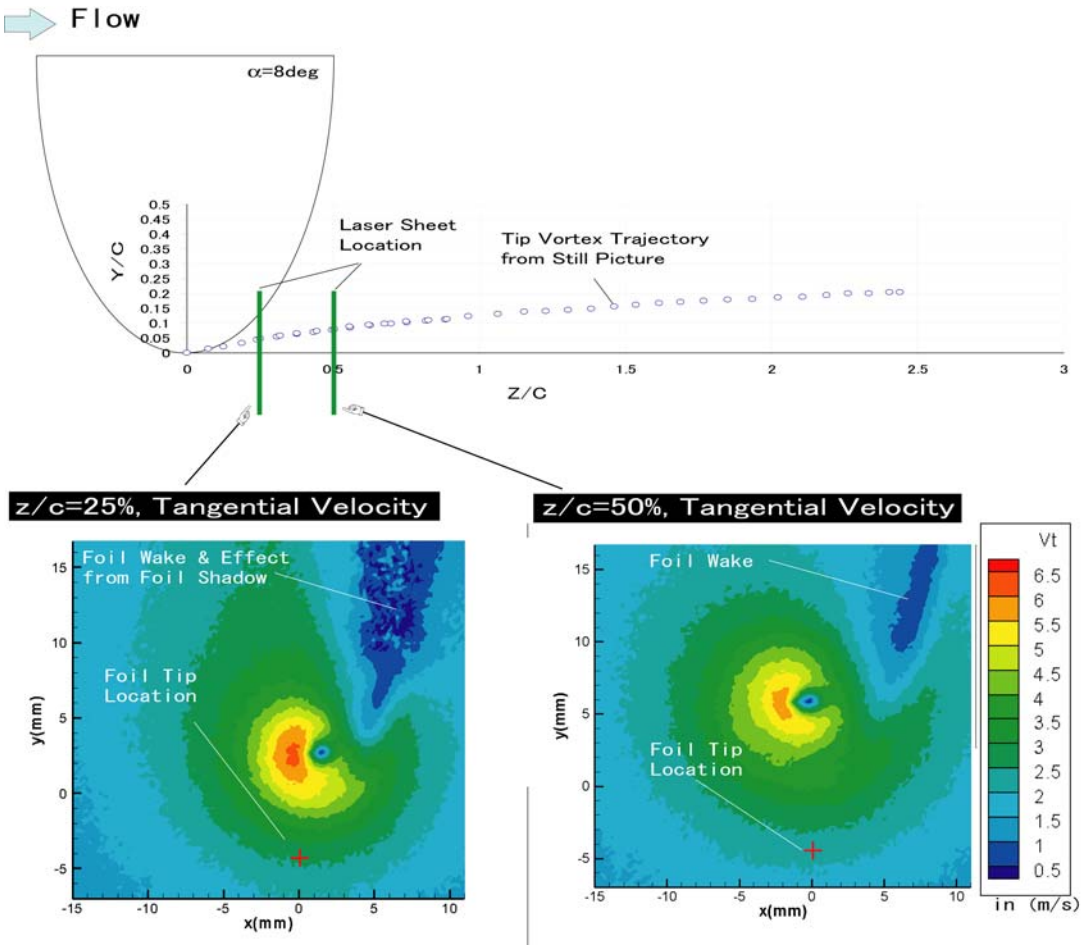

Figure 6-9: Flow field measurement locations and vortex geometry

Tangential velocity contours were obtained at α=8deg, U_{inf}=8m/s in "non-injection case".

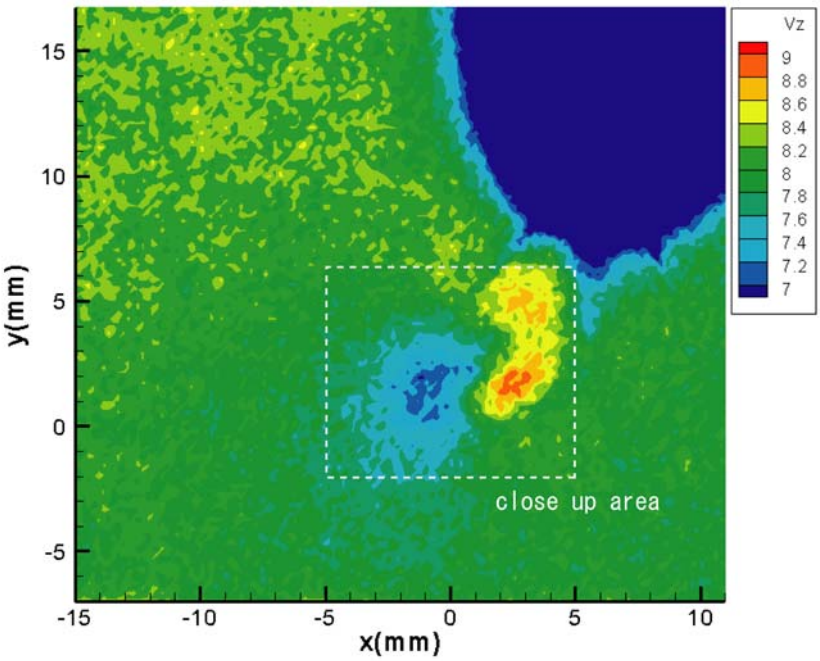

Figure 6-10: Whole axial velocity contour (z/c=25%) in "non-injection case"

(α=8deg, U_{inf}=8m/s, unit in (m/s))

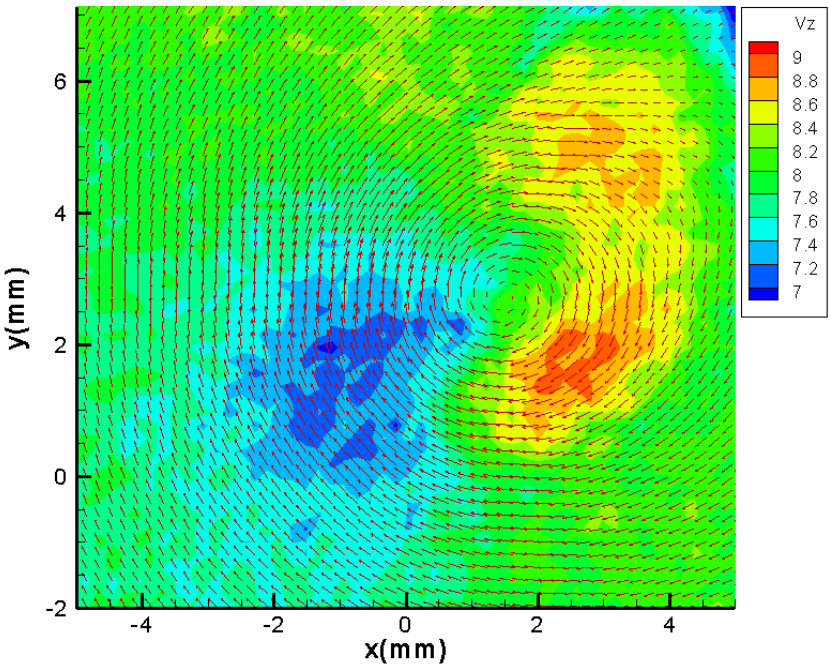

Figure 6-11: Close up axial velocity contour (z/c=25%) in "non-injection case"

(α=8deg, U_{inf}=8m/s, unit in (m/s))

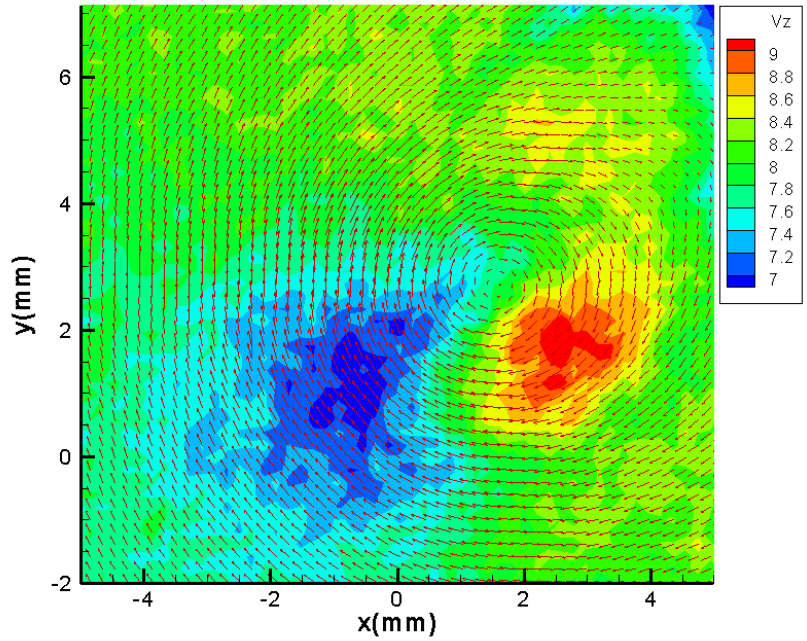

Figure 6-12: Close up axial velocity contour (z/c=25%) with polymer injection (Q_{jet}=2.8(cc/s), C=500 (wppm), α=8deg, U_{inf}=8m/s, unit in (m/s))

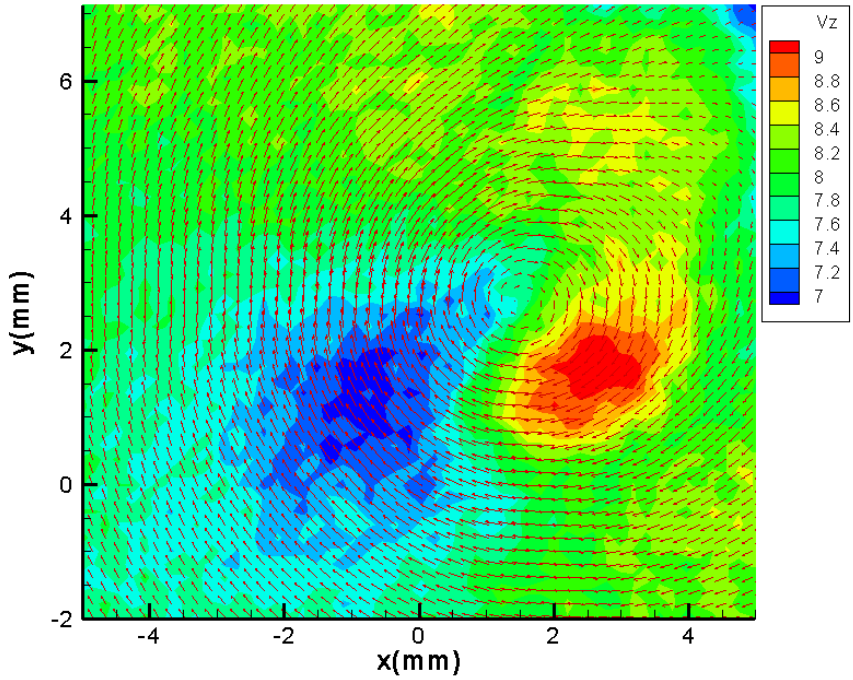

Figure 6-13 :Close up axial velocity contour (z/c=25%) with polymer injection (Q_{jet}=5.6(cc/s), C=500 (wppm), α=8deg, U_{inf}=8m/s, unit in (m/s))

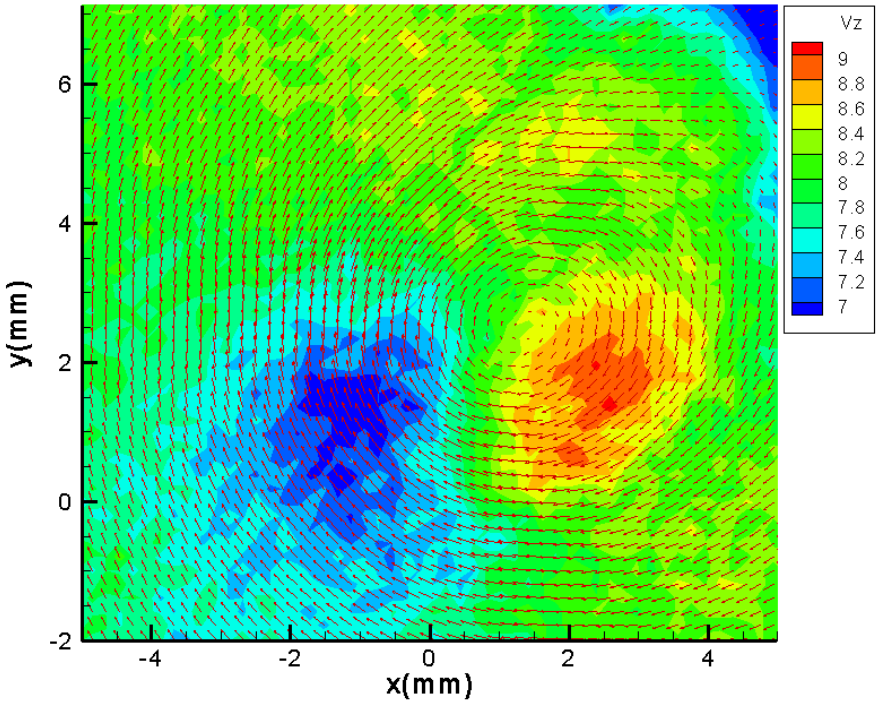

Figure 6-14: Close up axial velocity contour (z/c=25%) with polymer injection (Q_{jet}=22.8(cc/s), C=500 (wppm), α=8deg, U_{inf}=8m/s, unit in (m/s))

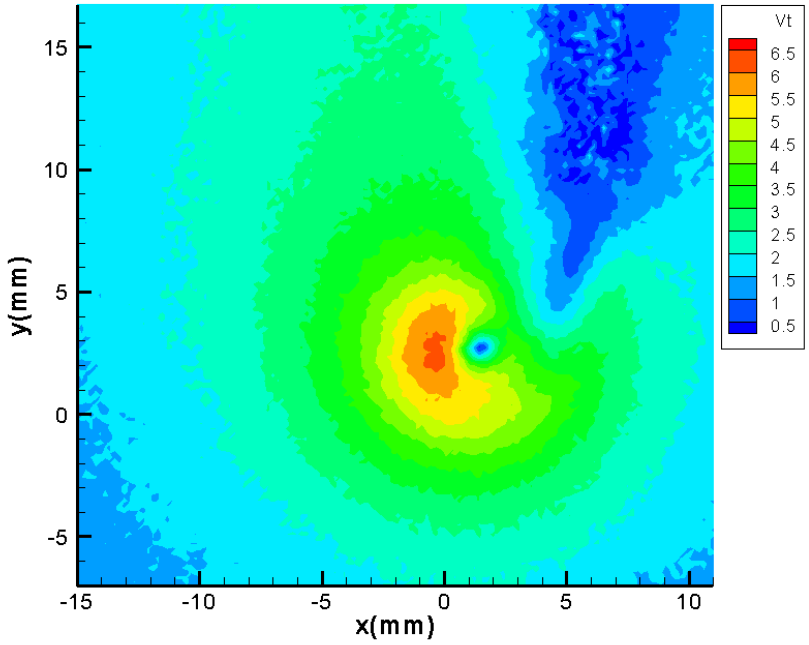

Figure 6-15: Whole tangential velocity contour (z/c=25%) in "non-injection case" (α=8deg, U_{inf}=8m/s, unit in (m/s))

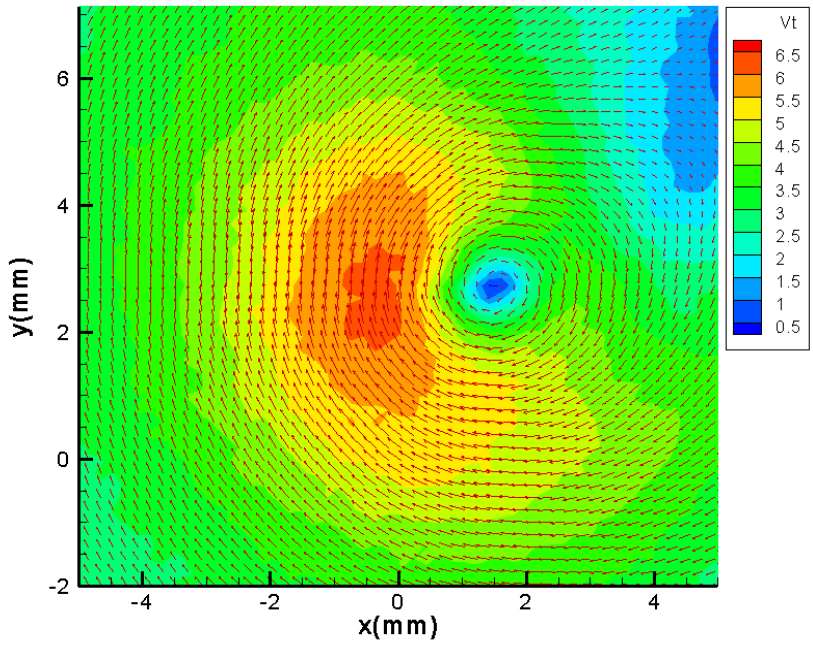

Figure 6-16: Close up tangential velocity contour (z/c=25%) in "non-injection case"
(α=8deg, U_{inf}=8m/s, unit in (m/s))

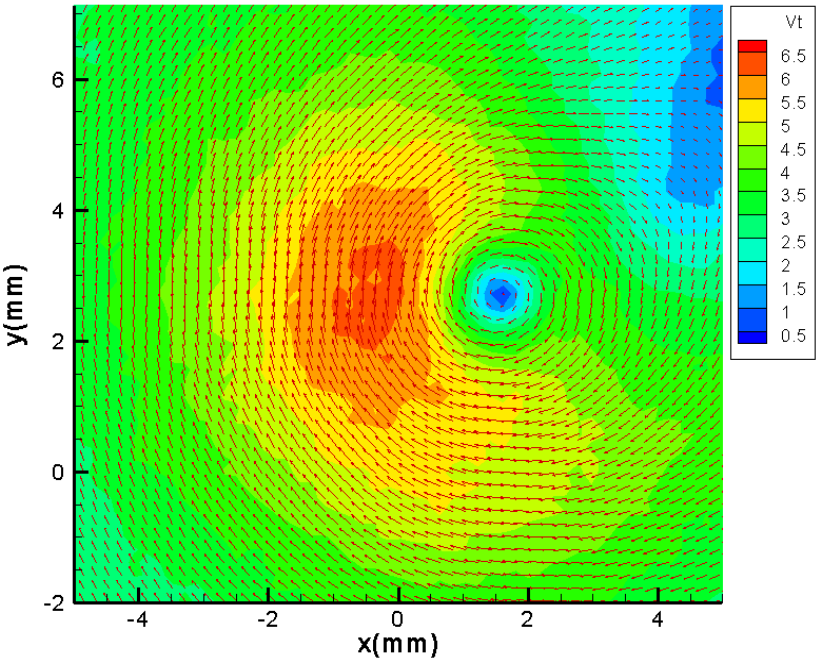

Figure 6-17: Close up tangential velocity contour (z/c=25%) with polymer injection
(Q_{jet}=2.8(cc/s), C=500 (wppm), α=8deg, U_{inf}=8m/s, unit in (m/s))

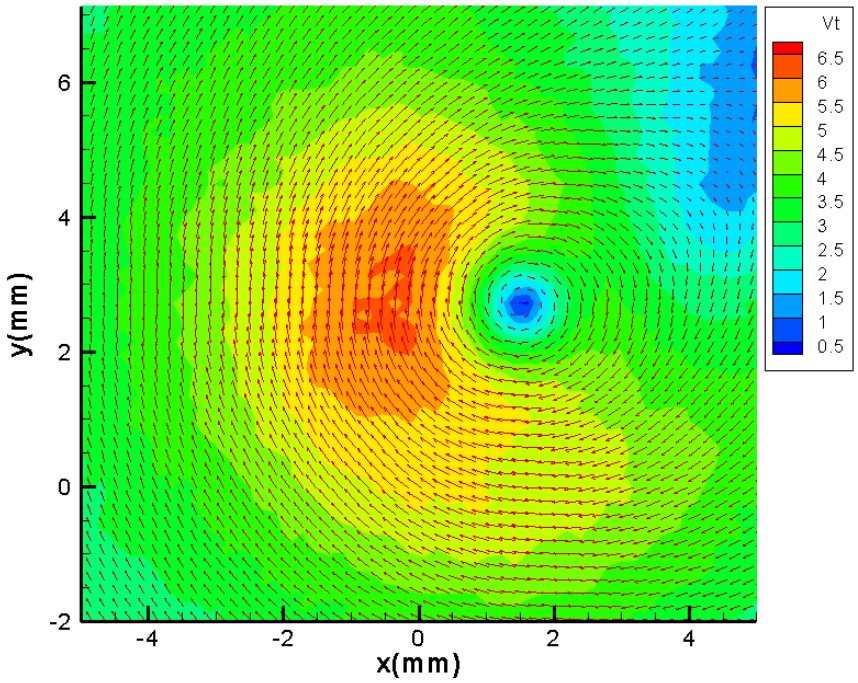

Figure 6-18: Close up tangential velocity contour (z/c=25%) with polymer injection (Q_{jet}=5.6(cc/s), C=500 (wppm), α=8deg, U_{inf}=8m/s, unit in (m/s))

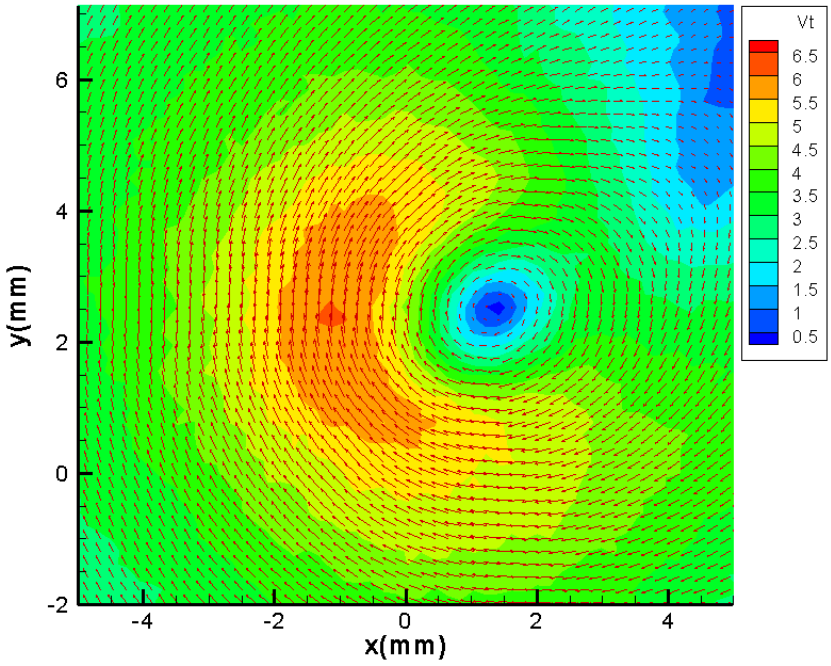

Figure 6-19: Close up tangential velocity contour (z/c=25%) with polymer injection (Q_{jet}=22.6(cc/s), C=500 (wppm), α=8deg, U_{inf}=8m/s, unit in (m/s))

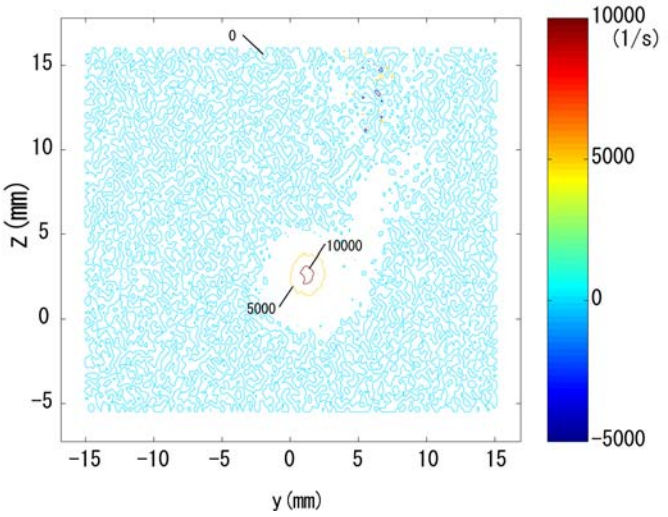

Figure 6-20: Vorticity contour from (z/c=25%) in "non-injection case"

(α=8deg, U_{inf}=8m/s)

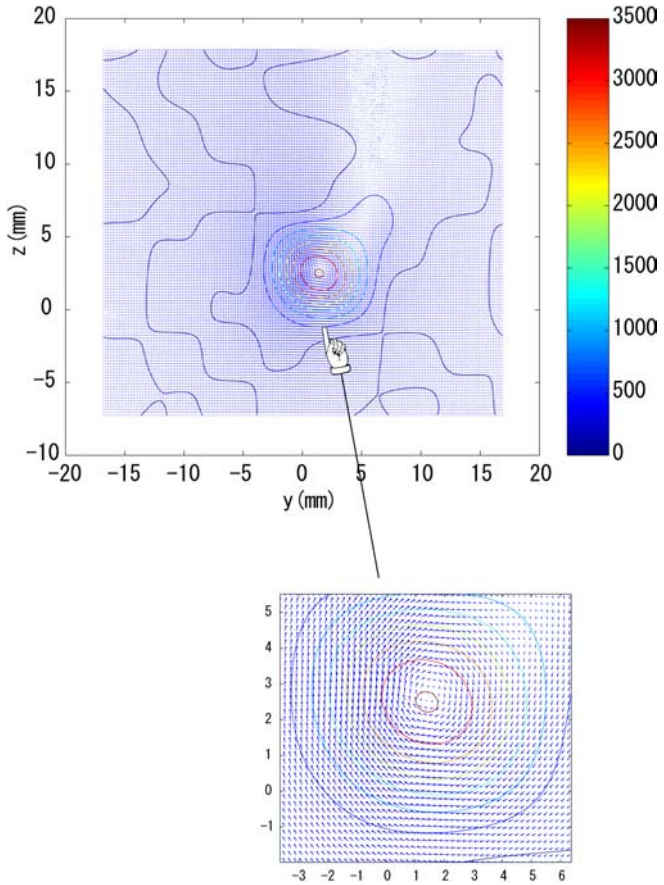

Figure 6-21: Low-pass filtered vorticity contour (to detect the vortex center)and original vector field from Figure 6-20

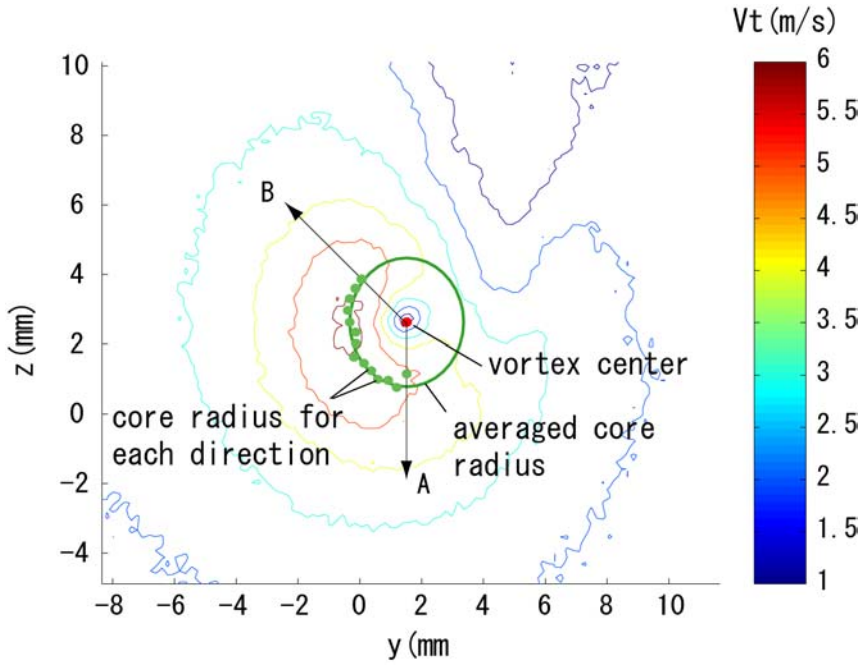

Figure 6-22: Tangential velocity contour and vortex radius definition

("non-injection case" at α=8deg, U_{inf}=8m/s)

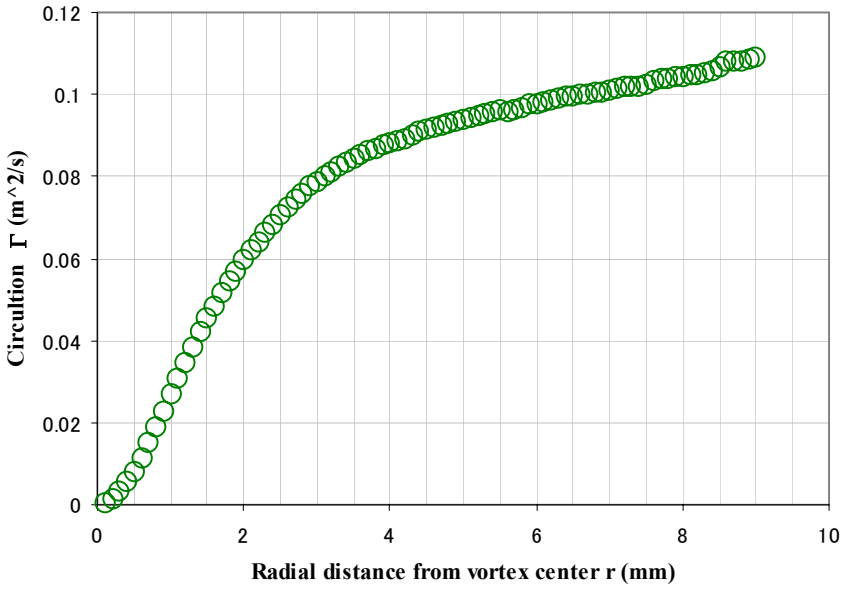

Figure 6-23: Radial distribution of Circulation obtained from vorticity integral

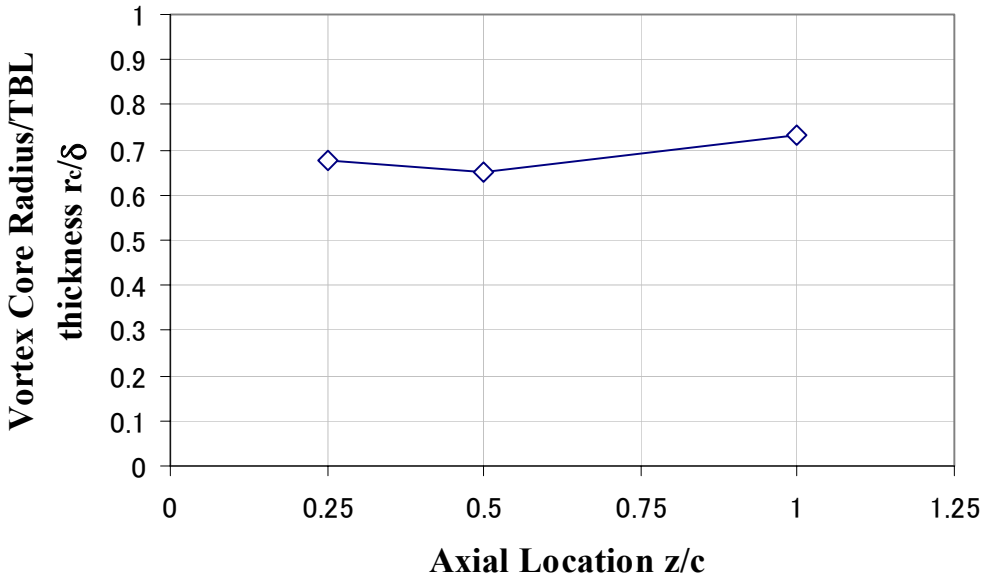

Figure 6-24: Vortex properties at “without injection” condition

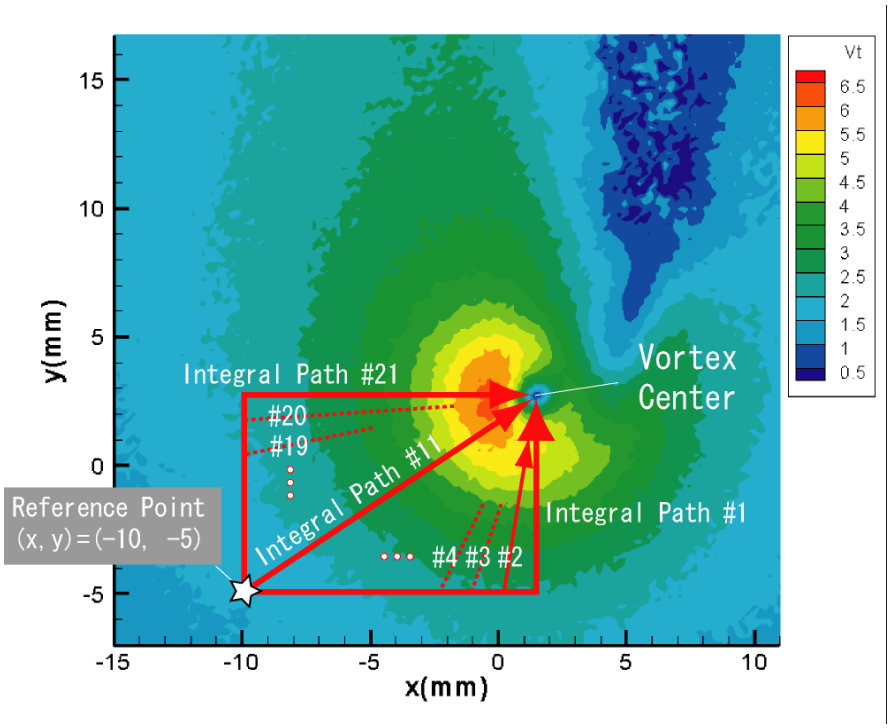

Figure 6-25: Integral path for static pressure estimation

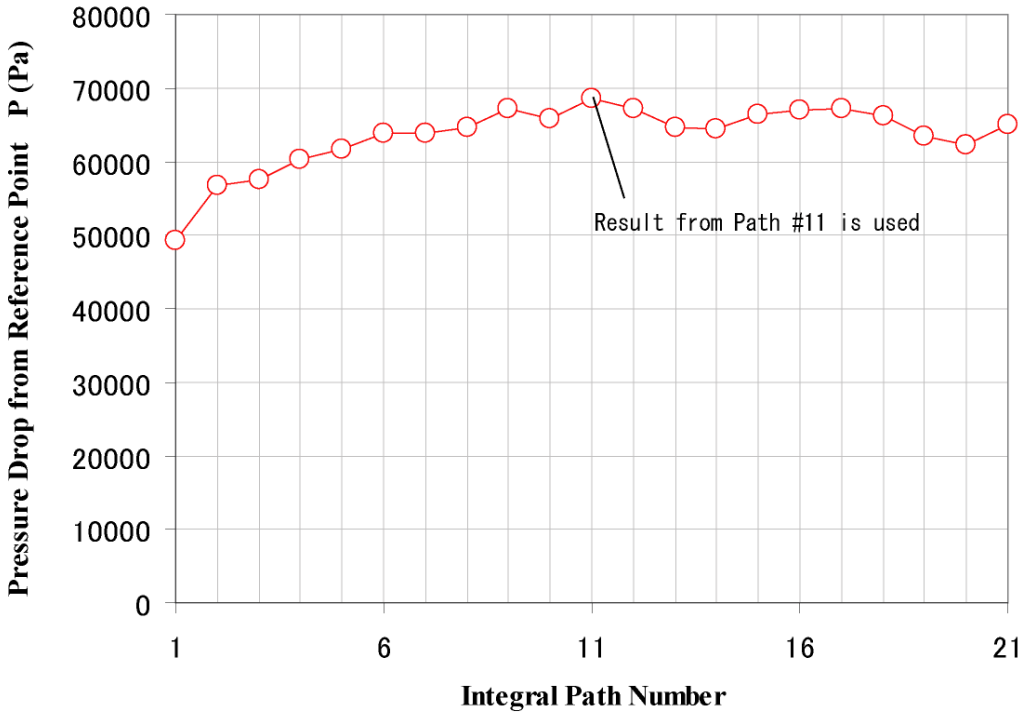

Figure 6-26: Pressure drop estimation dependence on integral path (path number is shown in the previous figure)

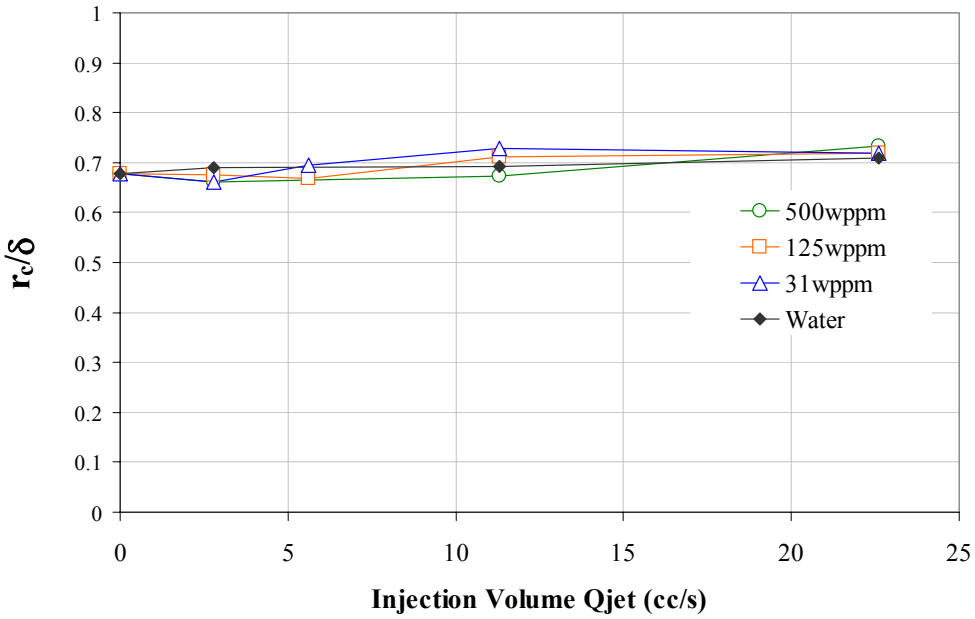

Figure 6-27: Vortex core radius at z/c=25%

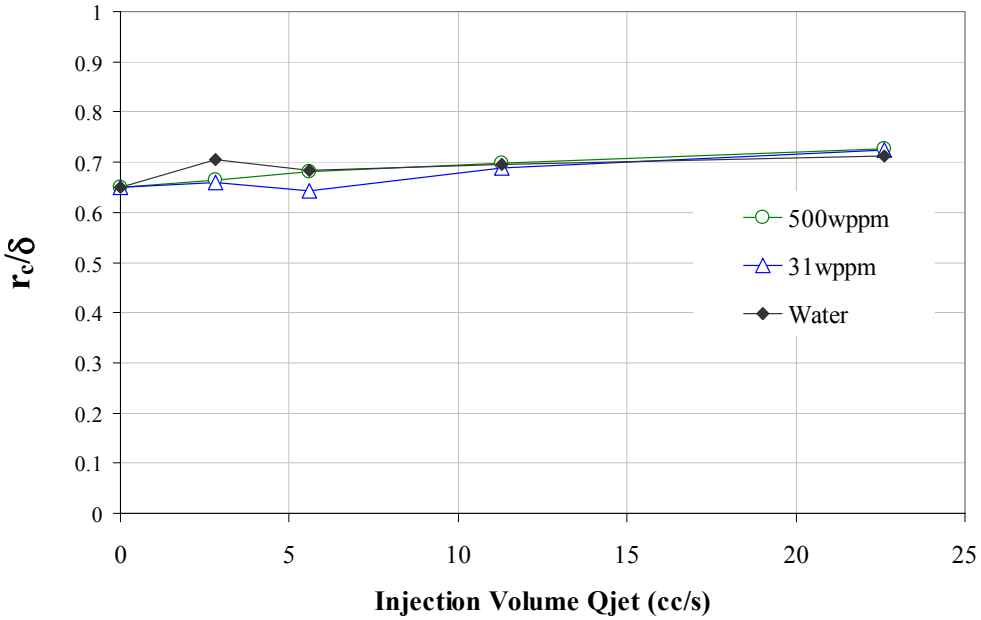

Figure 6-28: Vortex core radius at z/c=50%

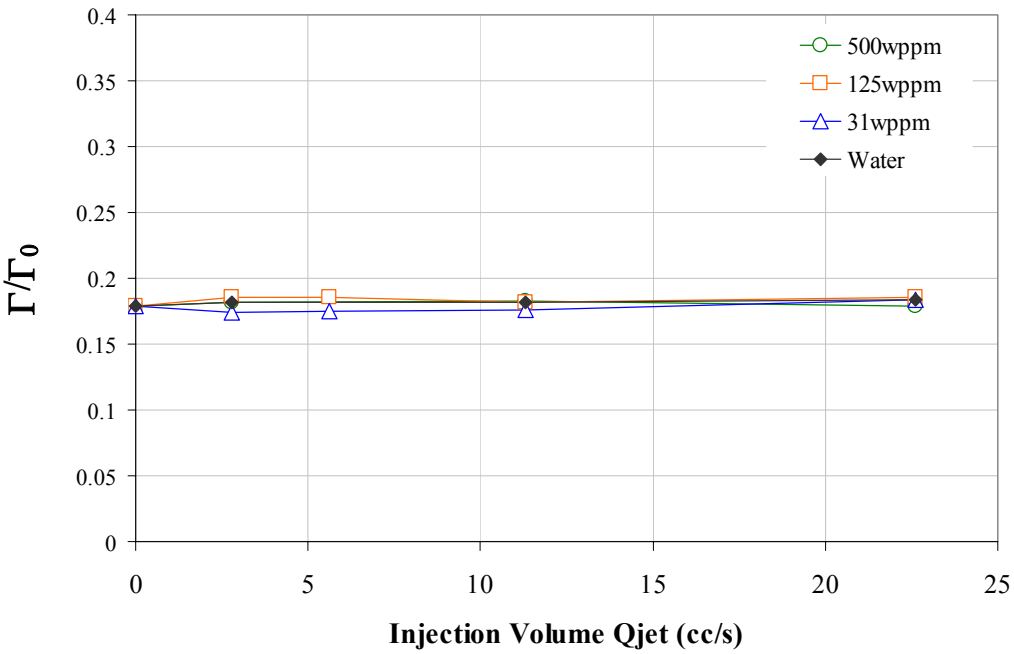

Figure 6-29: Tip vortex circulation at z/c=25%

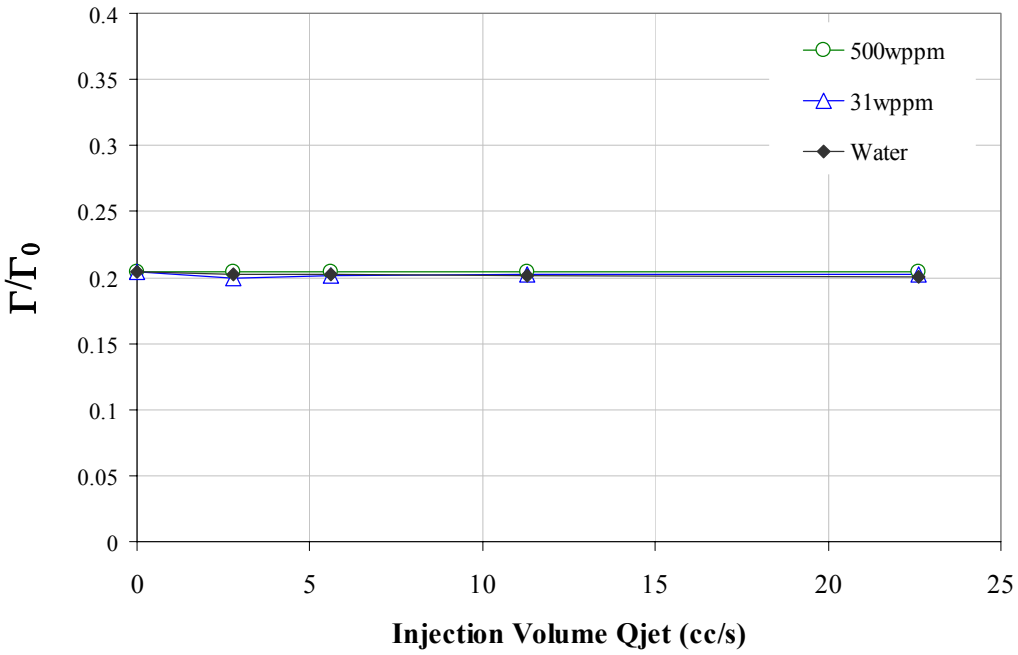

Figure 6-30: Tip vortex circulation at z/c=50%

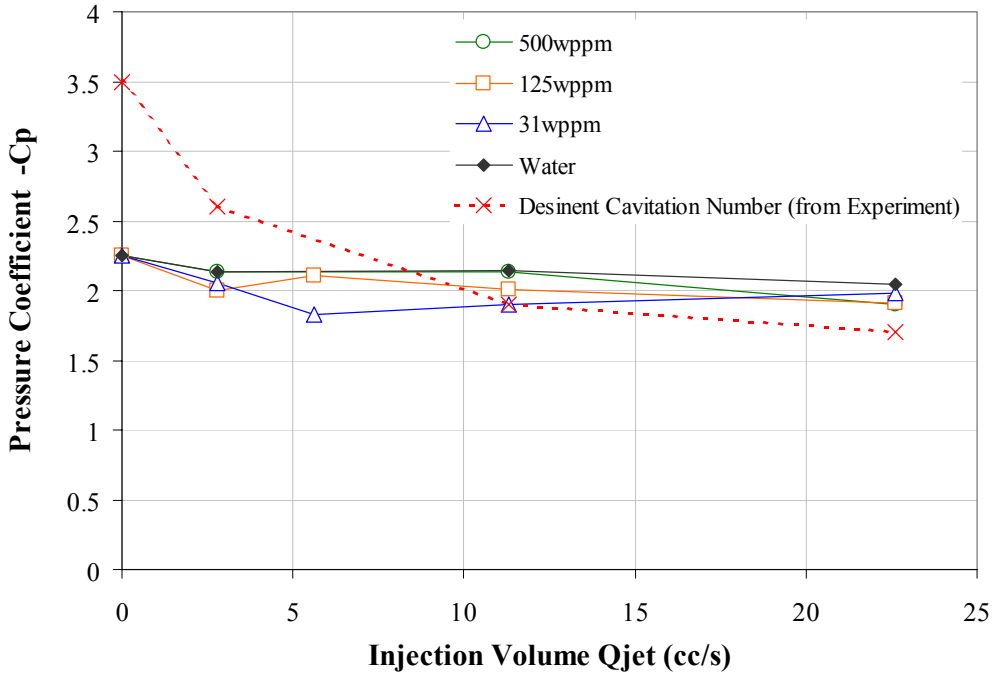

Figure 6-31: Estimated static pressure at vortex core at z/c =25%

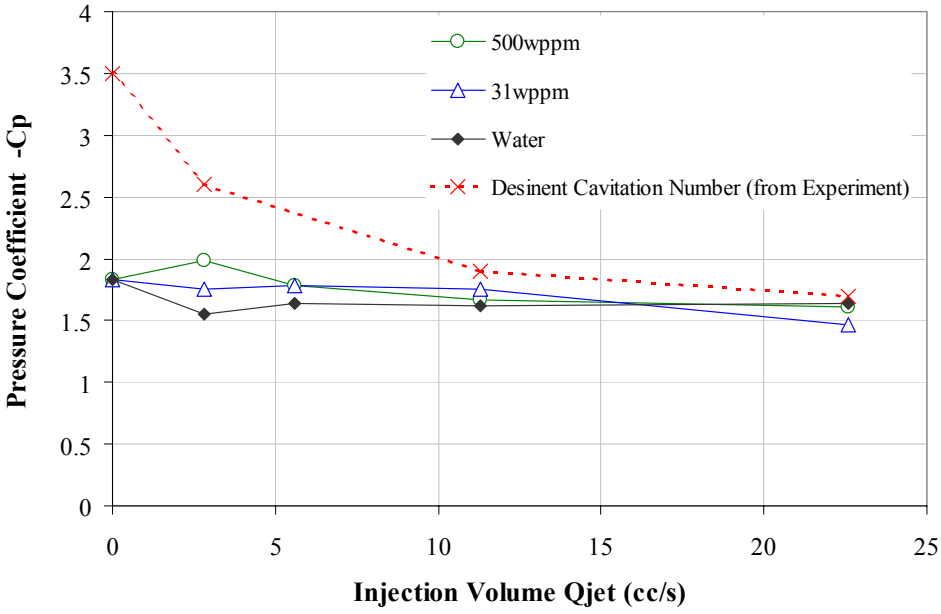

Figure 6-32: Estimated static pressure at vortex core at z/c =50%

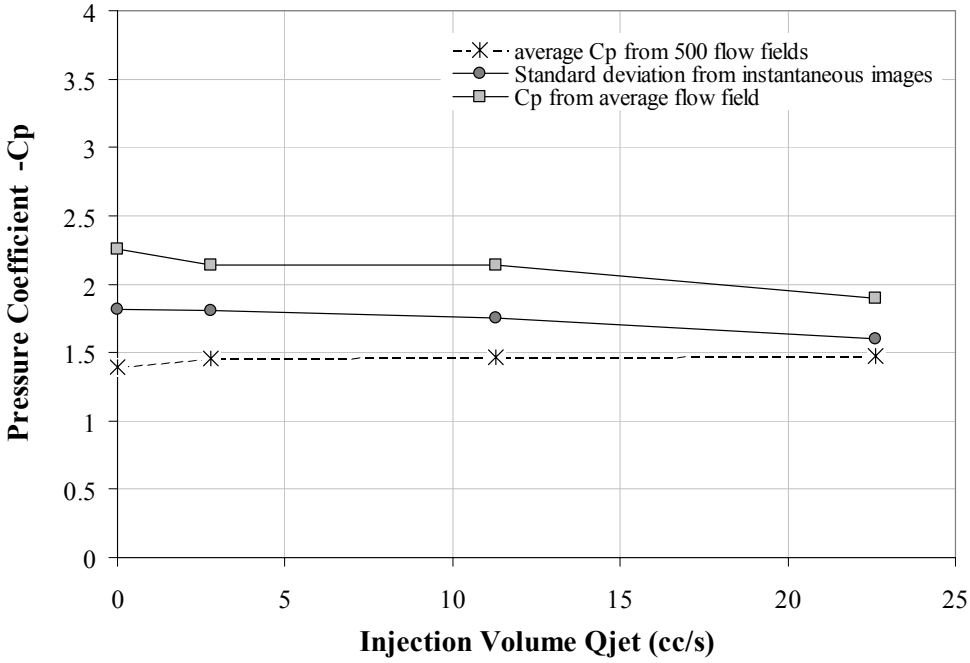

Figure 6-33: Standard deviation of Cp value from 500 instantaneous velocity fields (z/c=25%)

References

Arndt, R.E.A., Arakeri, V.H., Higuchi, H, 1991, *"Some observations of tip-vortex cavitation"*, Journal of Fluid Mechanics, Vol. 229, pp. 269-289

Choi, J., 2006, *"Dynamics and noise emission of vortex cavitation bubbles"*, PhD thesis of the University of Michigan, Ann Arbor

Fruman, D. H., Dugue, C., Pauchet, A., Cerrutti, P., Brianson-Majollet, L., 1992, *"Tip vortex roll-up and cavitation"*, 19th International symposium on naval hydrodynamics, Seoul, Korea

Fruman, D.H., Pichon, T., T., Cerrutti, P., 1995, *"Effect of drag reducing polymer solution ejection on tip vortex cavitation"*, Journal of marine science and technology, Vol. 1, pp13-23

Fruman, D.H., Cerrutti, P., Pichon, T., Dupont, P., ,1995, *"Effect of hydrofoil plan form on tip vortex roll-up and cavitation"*, Journal of fluids engineering, Vol. 117, pp162-169

Liu, X., Katz, J., 2006, *"Instantaneous pressure and material acceleration measurements using a four-exposure PIV system"*, Experiments in Fluids, Vol. 41, pp227-240

Oweis, G.F., D. Fry, Chesnakas C.J., Jessup, S. D., Ceccio, S.L., 2006, *"Development of a Tip-Leakage Flow- part1: The Flow Over a Range of Reynolds Numbers"*, Journal of Fluids Engineering , Vol. 128, pp751-pp755,

Yamaguchi, H., 1999, *"FORTRAN77 program package which can calculate the hydrodynamic characteristics of a two-dimensional foil or cascade in steady incompressible uniform flow with the boundary layer effects taken into account"*, Program available at http://www.fluidlab.naoe.t.u-tokyo.ac.jp/~yama/prog/index-e.html

Chapter Seven

High Speed Video Observation

In the previous chapter, the flow field measurement by SPIV did not show the significant flow field modification by polymer injection. Moreover, it has to be noted that the estimated static pressure from SPIV is much higher than the vapor pressure even in the "without injection" case. This experimental data contradicts the classical model of TVC inception. Thus, it may be necessary to reconstruct a new physics to explain TVC inception/desinence for "non-injection" case, before approaching TVC suppression by polymer injection. Then a further explanation on TVC suppression effect would be established based on the new TVC inception model.

In this chapter, the additional observations were carried out, in order to approach a fundamental physics behind on TVC inception/desinence. Especially, the high-speed video camera observation was carried out to capture the dynamic motion of cavitation bubbles. Additionally, the injected polymer solution was visualized by fluorescence dye, which will provide new information on its behaviors.

7.1 Observation by high-speed video camera

The "non-injection" case and "polymer injection" case of TVC was observed closely by using a high-speed video camera. Kodak Ektapro with 256 by 256pixel resolution was used. Two metal halide lights illuminated the foil tip.

Figure 7-1 shows the sequence of images taken at σ=3.5, which corresponds to a very discrete TVC appearance in Figure 5-1 (in fact, bubbles are hardly captured in a still picture due to the very low event rate). It should be noted that the bubble appears at not exactly on the blade tip, but the downstream (z/c~10-20%). This bubble inception location matches Arndt et al (1991)'s observation. In this condition, 10 sets of TVC inception events were captured in the movie. Activated bubbles appeared around z/c=10-20% in 9 of 10 cases and bubbles incept just on the hydrofoil tip in the rest of cases. After inception, the bubble grows both upstream and downstream. In terms of a bubble's downstream growing, Choi (2006) observed the similar bubble appearance in a single vortex cavitation. On the other hand the upstream growing is unique for this study. Although it is hardly recognized in a sequence of still pictures, a front tip of the bubble is wobbling around near the tip region (see Figure 7-2). In a classical model of three-dimensional hydrofoil, a single line vortex is shed from a hydrofoil tip and this flow structure is thought to be steady (Franc and Michel (2004)). But the wobbling of the bubble indicates the existence of unsteadiness of flow structure near the tip. In addition to that, the upstream growing infers that secondary low-pressure region exists upstream from bubble inception point (z/c~10-20%). The static pressure at this region would be higher than the TVC inception region located at downstream, because TVC incepts more frequently at downstream than this tip region.

Figure 7-3 shows the images taken with polymer injection. The injected polymer solution was fluoresced by Rhodamine 6G. The main difference observed was that TVC incepts from the surface of the blade tip when polymer was injected, unlike the "non-injection case". Exactly saying, the inception point during polymer injection was just on the injection hole. This cavitation may be induced by a shear flow or secondary vortex flow on the edge of the injection hole. In addition, the bubble is activated "NOT ON" the injected polymer flow path, which was assumed to be the core of the primary vortex. The bubble was subsequently trapped into the primary vortex core. Finally, the activated bubble was dissipated at the downstream. (see Figure 7-4) Therefore, the laser bubble detector used in the cavitation desinence test cannot detect this local cavitation.

7.2 Flow visualization by Fluorescence

To capture the behavior of injected polymer, intensive flow visualization was carried out with a fluorescence dye. Rhodamine 6G was diluted in an aqueous polymer solution and this dye was fluoresced by a stroboscopic light. Figure 7-5 shows the pictures taken in both polymer injection case and water injection case. The right picture was taken with 2500 wppm polymer solution injection (Q_{jet}=11.3cc/s). The concentration of Rhodamine was 500 wppm. The left picture was taken in the water injection case and the injection flux rate was the same as the polymer injection case.

In the water injection case (right side of the figure), the injected water was trapped into the vortex core and shed downstream. The injected polymer was gradually dissipated from a vortex core by turbulence. On the other hand, the dyed polymer picture (left side of the figure) showed completely different appearance, especially in terms of the absence of turbulent dissipation. The injected polymer path was not single line but showed multiple paths. In this condition (Q_{jet}=11.3cc/s), the jet velocity from the injection hole was lower than the uniform flow velocity (V_{jet}/U_{inf}=0.71). Simply saying, the environmental fluid pulls out the aqueous polymer solution from the injection hole. The multiple paths indicate that the polymer is pulled out from an injection hole unsteadily and resulted in a filament.

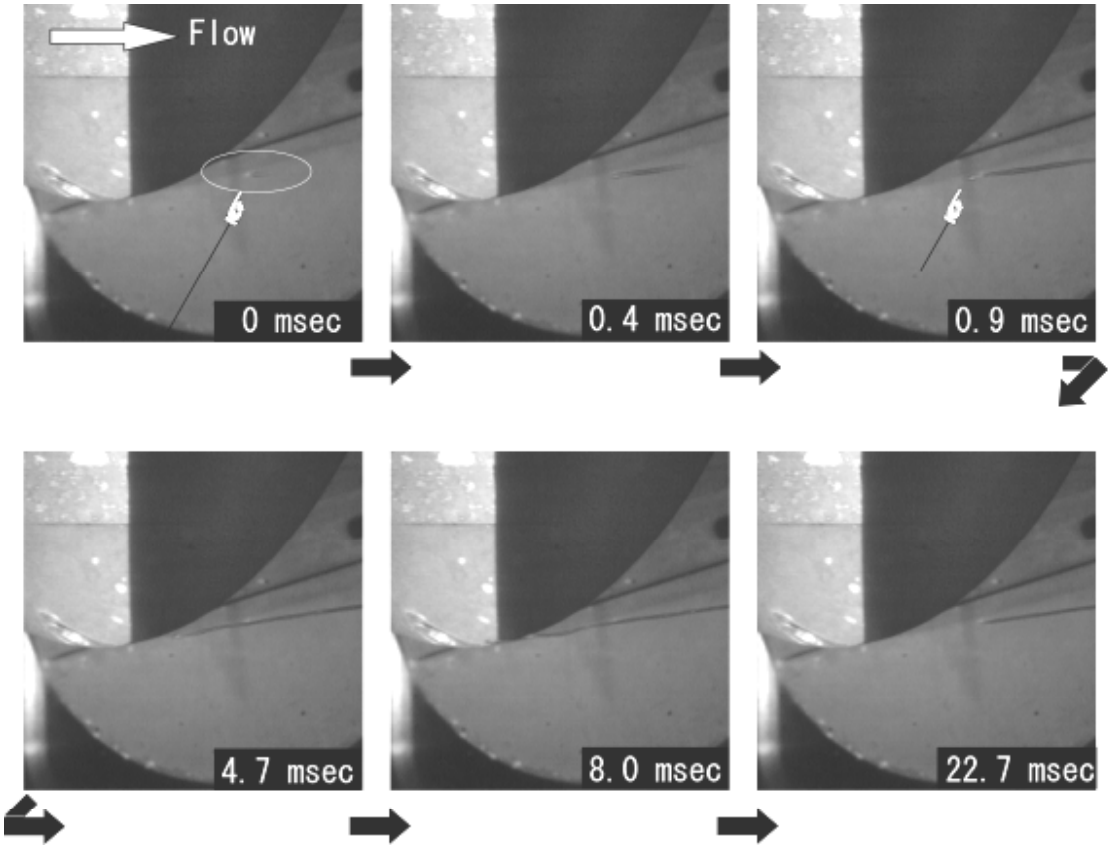

Figure 7-1: High-speed video images without polymer injection
(U_{inf}=8m/s, α=8deg, σ_{∞}=3.5, DO=37%)

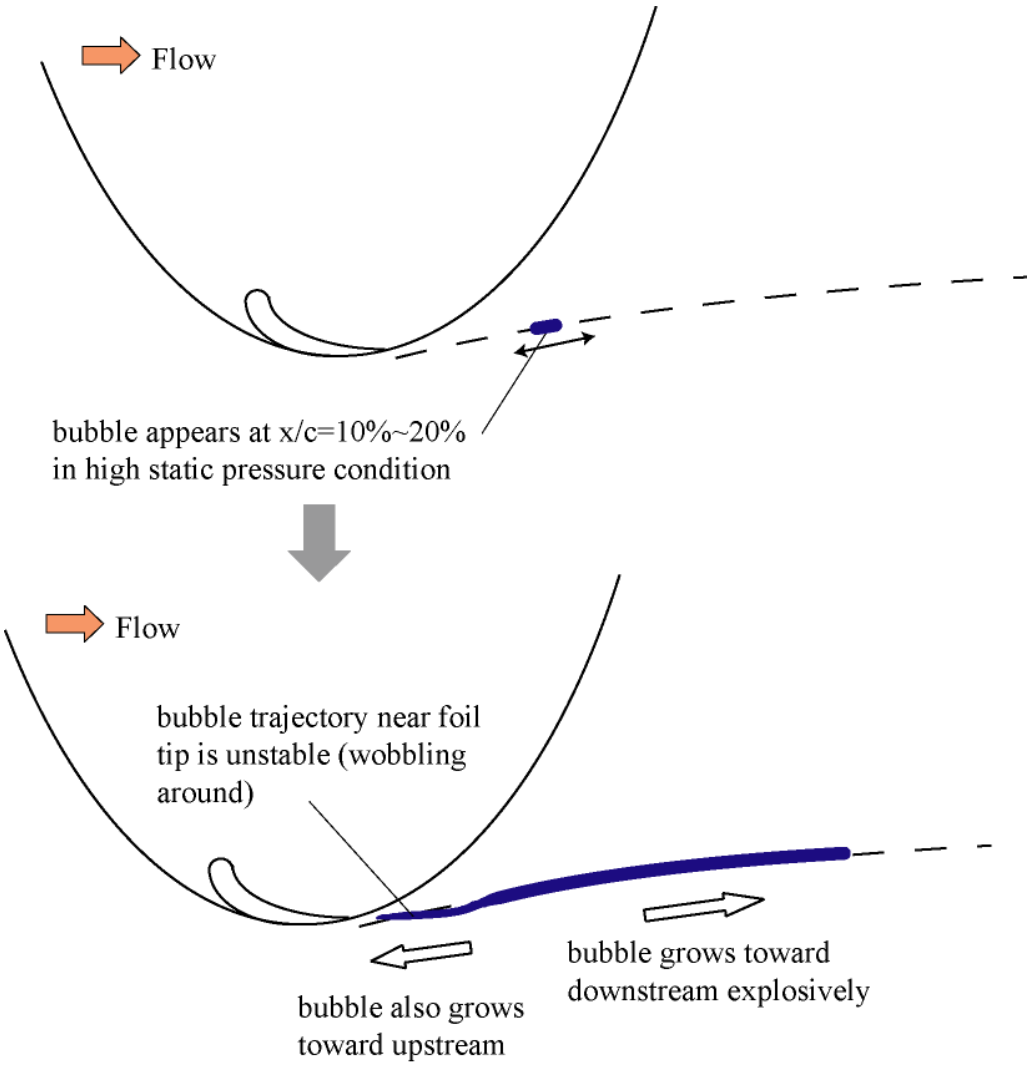

Figure 7-2: Flow field structure in "without injection" condition

(Corresponding to high speed camera images in Figure 7-1)

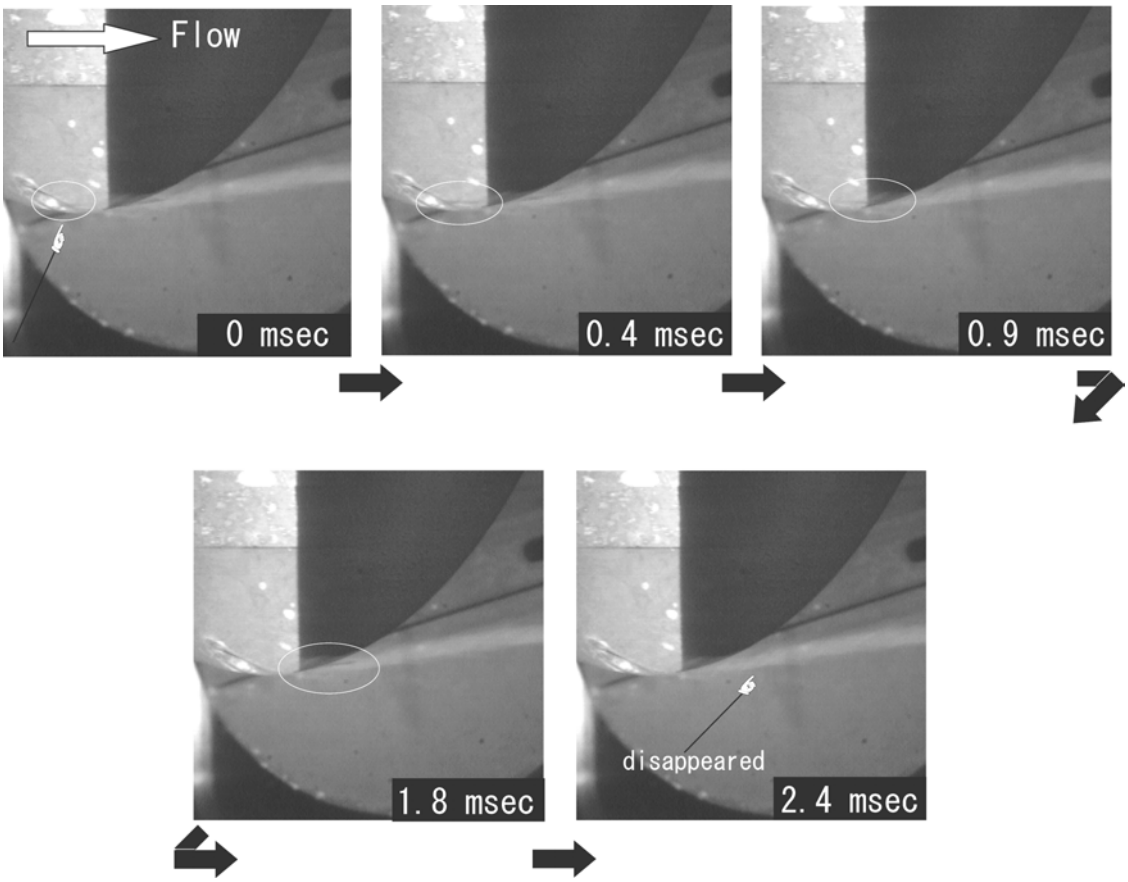

Figure 7-3: High-speed video images with polymer injection

(U_{inf}=8m/s, α=8deg, σ_{∞}=2.5, with Injection C=125wppm Q_{jet}=22.6cc/s, DO=35%
Fluoresced byRhodamine6G 100wppm)

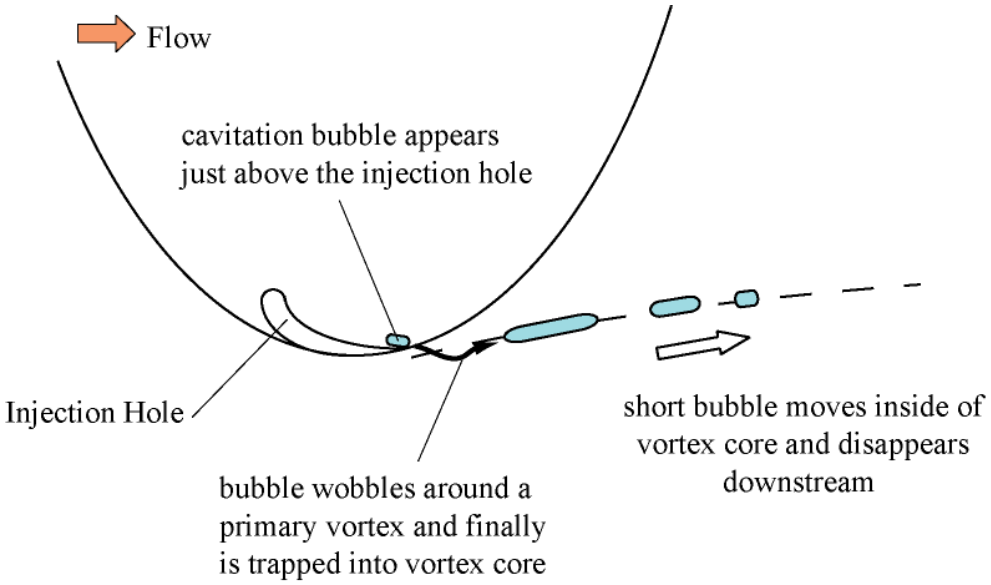

Figure 7-4: Flow field structure in “with polymer injection” condition

(Corresponding to high speed camera images in Figure 7-3)

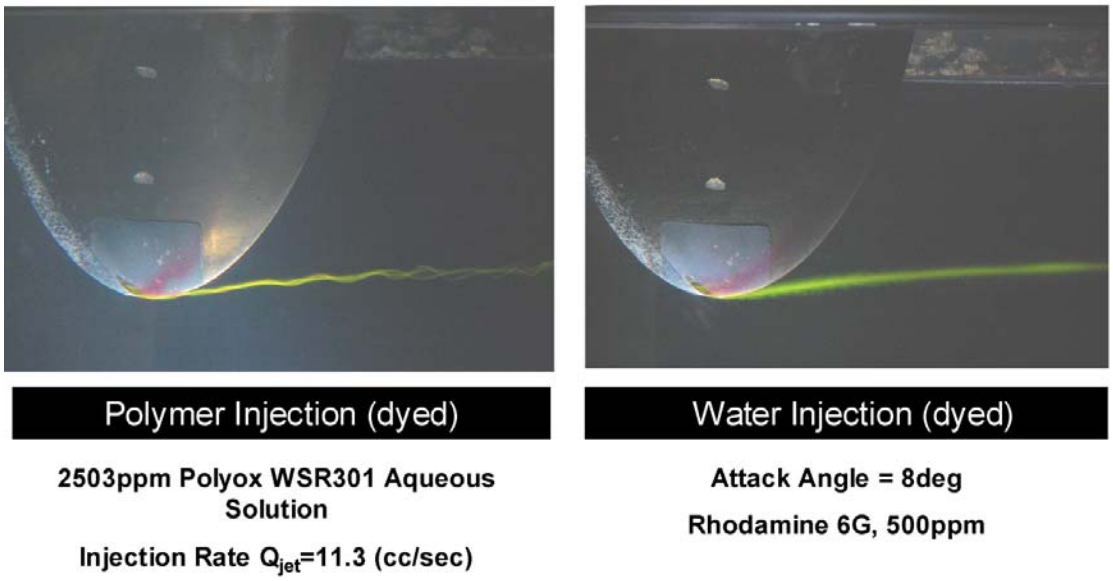

Figure 7-5: pictures taken with fluorescence dye

References

Arndt, R.E.A., Arakeri, V.H., Higuchi, H, 1991, *"Some observations of tip-vortex cavitation"*, Journal of Fluid Mechanics, Vol. 229, pp. 269-289

Choi, J., 2006, *"Dynamics and noise emission of vortex cavitation bubbles"*, PhD thesis of the University of Michigan, Ann Arbor

Franc, J. P., Michel, J.M., 2004, *"Fundamentals of Cavitation"*, Kluwer Academic Publishers

Chapter Eight

Discussion

8.1 TVC inception mechanism without polymer injection

8.1.1 Result from this study

In Chapter Five, the quantitative results from the TVC suppression effect by polymer/water injection were evaluated and a new method for estimating cavitation desinence using a laser bubble detector was introduced. The nuclei effect was also examined and it was inferred that the background nuclei still controls TVC event rate regardless of polymer injection. From those facts, the flow field modification due to mass injection is thought to be the primary source of the TVC suppression.

However, the flow field measurement by SPIV does not show average changes to the flow field by water or polymer injection. Moreover, it has to be noted that the estimated average static pressure from SPIV is much higher than the vapor pressure even in the "without injection" case.

This work originally aimed to approach the mechanism on TVC suppression by polymer injection. However, the findings in the previous chapters do not reveal significant modification of the average properties of the primary tip vortex with mass injection. Thus it can be inferred that other flow physics is involved and it may be necessary to reconstruct a new hypothesis to explain TVC inception/desinence for the baseline (non-injection) case.

The detailed observation by high-speed video in chapter seven reveals the presence of flow unsteadiness at the tip region and the injected water and polymer is thought to modify and possibly reduce this flow unsteadiness.

In the next part, the experimental data from past studies will be reviewed again with a special attention to the consistency between the average static pressure in the vortex core and the observed cavitation inception value.

8.1.2 Extensive review on past studies

For the first example, Fruman's two studies are reviewed. In Fruman (1995(a))'s study, the flow field around a tip vortex was measured by LDV. For the simple elliptic planform foil (with NACA16020 section), the cavitation desinence point was found to be σ_d=0.83 and the pressure coefficient at vortex center was estimated to be Cp=-0.48. This means that TVC incepts at higher cavitation number than the estimated by a flow field measurement. In the paper, they explicitly declare the definition of cavitation desinence point as follows:

> *"The incidence angle was then increased slightly to form a well developed tip vortex cavity, in the shape of continuous filament, and desinence conditions were obtained by reducing the angle"*

This expression means that the TVC desinence was defined at the point, in which TVC ceases to form a continuous bubble tube. This definition doesn't corresponds to the definition of study's definition, in which very low event rate (T1/T2=0.01 in chapter Five) is defined to be "inception/desinence point". Therefore it is still possible that a very discrete bubble appeared at higher pressure than σ_d=0.83.

Fruman (1995b)'s second work is associated with TVC suppression by polymer injection. In the study, the cavitation desinence point in "non-injection" case (σ_d=1.95) is also higher than the expected cavitation inception point from flow field measurement. This fact can be explicitly recognized in the figure of their paper (the same figure is referred in Figure 2-2). They simply assumed that the existence of a lowest static

pressure point from the cavitation desinence number and this assumption is just based on a classical steady flow model of TVC inception.

Arndt et al. (1991)'s study seems to show an opposite result, in which TVC inception occurs at lower static pressure (σ_d= 1.0) than the estimated core pressure (Cp=-2.3). But with a careful reading on their expression, the definition of TVC is expressed as follows,

"inception was characterized by the sudden appearance of a defined, fully cavitating vortex (for strong water)"

This indicates the possibility of the existence of discrete bubbles in higher static pressure than the their desinence definition. In our study, the cavitation desinence point is σ_d=3.5, but a continuous bubble tube starts to appear at σ=2.9 (see Figure 5-1). Therefore the different definitions of TVC inception can introduce a difference of σ (in our case, $\Delta\sigma$= 0.6). In Arndt et al's case, there is no description on the cavitation number, when a discrete bubble starts to appear. However it may probably happened that a discrete cavitation event started to occur at a higher cavitation number than σ_d =1.0.

Steinberg et al (1991)'s study shows a good agreement with cavitation inception number and flow field measurement. Though, an explicit definition of the cavitation inception point was not given, the planform of their study was trapezoidal, which is different from our study. This geometrical difference probably makes the flow structure near the foil tip.

In summary, the cavitation inception/desinence measurements reported in past studies were also not consistent to the average pressure coefficient estimated from corresponding flow field measurement. This also points to the existence of flow unsteadiness in the tip region as a cause of TVC inception.

8.2 Mechanism of TVC inception and its suppression

As discussed in chapter 8.1, the unsteadiness of the flow near the hydrofoil tip may contribute TVC inception mechanism in "non-injection" condition. This unsteadiness will be related to the following several possible factors. One is the vortex-vortex interaction, which was reviewed in chapter 2.6.2 and second possible factor is the turbulence induced by a shear flow between a uniform velocity and vortex core velocity.

For a vortex-vortex interaction, the vorticity fragmentation is thought to increase the flow unsteadiness and result in a low static pressure during the merging process. Near the elliptic foil tip, the tip vortex from the lifting line can be a primary vortex. Then the separation bubble at the leading edge, or other local vortex can be a secondary vortex.

For the second factor, Fruman et al. (1992)'s LDV measurement shows the existence of axial jet on the vortex core just downstream from the tip. The shear between uniform flow and this jet in the vortex core can provide unsteadiness. In this study, we can recognize the unsymmetrical axial flow around a core in Figure 6-10. This structure also can cause a turbulent flow around a vortex core and this might be analogous to jet cavitation or shear cavitation.

Though this study does not have enough data to confirm the origin of the unsteadiness, it should be noted that the coherent fragmentation of vorticity may introduce a low pressure and this can govern TVC inception in the first two scenarios.

In addition to that, the fluctuation of the vortex property can be a source of the lower static pressure, which can account for the higher cavitation desinence point.

8.3 Hypothesis on the mechanism of TVC suppression by polymer

As discussed in the previous part, the unsteadiness near the foil may be responsible for the TVC inception mechanism. Therefore, the suppression mechanism can be inferred to be strongly related to the unsteadiness of the flow field.

Based on the possible mechanism for TVC inception, especially for the origin of unsteady flow field near the foil tip, we are able to construct a hypothesis on TVC suppression. Even though the unsteadiness can potentially be introduced by several possible factors, each unsteadiness is related to the fragmentation of vorticity from shear layer flow or vortex-vortex interaction. The elasticity of the polymer solution may suppress this fragmentation of vorticity and finally resulted in a higher static pressure.

In each story, the viscoelastic solution suppresses dynamic flow unsteadiness near the foil tip and result in TVC suppression.

The mechanism suggested here can be also supported by TVC inception location observed in this study. As we see in chapter 7.1, most bubbles are activated nearby the foil tip (z/c~10-20%). But still pictures taken in "polymer injection case" show that the inception point moves downstream. (In Figure 5-2, bubbles does not appear around z/c~10%-20%.) In other words, the bubbles start to appear at further downstream and it may correspond to the location, in which the vorticity from a hydrofoil trailing edge is rolled-up.

8.4 Scalability of suppression effect

Although the suggested mechanism of TVC suppression includes some unknown parts (especially the origin of unsteadiness), we can introduce a way to scale the "possible maximum" suppression effect up to the ship scale propeller. Basically, the suppression effect due to polymer injection does mainly work on the unsteady component of flow structure. Therefore, the suppression effect will be saturated at the cavitation inception/desinence point, which is estimated from a classical steady tip vortex roll-up model. However, it should be noted that the scaling of steady flow structure model itself contains some difficulty. Fruman et al. (1992)'s study revealed that the jet velocity inside of the vortex core shows completely different characteristics in a large scale. The axial jet velocity in the vortex core at large hydrofoil (chord length is 475mm) is much higher than the smaller foil (chord length is 40mm). But it is still possible to estimate a maximum suppressed point from a time averaging velocity measurement experimentally. At the end of this chapter, this study strongly recommends the large-scale experiment on TVC suppression effect by polymer injection and complete flow measurement around a vortex core.

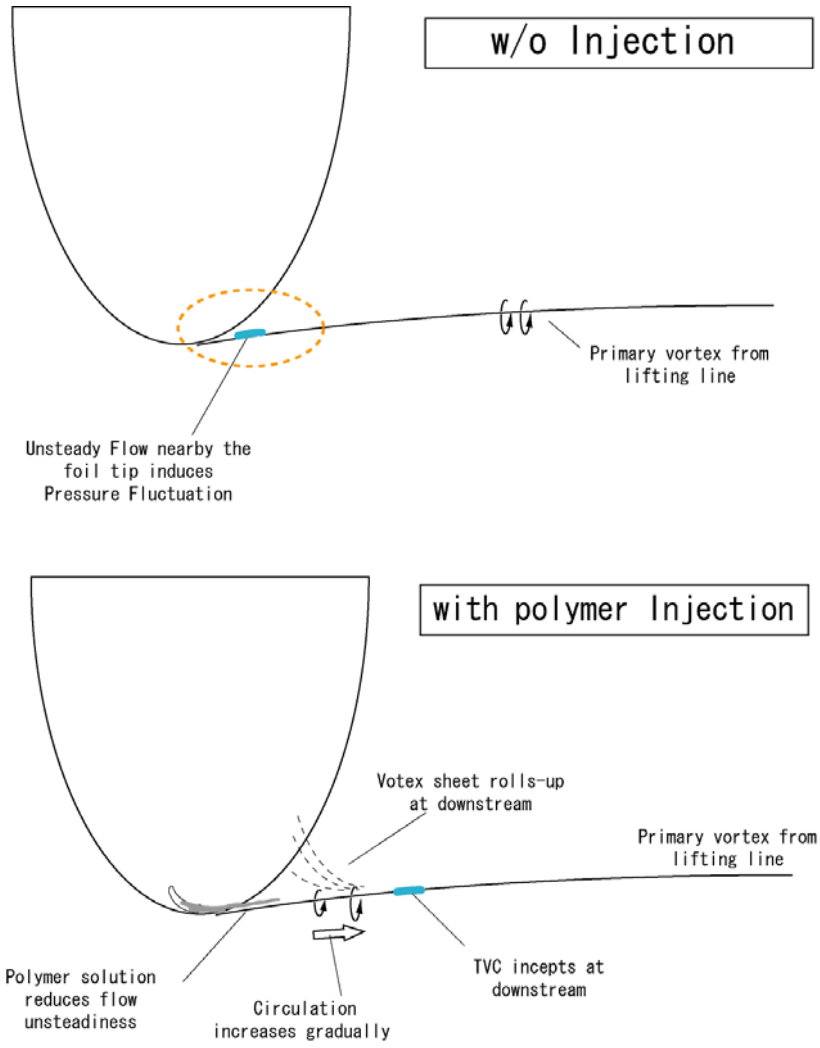

Figure 8-1: TVC suppression and inception location

References

Arndt, R.E.A., Arakeri, V.H., Higuchi, H, 1991, *"Some observations of tip-vortex cavitation"*, Journal of Fluid Mechanics, Vol. 229, pp. 269-289

Fruman, D.H., Dugue, C., Pauchet, A., Cerrutti, P., Pichon, T., Brianson-Marjollet, L., ,1992, *"Tip vortex roll-up and cavitation"*, International symposium on Naval Hydrodynamics, Seoul, Korea,

Fruman, D.H., Cerrutti, P., Pichon, T., Dupont, P., ,1995 (a), *"Effect of hydrofoil planform on tip vortex roll-up and cavitation"*, Journal of fluids engineering, Vol. 117, pp162-169

Fruman, D.H., Pichon, T., T., Cerrutti, P., 1995 (b), *"Effect of drag reducing polymer solution ejection on tip vortex cavitation"*, Journal of marine science and technology, Vol. 1, pp13-23

Stinebring, D., Farrell, K., Billet, M., 1991, *"The structure of a three dimensional tip vortex at high Reynolds numbers",* Journal of Fluid Engineering, Vol. 113,

Chapter Nine

Conclusion

This study aims to present the underlying the physics on active TVC (Tip Vortex Cavitation) control by polymer/water injection. From the literature review on previous research on the general physics of TVC and its suppression, the following strategies were established.

First of all, the degree of TVC suppression by water and polymer injection has to be determined by a quantitative method. Secondly, the experiment should be done in an well-controlled environment, especially, in terms of water quality. Then it was expected to reconstruct a base mechanism on TVC inception itself, with up-to-date measurement technologies.

Based on these strategies, a cavitation susceptibility meter was used for water quality determination. The measurement error and bias, for a specific set-up in this study, were evaluated and discussed in Chapter Three. Then CSM was confirmed to satisfy the purpose of this study.

In Chapter Five, a new method of cavitation detection by using a laser scattering was introduced. The system captured the degree of TVC suppression due to polymer injection and the following knowledge was obtained. The suppression effect was saturated at high concentration and high injection rate. Several ways to scale the suppression effect was tried in this study (e.g. the volumetric rate between injected liquids and vortex core flux), however it was difficult to find a simple scaling law. This study confirmed that water injection can suppress TVC with high injection rate, but not

effective as polymer injection. Water nuclei dependence was surveyed with CSM measurement and it was found that the background nuclei density governs event rate. This fact supports the idea, in which TVC suppression is caused by a change of flow structure, as the past study showed.

Following that, flow field measurement was done by using Stereo Particle Image Velocimetry (SPIV). The resulted flow field was used to estimate the static pressure in a vortex core by integrating the conservation equation of momentum. The estimated average static pressure at the baseline conditions was not low enough for cavitation desinence. On the contrary, the estimated average static pressure with mass injection agreed with a cavitation desinence test data. An attempt was made to use the SPIV data to estimate the unsteady pressure fields, but the data was not certain enough to successfully do this with confidence.

In Chapter Seven, a close observation on TVC inception was carried out with a high-speed video imaging and fluorescence dye. The additional observations showed that the unsteadiness near the hydrofoil tip region can lead to a low pressure. This unsteadiness can be introduced by several factors (e.g. vortex-vortex interaction or shear between a vortex core and uniform flow), but the fragmentation of the vorticity makes the large pressure fluctuation in each story (i.e. vortex stretching or shear flow oriented unsteadiness).

At the end, this study is suggesting a new hypothesis on TVC inception mechanism and its suppression by polymer injection. The elasticity of the polymer solution may suppress the formation of the vorticity filament and result in prohibiting a large pressure fluctuation.

However, additional works are still required. To approach the original purpose, that is to say the application of active TVC suppression to a real ship scale propeller, further experimental study with a large-scale model is strongly desired, since the vortex interaction and other flow structure can be changed at different Reynolds number scale.